

# Dissertation

zur

Erlangung der Doktorwürde (Dr. rer. nat.)

der

Gesamtfakultät für Mathematik, Ingenieur- und

Naturwissenschaften

der

Ruprecht-Karls-Universität Heidelberg

Thema

**N-Heteropolycycles on graphene: Supramolecular  
organization and charge transfer**

Vorgelegt von

**M.Sc. Maximilian Krings**

geboren in Mannheim

Gutachter

Prof. Dr. Claudia Backes

Prof. Dr. Felix Deschler

Tag der mündlichen Prüfung: 13. Juni 2022



# Dissertation

to obtain the degree of

Doctor of the Natural Sciences (Dr. rer. nat.)

submitted to the

Combined Faculty of Mathematics, Engineering and Natural

Sciences

at the

Ruprecht-Karls-Universität Heidelberg

Topic

**N-Heteropolycycles on graphene: Supramolecular  
organization and charge transfer**

Presented by

**M.Sc. Maximilian Krings**

born in Mannheim

Reviewer

Prof. Dr. Claudia Backes

Prof. Dr. Felix Deschler

Oral examination: June 13<sup>th</sup> 2022

*Für Vanessa*

*If I am guilty of anything it is the simple pursuit of knowledge.*

Magnus the Red at the Council of Nikaia  
*A Thousand Sons* (Novel) by Graham McNeil



# Abstract

This work aims at a more detailed understanding of non-covalent doping of graphene and Molybdenumdisulfide using aromatic *N*-heteropolycycles. Therefore a wide variety of molecules is first deposited via wet-deposition onto graphene, to then investigate the induced changes in Fermi energy of graphene with both Raman spectroscopy and Kelvin-Probe-Force Microscopy. The induced shifts in graphene are then correlated with both the molecular geometry and substituents, as well as their electronic properties to derive a structure-effect relation that can be used to guide the fine tuning of graphene's electronic and surface properties.

All methods in this work, from deposition to measurements are done under ambient conditions to mimic the conditions of real live applications and to avoid perfect lab conditions like ultra-high vacuum that are not viable for end-of-the line device production and use. This idea is also applied to the graphene that is used itself, as commercially available graphene was used for all experiments.

With this framework in mind the first steps of this project were to establish a suitable sample preparation routine to achieve a reproducible and comparable graphene substrate for the subsequent measurements. Due to CVD-grown and wet-transferred graphene being contaminated with polymer residues and water this was a crucial step for reliable results in the end. Comparing a wide range of different molecules, it was also necessary and important to formulate a deposition procedure that can be applied to all molecules, although probably not optimized for the specific molecule it was optimized for the overall comparison of all molecules on even ground.

The first results of the deposition of both TIPS-Tetraazapentacenes and Tetraazaperopyrenes show a strong dependence of the graphene doping on the acceptor strength (=LUMO energy) of the molecules and less on the overall molecular structure (i.e. substituents and substitutional patterns).

With those established protocols and findings the relations of charge transfer interaction between molecules and graphene were further refined with additional acceptor molecules (Benzonaphthyridines) and also demonstrated for the opposite interaction with donor-type Heterotriangulenes showing trends in-line with the theory.

In case of the Benzonaphthyridines and Heterotriangulenes the graphene modification was carried a step further by utilizing the molecule specific properties of possible protonation with common acids and oxidation via UV irradiation to introduce a second stage of charge transfer after initial deposition. This demonstrated that it is possible to further modify already assembled molecules on graphene (and as a consequence the Fermi level of graphene as well) without major damage to graphene itself, although in our cases the overall changes following the second modification were small, but could easily be increased with specific molecules engineered for those kinds of applications.

To delve even further into the non-covalent nanomaterial doping all, the gained insights and experiences from graphene were then taken to Molybdenumdisulfide ( $\text{MoS}_2$ ) to see whether the rules of structure-effect-relations derived from graphene can be applied to a different class of nanomaterial and to see specific differences and whether they follow the theoretical expectations. With the self-assembly of molecules being guided by mainly  $\pi$ - $\pi$  interactions on graphene,  $\text{MoS}_2$  shows that the acceptor strength is one of the driving factors not only for the electronic modification but also for the deposition itself.

## Kurzzusammenfassung in deutscher Sprache

Ziel dieser Arbeit war es, ein tieferes Verständnis nicht-kovalenter Dotierung von Graphen und Molybdändisulfid mit *N*-Heteropolyzyklen zu erreichen. Hierzu wurden verschiedene Moleküle über ein lösungsbasiertes Verfahren auf Graphene abgeschieden. Die daraufhin induzierten Änderungen der Fermi Energie wurden dann sowohl über Raman Spektroskopie als auch Kelvinsondenkraftmikroskopie untersucht. Die beobachteten Auswirkungen auf die Fermi Energie wurden dann mit verschiedenen Parametern der Moleküle, wie Geometrie, Substituenten und elektronische Eigenschaften korreliert um eine Struktur-Effekt Relation abzuleiten, mit deren Hilfe eine Feinabstimmung der elektronischen und oberflächen-bezogenen Eigenschaften von Graphene vorgenommen werden kann.

Alle in dieser Arbeit verwendeten Methoden, von der Abscheidung bis zu den Messungen, wurden unter normalen Umgebungsbedingungen durchgeführt, um reale Anwendungsbedingungen zu immitieren und perfekte Laborbedingungen, wie z.B. Ultrahoch-Vakuum zu vermeiden, da diese keine realisierbaren Methoden für Produktion und Verwendung im Industriemaßstab darstellen. Dieser Gedanke wurde auch direkt auf das verwendete Graphen direkt übertragen, indem bereits kommerziell erhältliches Graphen für alle Experimente verwendet wurde.

Mit diesen Rahmenbedingungen abgesteckt waren die ersten Schritte dieses Projektes zunächst die Erstellung einer passenden Probenpräparation um reproduzierbare und untereinander vergleichbare Graphen Substrate für die folgenden Messungen zu erhalten. Da CVD-gewachsenes Graphen (CVD engl.: Chemical Vapor Deposition, deutsch: Chemische Gasphasenabscheidung), welches anschließend nasschemisch transferiert wurde sowohl mit Wasser als auch Transfer-Polymer kontaminiert ist, war dies ein entscheidender Schritt für letztendlich verlässliche Ergebnisse. Da eine breite Auswahl verschiedener Moleküle abgeschieden wurden, war es außerdem notwendig ein Abscheidungsprotokoll zu erarbeiten welches auf alle Moleküle gleichermaßen angewendet werden konnte. Auch wenn dieses Abscheidungsprotokoll daher nicht für jede spezifische Molekül-Klasse optimiert wurde, war aber ein Vergleich aller Moleküle unter gleichen Bedingungen gegeben.

Die ersten Ergebnisse der Abscheidung von sowohl TIPS-Tetraazapentacenen als auch Tetraazaperopyrenen zeigen eine deutliche Abhängigkeit der beobachteten Dotierung Graphens von der Akzeptorstärke der Moleküle und weniger eine Abhängigkeit von der Molekülstruktur (Substituenten und Substitutionsmuster).

Mit diesen Ergebnissen und den bis hier aufgebauten Methoden wurde der Ladungstransfer zwischen Molekülen und Graphen mit weiteren Akzeptoren (Benzonaphthyridine) demonstriert. Zusätzlich wurden auch Donoren (Heterotriangulene) untersucht. Beide zusätzlichen Molekülgruppen zeigen Trends die bezüglich der zugrunde liegenden Theorie zu erwarten sind.

Im Falle der Benzonaphthyridine und Heterotriangulene wurde die Graphenmodifikation noch einen Schritt weiter geführt, indem molekülspezifische Eigenschaften nach Abscheidung ausgenutzt wurden um nachträglich den Ladungstransfer zu beeinflussen. Hierbei handelt es sich einerseits um eine mögliche Protonierung mit laborüblichen Säuren und die Oxidation durch ultraviolette Strahlung. Es konnte dabei demonstriert werden, dass es möglich ist die ausgewählten Moleküle auf Graphen nachträglich zu modifizieren (infolge dessen auch Graphens Fermi Energy) ohne signifikante Defekte an Graphen zu erzeugen. Letztendlich waren in fälle der verwendeten Moleküle die allgemeinen Änderungen im Ladungstransfer nach der zweiten Modifikation relativ schwach, könnten aber durch gezielte Synthese stärkerer Moleküle verbessert werden.

Zur Vertiefung der Einblicke in nicht-kovalentes Dotieren von Nanomaterialien wurden alle erworbenen Kenntnisse und Erfahrungen mit Graphen auf Molybdändisulfid ( $\text{MoS}_2$ ) übertragen, um zu erkunden ob die Regeln der Struktur-Effekt Beziehung, die von Graphen abgeleitet wurde auch auf ander Klassen von Nanomaterialien übertragen werden kann und wie sich die Ergebnisse hinsichtlich der theoretischen Überlegungen entwickeln. Da die Selbstorganisation der aromatischen Moleküle auf Graphen hauptsächlich durch  $\pi$ - $\pi$  Wechselwirkungen gesteuert wird, zeigt sich bei  $\text{MoS}_2$ , dass die Akzeptorstärke nicht nur für die Dotierung, sondern auch für die Abscheidung der entscheidende Faktor ist.

# Contents

<b>Abstract</b>	<b>i</b>
<b>Kurzzusammenfassung in deutscher Sprache</b>	<b>iii</b>
<b>1 Introduction</b>	<b>1</b>
<b>2 Background</b>	<b>3</b>
2.1 <i>N</i> -Heteropolycycles . . . . .	3
2.1.1 Tetraazapentacenes . . . . .	3
2.1.2 Tetraazaperopyrenes . . . . .	5
2.1.3 Heterotriangulenes . . . . .	6
2.1.4 Benzonaphthyridines . . . . .	7
2.2 Graphene . . . . .	8
2.2.1 Overview . . . . .	8
2.2.2 Growth and Exfoliation . . . . .	9
2.2.3 Fundamental Electronic Properties . . . . .	10
2.2.4 Vibrational Properties and Raman Spectroscopy . . . . .	13
2.2.5 Doping strategies . . . . .	17
2.2.6 Characterization of non-covalently doped Graphene . . . . .	19
<b>3 Non-Covalent Molecule/Graphene Heterostructures</b>	<b>28</b>
3.1 Introduction . . . . .	28
3.2 Sample Preparation and Deposition . . . . .	31
3.3 Deposition of Tetraazapentacene Derivatives (TIPS-TAPs) . . . . .	36
3.4 Deposition of Tetraazaperopyrenes . . . . .	44
<b>4 Post-deposition Modification: UV Treatment and Protonation</b>	<b>54</b>
4.1 UV-Treatment of Triangulenes (HTAs) . . . . .	55
4.2 Protonation of Benzonaphthyridines . . . . .	62
<b>5 Beyond Graphene: <i>N</i>-Heteropolycycles on Molybdenumdisulfide</b>	<b>65</b>
5.1 Introduction . . . . .	65
5.2 Vibrational properties and Raman spectroscopy of MoS <sub>2</sub> . . . . .	68
5.3 Deposition of <i>N</i> -Heteropolycycles . . . . .	70
<b>6 Conclusions and Outlook</b>	<b>85</b>
<b>7 Bibliography</b>	<b>92</b>

<b>8</b>	<b>Experimental Parameters</b>	<b>93</b>
8.1	UV-Vis/Absorbance Spectroscopy . . . . .	93
8.2	Raman Spectroscopy . . . . .	93
8.2.1	Measurements on Graphene . . . . .	93
8.2.2	Measurements on MoS <sub>2</sub> . . . . .	94
8.3	FM-KPFM . . . . .	94
<b>9</b>	<b>List of Frequently Used Abbreviations</b>	<b>96</b>
<b>10</b>	<b>List of Figures</b>	<b>97</b>

# 1 Introduction

Electronics today are mostly based on semiconducting metals like for example silicon, but to improve technology, research is done with other materials that have potential to help making the step to more advanced applications like flexible and wearable electronics or more efficient energy collection through solar cells. In this work two major fields of research regarding new materials for electronic applications are addressed and combined. The first focus lies on small organic molecules that can be used as semiconducting materials in organic electronics. Regarding those small molecules most of them are aromatic systems that show semiconducting properties in films or single crystals. Due to the nature of having organic molecules in contrast to metals it is possible to realize circuits on bent or flexible surfaces. The possible structure motifs and substitutional patterns for molecules in electronics is vast and there is a lot of effort in current research going on to identify structures in combination with analysis of their properties to find the most promising materials. As one of the most prominent representative one has to mention rubrene. A lot of research was done until now on rubrene as a benchmark molecule showing, for non-metallic materials, high performance properties<sup>1-3</sup>. Another field of research where small organic molecules are of interest is for the fabrication of more efficient solar cells. There is a lot of research going on to utilize singlet fission to achieve higher energy conversion efficiencies.<sup>4,5</sup>

Apart from organics there are other promising materials that might help shaping future electronics. One- and two- dimensional nanomaterials like carbon nanotubes (1D) or Graphene (2D) show a plethora of interesting properties that can be utilized in a variety of different applications from transistors to sensors and electrochemistry<sup>6,7</sup>.

This work however does not focus on either organic semiconductor nor 2D-nanomaterial alone. The overarching aim of this research projects was to shape the properties of 2D-materials through charge transfer interactions of organic semiconductors to fabricate materials whose properties can be precisely tuned by changing the adaptable properties of the small molecules that can easily be changed by synthesis. With graphene being a rather well understood and researched material it serves as the perfect model system when combining both small organic semiconductors and 2D-material to establish protocols to entangle all the interactions between both materials to then construct a structure-effect relationship that can be used to further fine tune both materials to the desired properties that are needed for specific applications.

Setting the experimental results into context will be done by first giving an overview over all the different classes of molecules that were investigated. The focus here will mainly be towards their structure and resulting physical and chemical properties and less on their synthesis.

With graphene being the second important material under investigation a detailed look into its electronic properties and resulting vibrational properties is given to set the stage for an in depth understanding of the changes introduced through molecular doping and the necessary spectroscopic evaluation followed by an overview of the general doping strategies and the methodology for characterization of doped graphene.

The experimental work is split in three major parts that follow a somewhat chronological path through the research process starting with formulating a standard sample preparation procedure to guarantee comparable and reproducible results throughout every measurement. This procedure includes a sophisticated cleaning of the commercial CVD-grown graphene to minimize environmental effects influencing its electronic structure, as well as establishing a standard wet-deposition protocol for the polycyclic molecules. After establishing this groundwork TIPS-TAPs and TAPPs are deposited onto graphene to evaluate their acceptor strength with regard to the doping effects on graphene using Raman spectroscopy and Kelvin-Probe-Force Microscopy.

The second major section then utilizes the gained insights from the experiments done with TIPS-TAPs and TAPPs to take the non-covalent modification of graphene one step further by introducing secondary shifts of the electronic properties by modifying the deposited Heterotriangulenes and Benzonaphthyridines with UV irradiation and acid treatment respectively.

The last station on this experimental journey will take all the knowledge deduced from the experiments with the model system graphene to take the experiments beyond graphene by applying the established deposition protocols and measurement procedures onto another famous 2D-nanomaterial, namely Molybdenumdisulfide to see both differences and possible similarities between the results on graphene and MoS<sub>2</sub> to deepen the understanding of charge transfer interactions and self assembly on both material systems.

## 2 Background

### 2.1 *N*-Heteropolycycles

As already mentioned there is a vast variety of polycyclic aromatic compounds that can be employed in organic electronic devices. In this work the focus lies on so called *N*-Heteropolycycles a class of materials that have nitrogen incorporated into the polycyclic carbon structure to influence the electronic properties.

#### 2.1.1 Tetraazapentacenes

One of the more successful organic semiconductors apart from rubrene can be seen in pentacene (figure 2.1, a), a p-type semiconductor which is also widely used as a benchmark molecule.<sup>8,9</sup> Introducing nitrogen into the pentacene structure however will lead to n-type behavior, and with field effect mobilities of over  $10 \text{ cm}^2\text{V}^{-1}\text{s}^{-1}$  the most successful molecule that results from that is tetraazapentacene (figure 2.1, d). The major drawback with both pentacene and its nitrogen rich counterpart is that both molecules show very low solubility in organic solvents and are prone to oxidation.<sup>10</sup> To still be able to process those types of molecules out of solution and achieve long term environmental stability some changes to the structure have to be done. This is mostly done by adding a tri-isopropyl-silyl-group (TIPS) to the center ring of the backbone to prevent oxidation (figure 2.1, b-c) and enhancing solubility, making it possible to process those molecules out of common solvents like toluene.<sup>11,12</sup>

The TIPS-group will however not only affect the stability and solubility but also due to its rather large steric impact change the stacking pattern and distance between the molecules themselves. This results for pentacene in a herringbone structure in thin films, while TIPS-pentacene will be oriented in a brick wall pattern.<sup>13</sup> Further variation of the electronic properties of TIPS-TAP can be achieved by adding halogen substituents to the acene backbone (figure 2.1, e), which results in a lowering of the LUMO-energy making them even stronger acceptor-type molecules.<sup>14</sup>

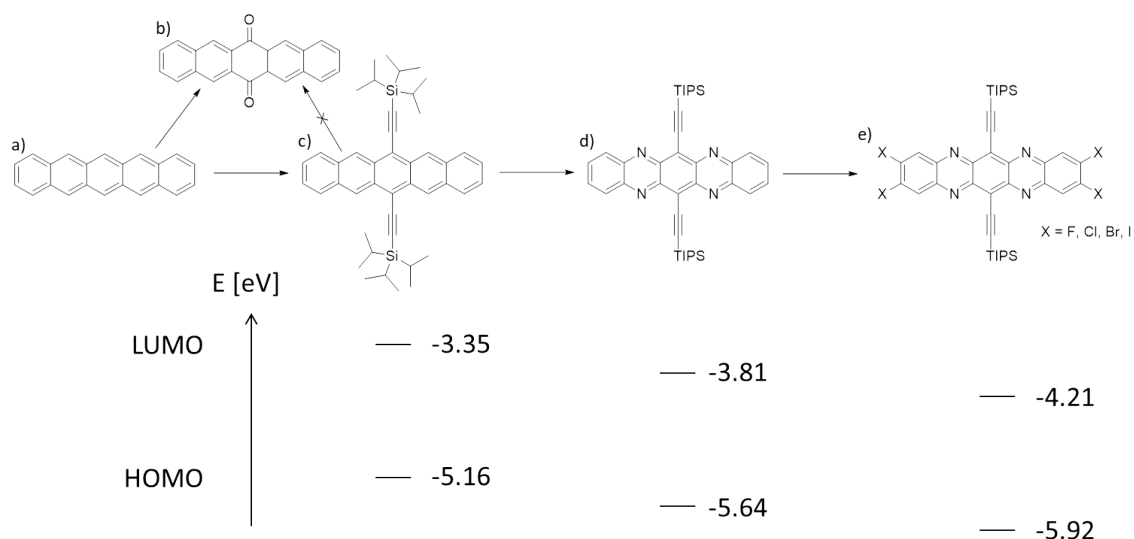


Figure 2.1: Logical evolution of the tetraazapentacene structure and its HOMO/LUMO energy, starting with pentacene (a). To avoid oxidation of the acene structure (b), triisopropyl-silyl groups are added to the center ring (c). Introducing nitrogen into the backbone decreases HOMO and LUMO energy<sup>15</sup> compared to TIPS-pentacene<sup>16</sup> (d). Additional decrease of HOMO/LUMO energy is achieved by additional substitution with halogen atoms<sup>14,15</sup> (e). Energies for the halogen substituted molecules, differ only slightly from one another and thus are summarized here in two values for demonstrative purpose.

### 2.1.2 Tetraazaperopyrenes

Another interesting class of heteropolycycles that show acceptor behavior are Tetraazaperopyrenes. In general these molecules can be considered as molecules similar to perylene-tetracarboxydiimides (PDI) regarding their photochemical properties and are extended pyrene (figure 2.2) systems.<sup>17</sup> If one formally extends pyrene by one extra pyrene unit it will result in peropyrene (figure 2.2,a) Lowering the LUMO-energy of peropyrene can be done similarly to azapentacenes by first introducing nitrogen into the acene structure, followed by halogen substituents (figure 2.2, b).<sup>18</sup> Decreasing the energy-gap in their case achieved by adding more complex substituents like different thiophene-units that additionally affect the packing properties of these molecules<sup>19</sup> in a similar fashion as the TIPS-group does with pentacene. Regarding solubility the TAPP with no substituents at all shows rather poor solubility in common organic solvents which again can be an issue for processing these materials. To overcome this obstacle it is possible to add perfluor-sidechains that will enhance solubility with subsequent changes to the overall LUMO-energy.<sup>20</sup>

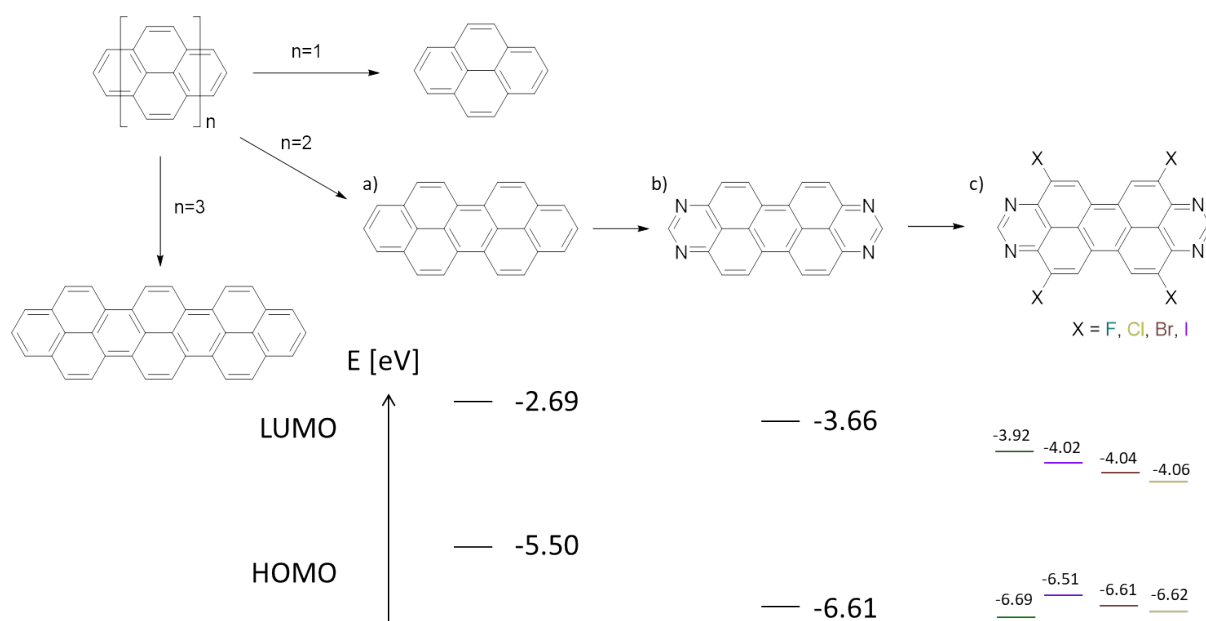


Figure 2.2: Overview of the pyrene molecule family and the changes in HOMO/LUMO energies from peropyrene<sup>21</sup> (a) to tetraazaperopyrene<sup>18</sup> (b) to tetra halogenated tetraazapentacene<sup>18</sup> (c). Peropyrene can be seen as a formal extension of the pyrene structure by adding an additional pyrene unit. Adding another pyrene unit will result in teropyrene and so on. The halogenated HOMO/LUMO energies are color coded to their respective halogens.

### 2.1.3 Heterotriangulenes

With TAPP and TIPS-TAP being p-type (acceptor) molecules it is necessary to also take a look at donor (n-type) molecules. Here the Heterotriangulenes come into play. This class of molecules can be described as bridged triphenylamines resulting in a planar triangular structure of six carbon rings with a center nitrogen atom. Depending on their composition regarding the bridging groups between the phenyl units they can be both donor and acceptor or even open-shell systems.<sup>22</sup> Relevant for us are the donors with  $-CMe_2$  bridges. One further property that can be explored is the conversion of those molecules to stable radical cations resulting in a acceptor-type structure.<sup>23</sup> A second interesting possibility to tune the HOMO-LUMO properties of Triangulenes it to change the center heteroatom from nitrogen to for example boron or phosphorus Changing the center to phosphorus however will lead to a geometrical change of the originally planar molecule to a more bowl-shaped geometry due to the structural constraint introduced with the larger P-atom.<sup>24</sup>

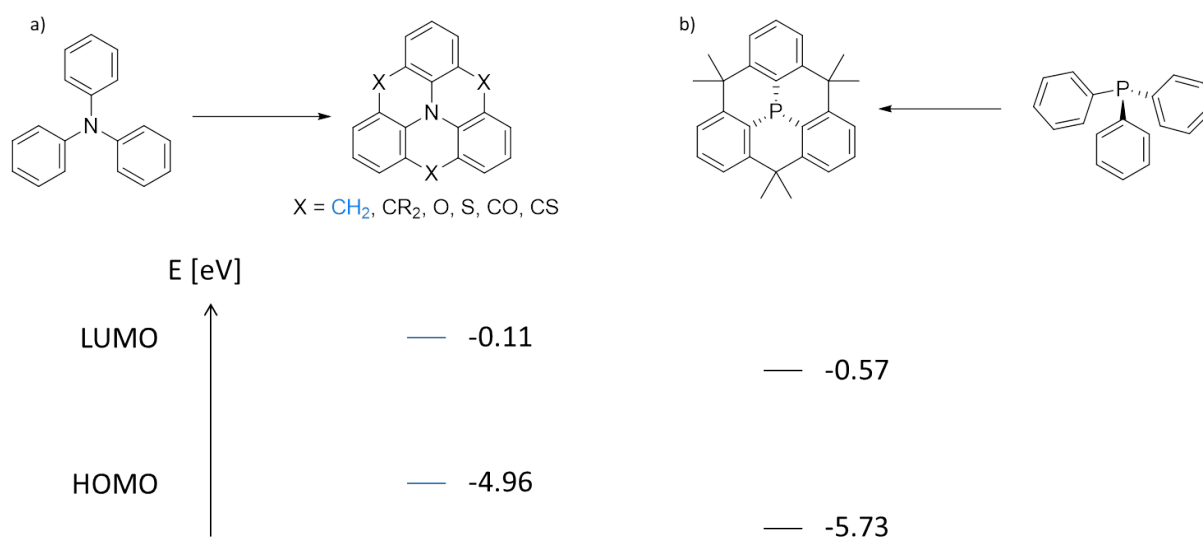


Figure 2.3: General conceptual overview of heterotriangulenes. Bridging of a triphenylamine leads to a planarization of the molecular structure (a). The bridging can be done with several different structures, from heteroatoms like oxygen or sulfur to carbonyl or  $-CR_2$  functionalities.<sup>24</sup> Changing the center atom from N to P will lead to a non planar structure due to the initial structural constraint of the larger phosphorus (b). For comparison of the HOMO/LUMO<sup>25</sup> energies (bottom) only one relevant example for each heterotriangulene is displayed for simplicity.

### 2.1.4 Benzonaphthyridines

The last molecular structure pattern that was examined can be categorized under the name Benzonaphthyridines. At the current state of research these specific molecules are rather unknown but can essentially be described as an extension of quinoxalinophenanthrophenazines (QPPs)<sup>26</sup> by incorporating a 1,8-naphthyridine unit<sup>27,28</sup> on both sides of the long axis of the molecule backbone. Similar molecules however, without the naphthyridine unit but with a pyridine unit were synthesized and investigated regarding their photochemical and charge transport properties revealing them as promising materials.<sup>26,29</sup> Again to increase the solubility by reducing the intermolecular  $\pi$ - $\pi$  interactions those molecules have *tert*-butyl substituents attached to the core pyrene unit<sup>26</sup>.

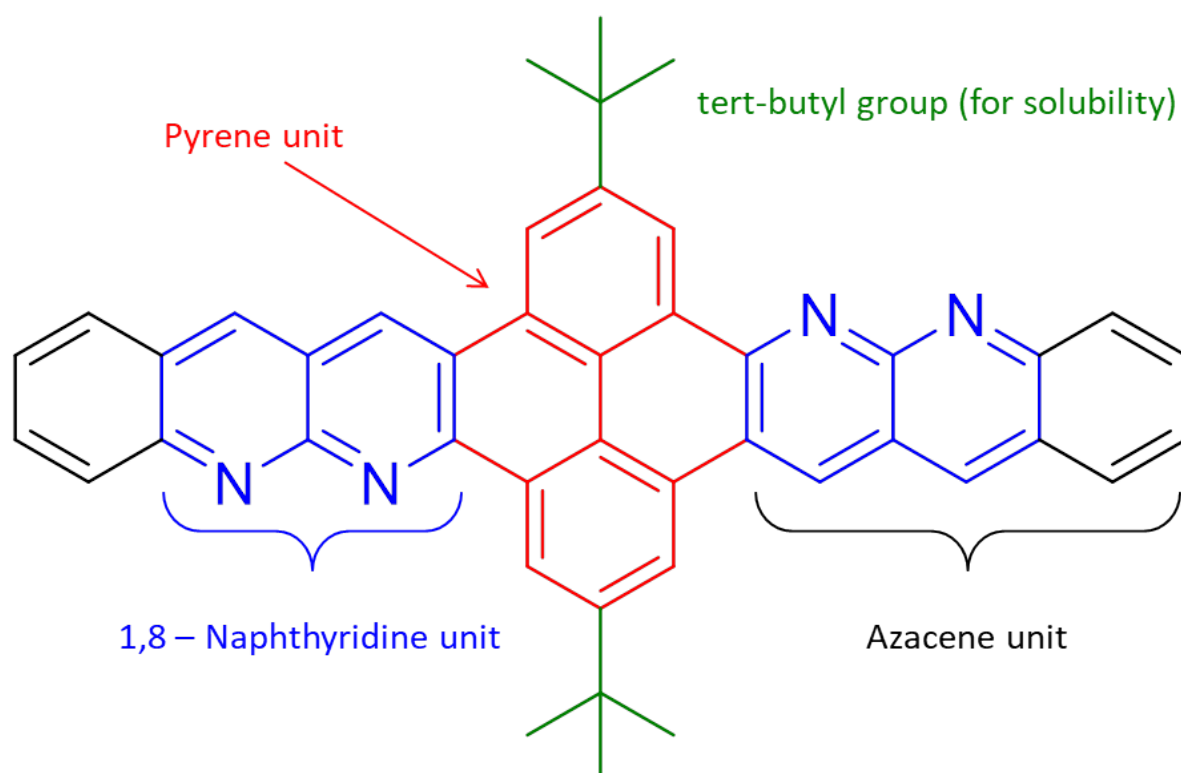


Figure 2.4: Structural composition of benzonaphthyridine to derive the principle of its molecule structure that combines several well known building blocks for organic electronics. It can be seen as two acene units containing a 1,8-Naphthyridine unit (blue) that are fused via a pyrene core (red). To increase solubility tert-butyl groups are added to the pyrene unit (green).

## 2.2 Graphene

### 2.2.1 Overview

Since its discovery in the early 2000s followed by the Nobel Prize of Andre Geim and Konstantin Novoselov<sup>30,31</sup> for their work in 2010, graphene gained a lot of attention as new and promising material for all different kinds of applications; from electronics to enhanced materials.<sup>7,32,33</sup> Strictly speaking graphene describes one layer of a two-dimensional, hexagonal lattice of sp<sup>2</sup>-hybridized carbon atoms. Two layers of graphene are usually denoted as bilayer graphene (BLG) and everything consisting of 2-10 layers is usually called multilayer graphene, though there is still some general confusion about nomenclature of graphene based materials (GBM) like for example where to draw the line in layer number between graphite and GBM<sup>34</sup>.

Graphene plays nowadays a role in lots of different branches of material sciences and device research. With possible thermal conductivities around 2000  $\frac{W}{mK}$ <sup>35,36</sup> and high mechanical strength<sup>37</sup> it is a promising strengthening additive for a variety of materials<sup>38</sup>. Due to its high conductivity<sup>39</sup> in combination with an optical transparency of about 97 %<sup>40</sup> it has a high potential to be utilized as transparent electrodes for displays, smart windows, solar cells etc.<sup>41</sup> Super capacitors with graphene show also a lot of potential for future energy storage applications.<sup>7</sup>

The modification of graphene also plays a major role in all those branches of research, due to its unique properties, discussed in section 2.2.3 that in some applications have to be tuned to the specific needs. As shown later, opening a bandgap in graphene is one of the crucial modifications for its applicability in anything electronics related due to the need of semiconducting materials, but depending on the process that is employed for this a lot of different changes apart from just opening a band gap can occur, thus making an in depth evaluation of not only the doping but also structural and surface changes of graphene most important.

Because this work is focused on modifying mainly electronic properties of graphene the following sections will give, apart from the methods to obtain graphene, a detailed rundown on the fundamental electronic properties of graphene as well as the resulting spectroscopic fingerprint that is used to identify changes in its electronic structure and how these changes can be achieved and characterized.

## 2.2.2 Growth and Exfoliation

Research on how to gain access to graphene brought forth a huge variety of different methods to synthesize it, that can be roughly separated into two different approaches, namely top-down and bottom-up processes.<sup>42</sup> Top-down processes usually describe methods where graphite is used as a starting material from which ideally single layers of graphene are separated. This includes the scotch tape method (also known as micro mechanical cleavage)<sup>39</sup>, all kinds of liquid phase exfoliation<sup>43</sup> and electrochemical exfoliation.<sup>44</sup>

The scotch tape method was famously used by Geim and Novoselov<sup>31,39</sup> to separate a single graphene layer from graphite. Today there are improved methods that lead to a low defect density and rather large graphene sheets.<sup>45</sup>

As mentioned above another method to separate a layered material into its (single) layers, Liquid phase exfoliation (LPE) can be applied<sup>43</sup>. Hereby, the graphite can be dispersed in *N*-Methylpyrrolidone (NMP) and treated with bath sonication to achieve a graphene layer separation and the resulting graphene dispersions can be up to a concentration of 0.01 mg/ml<sup>43,46</sup>. Electrochemical exfoliation on the other hand uses not an outside force like sonication but utilizes ion intercalation as a driving force to separate the material layers.<sup>44</sup>

All those methods produce rather small flakes of the material but often a large, monolayer-like coverage is needed for device applications. In this case one can resort to Langmuir-Blodgett films to produce a large coverage of a desired substrate.<sup>47</sup>

A different approach to graphene can be realized by direct growth from precursor materials via chemical vapor deposition (CVD) on copper foil<sup>48,49</sup>. For further use the graphene then has to be transferred from copper to the desired substrate via either a dry- or wet-transfer process<sup>50</sup>. In both cases a transfer polymer (mostly PMMA) is coated on the graphene to enable etching of the copper foil. After deposition of graphene on a substrate the transfer polymer is removed via organic solvents. This process leads to large monolayer coverages but leaves behind polymer residues and water that have to be removed in further cleaning procedures<sup>51</sup>.

### 2.2.3 Fundamental Electronic Properties

To understand the unique electronic properties of graphene one has to look first at the honeycomb lattice itself. As shown in figure 2.5 this lattice can be realized with a unit cell of two atoms in a triangular lattice orientation with the resulting lattice vectors

$$\mathbf{a}_1 = \frac{a}{2}(3, \sqrt{3}), \quad \mathbf{a}_2 = \frac{a}{2}(3, -\sqrt{3}) \quad (2.1)$$

where  $a$  stands for the distance between two carbon atoms of 1.42 Å. To further understand and work out the underlying quantum mechanical properties this real space lattice has to be converted to its corresponding Brillouin zone, which represents the real space lattice in the reciprocal space (k-space, with vectors  $k_x$  and  $k_y$ ). To describe the k-space lattice the real space lattice vectors  $\mathbf{a}_1$  and  $\mathbf{a}_2$  can be written as their reciprocal counterparts  $\mathbf{b}_1$  and  $\mathbf{b}_2$  with

$$\mathbf{b}_1 = \frac{2\pi}{3d}(1, \sqrt{3}), \quad \mathbf{b}_2 = \frac{2\pi}{3d}(1, -\sqrt{3}). \quad (2.2)$$

The important symmetry points are  $\Gamma$  that describes the center of the first Brillouin zone, M the center of a rectangular face of the reciprocal lattice and K (or K') which are the center points of an edge and have, regarding graphene special properties discussed below.

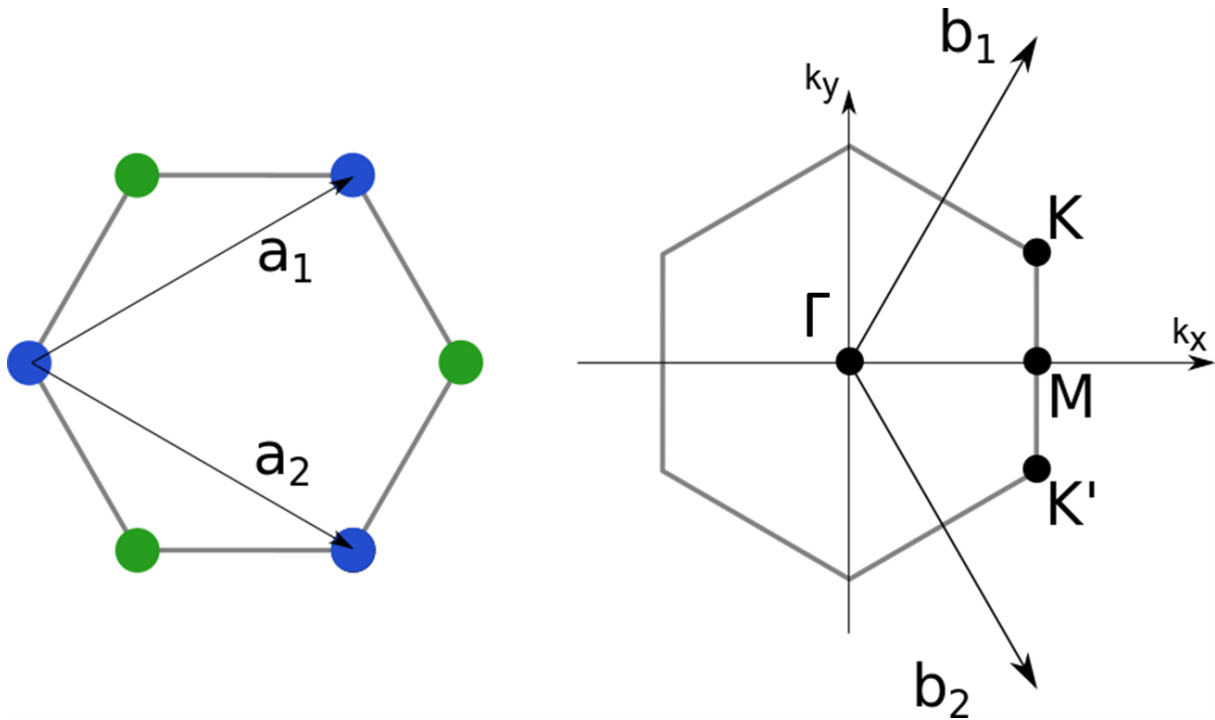


Figure 2.5: Graphene unit cell with lattice vectors  $\mathbf{a}_1$  and  $\mathbf{a}_2$  (left) and corresponding Brillouin zone (right). Reciprocal lattice vectors are denoted as  $\mathbf{b}_1$  and  $\mathbf{b}_2$  and important lattice points are marked as explained in the text above.

With this Brillouin zone the electronic dispersion of the graphene lattice can now be calculated. Further and more in depth information on the theoretical calculations and background can be found in the literature<sup>52–54</sup> but looking at the resulting band structure<sup>52</sup>

$$f(\mathbf{k}) = 2\cos(\sqrt{3}k_y a) + 4\cos\left(\frac{\sqrt{3}}{2}k_y a\right)\cos\left(\frac{3}{2}k_x a\right) \quad (2.3)$$

visualized in figure 2.6 one can see the special property emerging at the K (or K') point. Those points in the  $k$ -space of graphene are called Dirac points due to the fact that the resulting energy dispersion<sup>52</sup>

$$E_{\pm}(\mathbf{q}) \approx \pm v_F |\mathbf{q}| + O[(q/K)^2] \quad (2.4)$$

at those points can be described, with the momentum  $q$  relative to the Dirac points, as ultrarelativistic particles with the massless Dirac equation.

The density of states (DOS) at the K-point can be derived from Eq. 2.4 as

$$\rho(E) = \frac{2A_c |E|}{\pi v_F^2} \quad (2.5)$$

with the Fermi velocity  $v_F \approx 10^6 \frac{m}{s}$  and the area per unit cell  $A_c = 3\frac{\sqrt{3}a^2}{s}$ .

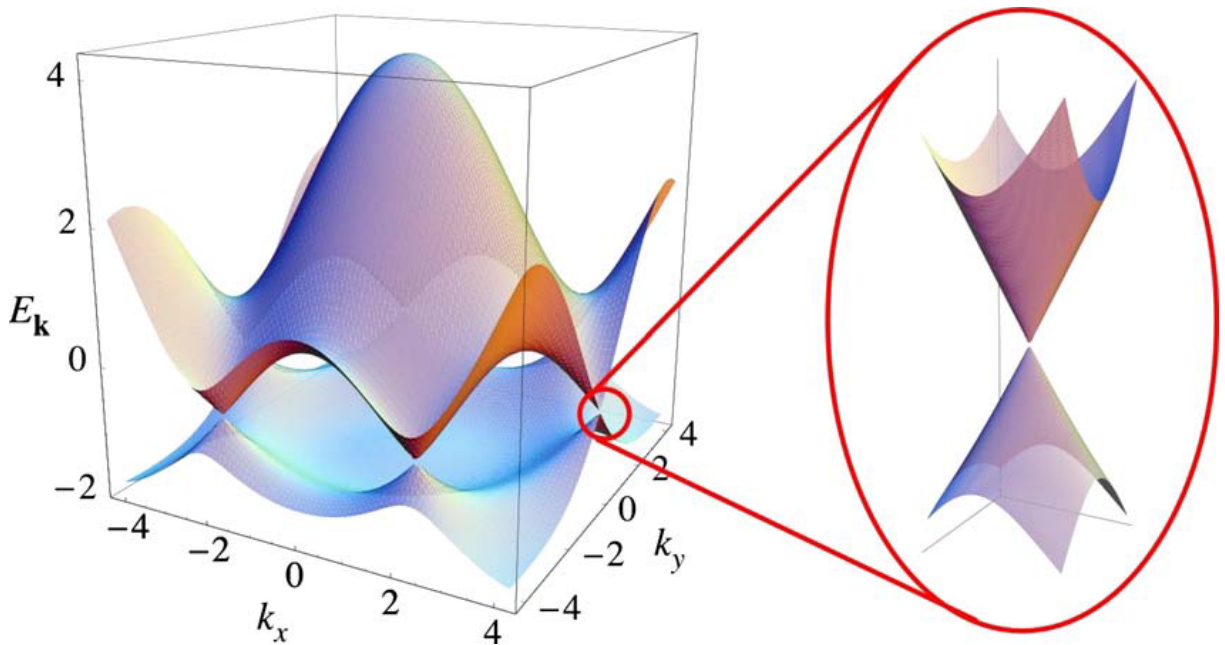


Figure 2.6: Energy dispersion for the graphene unit cell with a zoom in on the Dirac point. Adapted from Neto *et al.*<sup>52</sup>

This unique feature of a DOS of zero at the Fermi level leads to several outstanding properties which make graphene such a promising material for future electronics. Charge carrier mobilities in graphene range from  $25000 \frac{cm^2}{Vs}$  on different substrates up to over  $200000 \frac{cm^2}{Vs}$  in suspended graphene. This transport occurs for electrons and holes alike (ambipolar transport) and with a mean free path-length of up to  $1 \mu m$  showing ballistic transport.<sup>52</sup>

Another important electronic property that can be derived from the DOS is the work function of graphene. Fig 2.7 shows the relation between Fermi energy and measurable work function  $W$  at the K-point.  $W_0$  describes here the work function of neutral graphene that gets shifted with the Fermi energy  $E_F$  relative to the vacuum energy  $E_V$ . One of the most relevant areas where the work function come into play can be observed in fabrication of electric devices due to the charge transfer between materials being the most effective with matching Fermi levels that are reflected in the work function.<sup>56</sup> Thus it is of high importance to closely examine changes in work function in Graphene to make sure later implementation in electronic devices can be done successfully. As one can already fathom from figure 2.7 due to the work function being dependent on the Fermi energy it will change with doping level and as a result can be a complementary tool to evaluate charge transfer interactions between graphene and doping agents. Further in depth explanations of utilizing the work function for characterization will be done in chapter 2.2.6.

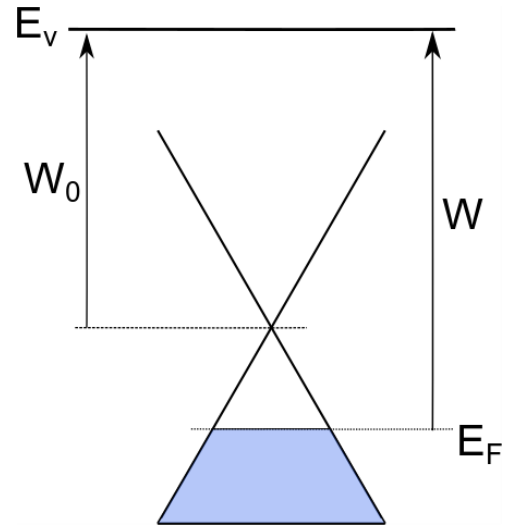


Figure 2.7: Schematic representation of the Dirac cone at the K point of the graphene unit cell and the relation of the Fermi energy  $E_F$  to the sample work function  $W$ . The vacuum energy is denoted as  $E_V$  and  $W_0$  represents the work function of neutral graphene.<sup>56</sup>

## 2.2.4 Vibrational Properties and Raman Spectroscopy

One of the most powerful tools to investigate graphene comes in the form of Raman spectroscopy. A single Raman spectrum of graphene contains a huge amount of different information. Properties like strain, layer number, defects and for us most important, doping<sup>57–61</sup> can be identified using Raman spectroscopy. Figure 2.8 shows a comparison of typical Raman spectra of graphite and graphene. The two most prominent bands are the G- and 2D-band at  $\sim 1585\text{ cm}^{-1}$  and  $\sim 2680\text{ cm}^{-1}$  respectively.<sup>62</sup>

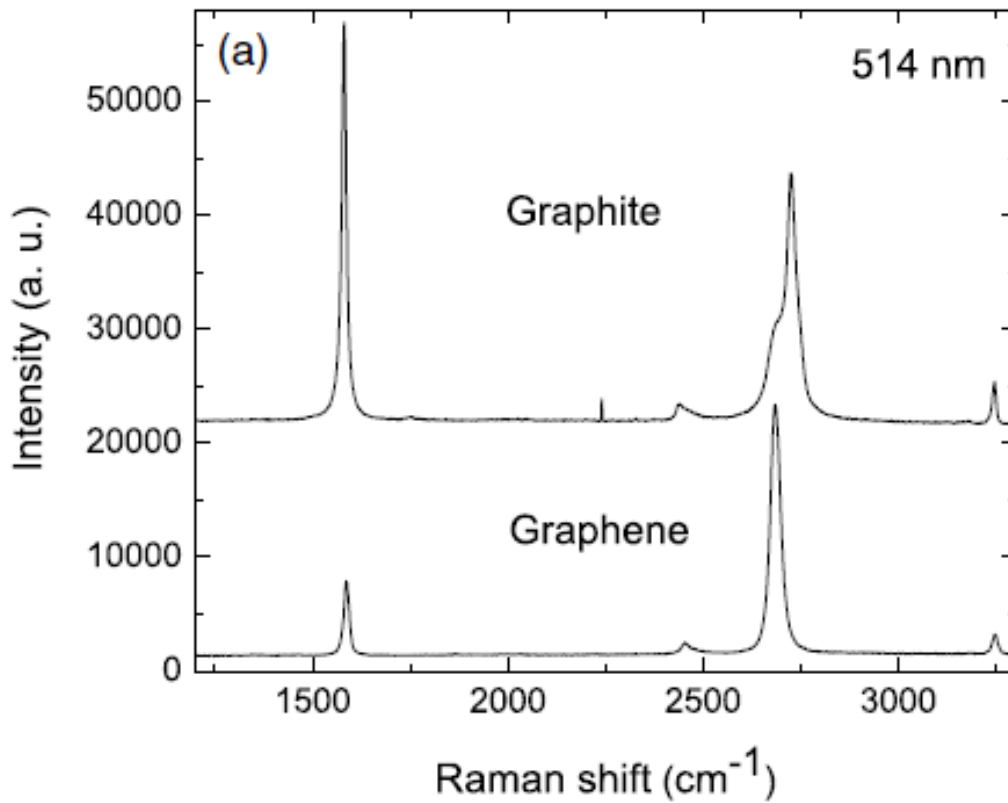


Figure 2.8: Comparison of Raman spectra for graphite (top) and graphene (bottom) at an excitation wavelength of 514 nm. Both spectra show the typical Raman signals with a G-band around  $1585\text{ cm}^{-1}$  and a 2D-band around  $2680\text{ cm}^{-1}$ . The main difference between graphite and graphene lies in the intensity ratio of both signals and the 2D-band being a single symmetrical Lorentzian for graphene.<sup>62</sup>

Those two signals are the main source of information on graphene properties, but to fathom how this information is available in those vibrations one has to understand the physical processes that govern the shape of the graphene Raman spectrum. The key to that is the phonon dispersion as it is shown in figure 2.9.

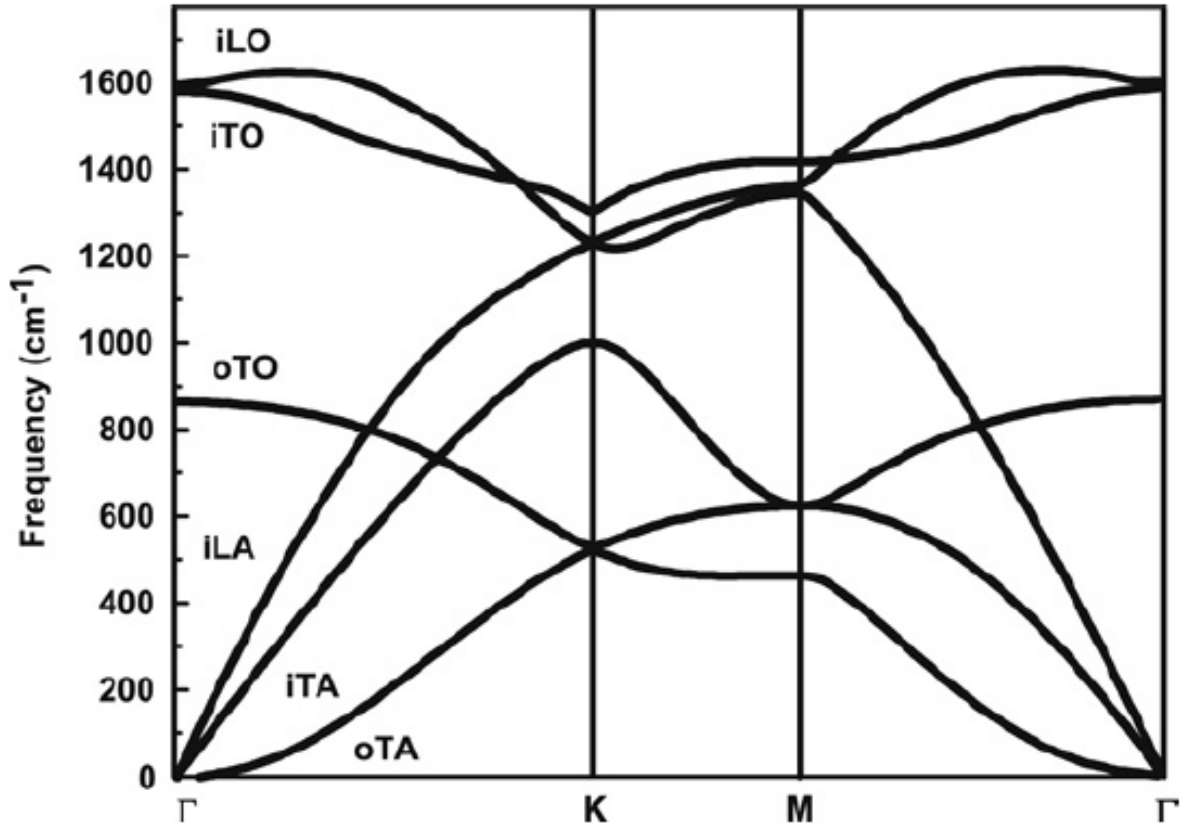


Figure 2.9: Calculated phonon dispersion for graphene along the  $\Gamma$ -K-M- $\Gamma$  direction. In total, six phonon branches can be observed of which the iLO and iTO phonons are relevant for Raman spectroscopy of graphene. Plot adapted from Ref<sup>61,63</sup>

As worked out in the previous section the unit cell of graphene consists of only two atoms that result in six different phonons, with three being acoustic (A) and three optical (O). Those two categories can be divided again by their vibration direction compared to the graphene plane into in- and out-of-plane phonons (i and o). With that one gets two in-plane vibrations for both optical and acoustic phonons as well as one out-of-plane remaining for each of them. The third and last parameter to precisely identify phonons is by their direction in regard to the carbon-carbon bond. Phonon vibrations along the C-C bond are denoted as transversal (T) and longitudinal (L) if perpendicular to the carbon bond (2.11). With this characterization the important phonons that are observable in Raman spectra can be identified as both optical and in-plane phonons. The G-band ultimately results from two degenerate carbon-carbon stretching vibration of the iTO and iLO phonon at the  $\Gamma$ -point of the Brillouin zone. These two modes will scatter either the hole or electron that is created with optical excitation only to recombine under emission of light with less energy than the original excitation due to energy transfer to the phonon itself. The process behind the 2D-band involves the iTO phonon at the K-point and a double resonance process where either the electron or hole of the initial excitation is scattered

inelastic to the  $K'$ -point by the iTO phonon to then recombine after backscattering by another iTO phonon. This backscattering has to occur due to the energy conservation of the Raman process. The 2D-band formation is not only limited to this double-resonance process but can also happen via a triple-resonance process that involves a simultaneous scattering of both electron and hole to the  $K'$ -point by the iTO phonon to recombine and emit radiation from there. In addition to the G- and 2D-band the D-band plays an essential role in the Raman spectrum, for it being related to defects thus revealing information about the graphene quality. The mechanism of the D-band formation is comparable to the 2D-band double-resonance process with the difference that the electron (or hole) is elastically scattered from the  $K'$ -point back to the  $K$ -point by the iTO phonon for recombination. As momentum has to be again conserved a breaking of symmetry (i.e. a defect) is needed for that process. One minor feature that can be observed with defects is the  $D'$ -band near the G-band that is the result of a double-resonance process at the  $K$ -point without any participation of the  $K'$ -point and again the necessity of a defect. All scattering processes are depicted schematically in figure 2.10.

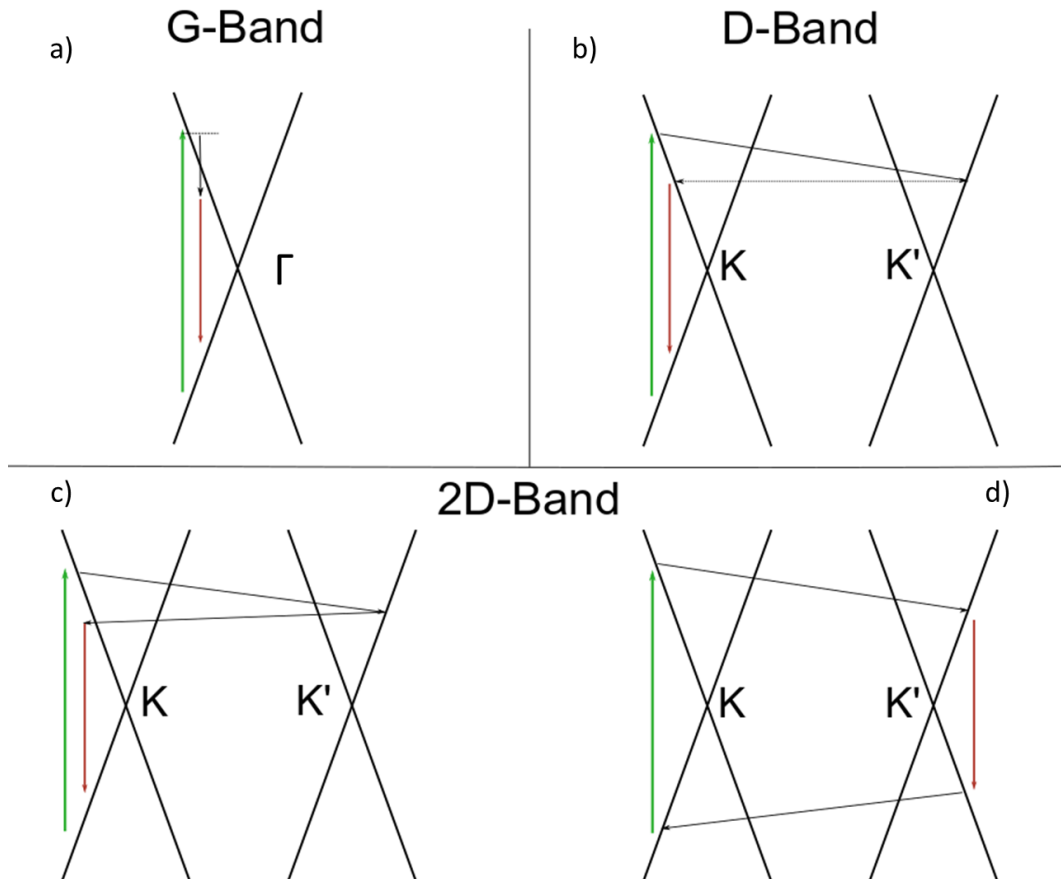


Figure 2.10: Phonon scattering processes leading to the main observable Raman modes of graphene. a) single resonance process at the  $\Gamma$  point leading to the G-band. b) defect mediated double resonance at the  $K$  (and  $K'$ ) point leading to the D-band. c) and d) double and triple resonance respectively at the  $K$  (and  $K'$ ) point resulting in the 2D-band.

A schematic illustration of the actual phonon vibrations relative to the graphene lattice are depicted in figure 2.11.

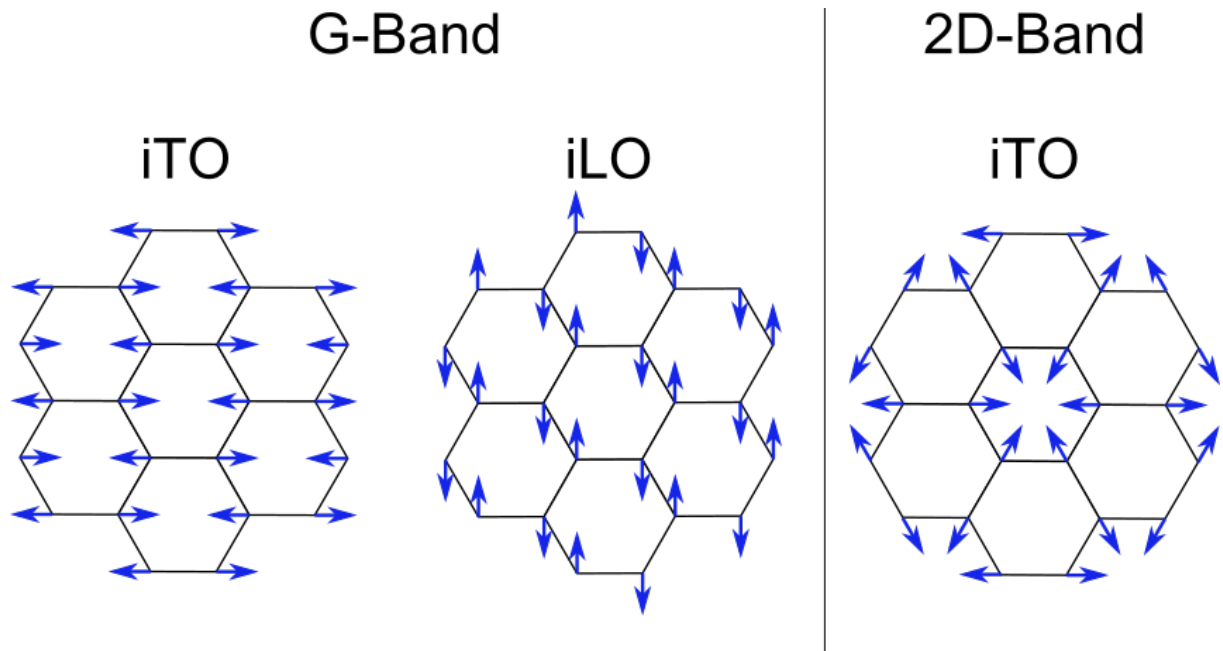


Figure 2.11: Schematic illustration of the phonon vibrations for the two main Raman signals of graphene. Left: the doubly degenerate iTO and iLO phonons at the  $\Gamma$ -point responsible for the G-band. Right: Radial breathing mode of the iTO phonon at the K-point resulting in the 2D-band (and D-band with defects present).

### 2.2.5 Doping strategies

Even though graphene has many promising properties, there is one major drawback if it is to be used in electronic devices. Graphene being a zero band gap semiconductor due to its DOS of zero at the Fermi energy has low on-off ratio of  $>10$  at room temperature, which means a transistor with graphene as its semiconductor is not reliable switchable between an reliable on and/or off state. Opening a band gap and precise engineering of the DOS of graphene is therefore necessary to realize the potential of graphene in electronic devices. Figure 2.12 shows a schematic of doping in graphene where p-doping lowers the Fermi energy by extraction of electrons and n-doping raises the Fermi energy by addition of electron density.

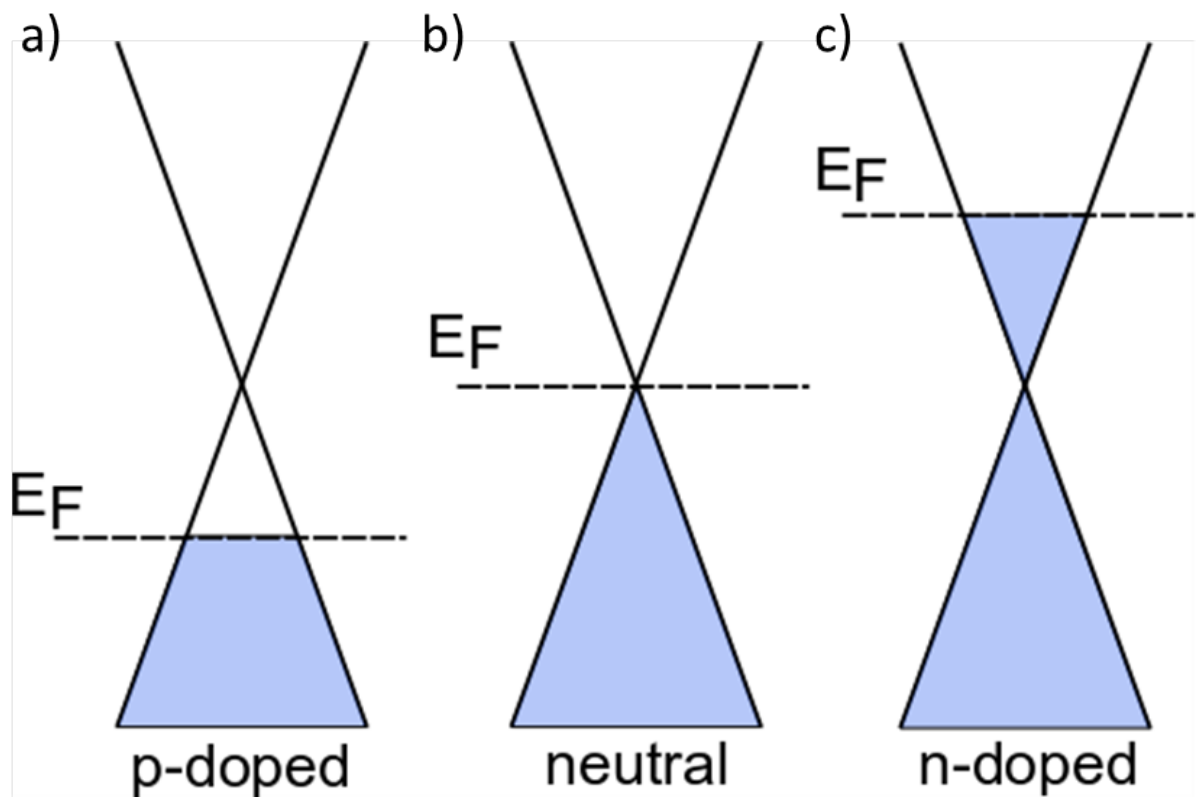


Figure 2.12: Schematic representation of the Fermi energy  $E_F$  at the Dirac points for from left to right, p-doped (electron poor), neutral and n-doped (electron rich) graphene.

Up until today many possibilities to achieve a shift in Fermi energy to open a band gap have been researched. One approach can be to utilize quantum confinement effects that erase the degeneracy of the band structure at the K points. This can be achieved by spatially reducing the graphene plane to a so called nanoribbon structure<sup>64</sup>.

The direct introduction of heteroatoms into the graphene lattice like for example nitrogen leads to n-doping or boron will lead to p-doping.<sup>65</sup> Due to its special properties even the proximity of graphene to a substrate can induce either p- or n-doping depending on the substrate<sup>65,66</sup> which has to be considered while working with anything else than annealed

and suspended graphene. Adsorbates like oxygen and water or nitrogen oxides do alter the electronic properties of graphene as well.<sup>67</sup>

Intentionally introducing defect sites by e.g. oxidation (graphene oxide, GO) and reduction (reduced graphene oxide, rGO) of graphene also gives rise to a band gap but at the major cost of losing the pristine honeycomb lattice. The same can be said for covalently attaching molecules to the graphene lattice.<sup>65</sup> A further possibility to modify graphene lies in non-covalent interactions with adsorbates on the surface that can lead from a simple surface modification to charge transfer interactions that alter the electronic structure of graphene.<sup>65,68,69</sup> All methods for graphene modification discussed until now make alterations to the hexagonal,  $sp^2$ -hybridized lattice itself inducing defects. Non-covalent interactions on the other hand leave the pristine lattice of graphene untouched and preserve the unique properties that are tied to the lattice structure. Especially aromatic molecules show due to their aromatic system and therefore strong van-der-Waals interactions with graphene<sup>70,71</sup> excellent properties for non-covalent graphene modification. Until now there has been various investigations regarding the formation of aromatic monolayers on graphene with Perylenetetracarboxylic dianhydride (PTCDA) that show a flat orientation<sup>72</sup> but also results with Perylenebisimides where a vertical orientation was observed<sup>73</sup>. Thus it is important to unveil the fundamental properties behind those self assembly mechanisms and simultaneously investigate the changes in the electronic and surface properties of graphene.

## 2.2.6 Characterization of non-covalently doped Graphene

As already mentioned in section 2.2.4 it is possible to gain insight into the Fermi level shift of Graphene that results from the charge transfer interaction of adsorbed aromatic molecules, by looking at the behavior of the G and 2D-band of the graphene Raman spectrum. As shown in figure 2.13 shifting the Fermi energy in graphene leads to several changes in Raman shifts for both G and 2D band. The G-band shifts up asymmetrical with both n- and p-doping while the 2D-band, apart from a plateau around the neutrality point increases in Raman shift with decreasing Fermi energy and vice versa. Additionally to the position the width of the G-band shows a decrease corresponding to Fermi energies unequal to the neutral state. The intensity ratio between G and 2D also shows a similar trend to the G-band width however with far less scattering of the data.

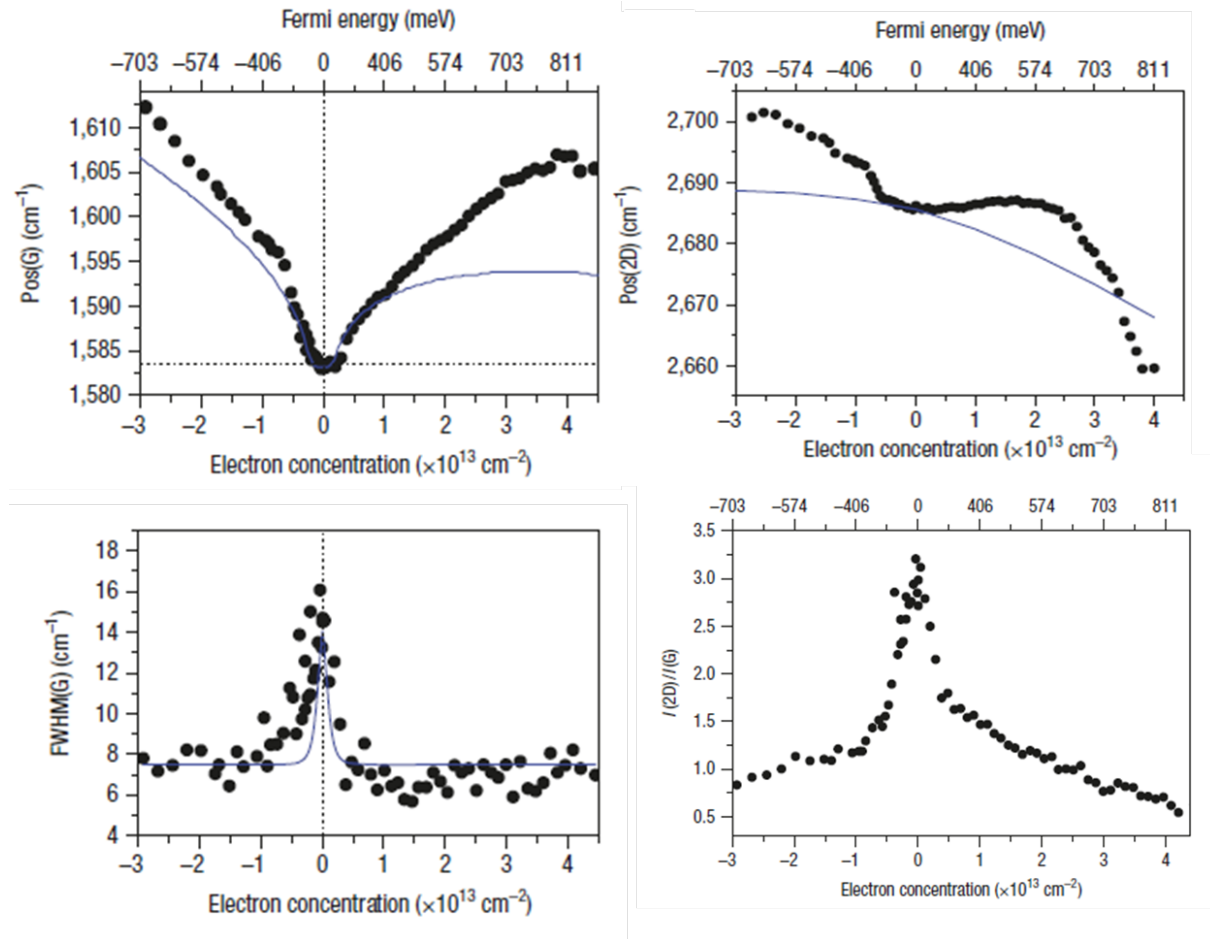


Figure 2.13: Shift of graphene Raman signals in dependence of electron concentration. Asymmetric shift of G-band position to higher wavenumbers by both increase and decrease of electron concentration (top left). Downward shift of D-band position from low to high electron concentrations. (top right). Symmetric decrease of full width at half maximum (FWHM) of G-band (bottom left) and similar shift for the intensity ratio between 2D- and G-band (bottom right). Adapted from Das *et. al.*<sup>74</sup>

Raman spectroscopy not only serves as a tool to investigate graphene but the molecules used for non-covalent interactions as well. However, especially organic dye molecules like pyrenes and similar molecules exhibit a very strong fluorescence when resonantly excited. This naturally leads to spectra that are highly contaminated with background signals that make it hard to evaluate the vibrational modes or even gain access to them at all. Luckily there is one property of graphene that enables us to record (almost) fluorescence free vibrations of the organic molecules. The charge transfer interaction that leads to doping also is responsible for this quenching<sup>68,69</sup> and thus enables us to simultaneously observe molecular vibrational intensities with graphene properties to possibly identify stacking behavior and quantities of the molecules in correlation with induced doping. Additionally to the intrinsic quenching of fluorescence by the molecule/graphene heterostructures the instrumentation of the Raman microscope plays an important role, too. Utilizing a confocal microscope setup achieves further reduction of any kind of background fluorescence to enhance the spectral quality even more. A schematic of the Raman setup used for all experiments in this work can be seen in figure 2.14. A 532 nm laser is coupled into a microscope going through an objective to be focused on the sample surface. The backscattered light then proceeds through a notch filter to drastically reduce the light that is elastically backscattered via Rayleigh scattering (hence the name "Rayleigh filter"). The light is then dispersed with an optical grating to be analyzed with a CCD detector.

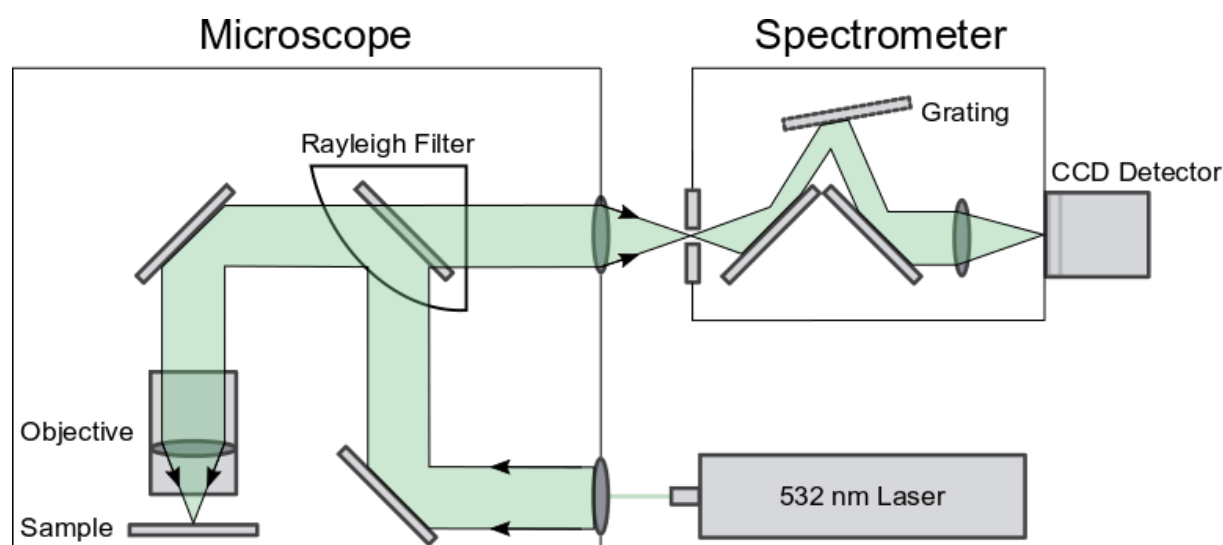


Figure 2.14: Schematic of a confocal Raman microscope setup that was employed in this work. The 532 nm laser is coupled into a microscope objective to be focused on the sample surface. The scattered light then travels through a holographic notch filter (i.e. Rayleigh filter) to drastically reduce the elastic scattered light at 532 nm. The filtered light is then coupled into a spectrometer onto a CCD detector.

With graphene being a two-dimensional material evaluation of its surface is as important as examining the intrinsic electronic properties. For that there are several methods available that can be summarized under the term of scanning probe microscopy (SPM) In general SPM stands for measurement methods that utilize a, for the experiment specific tip that interacts with the sample surface while moving in a scanning pattern. Depending on the SPM technique, different sample properties like topography, mechanical or electrical/magnetic properties can be measured.<sup>75,76</sup> The technical setup of any SPM measurement usually consists of a tip that is attached to a cantilever. This cantilever together with the tip is oscillating at frequencies of a few ten to several hundred kilohertz This oscillation will change once the tip is interacting with the sample surface. Tip-sample interactions can be an attractive/repulsive force like van-der-Waals interactions for measurements of the sample topology, electrostatic forces or potential differences between sample and tip for measurements of electric properties. To capture these changes in cantilever oscillation a Laser is reflected off the backside of the cantilever onto a photodetector. An electronic feedback loop maintains a constant force between sample and tip while scanning the sample in x-y direction. To maintain this constant force set-point the tip is moved in z-direction during the scan, according to the exerted forces between sample and tip via piezoelectric elements. The z-movement is recorded during the scan giving, together with the x- and y-movements a three dimensional representation of the surface properties.

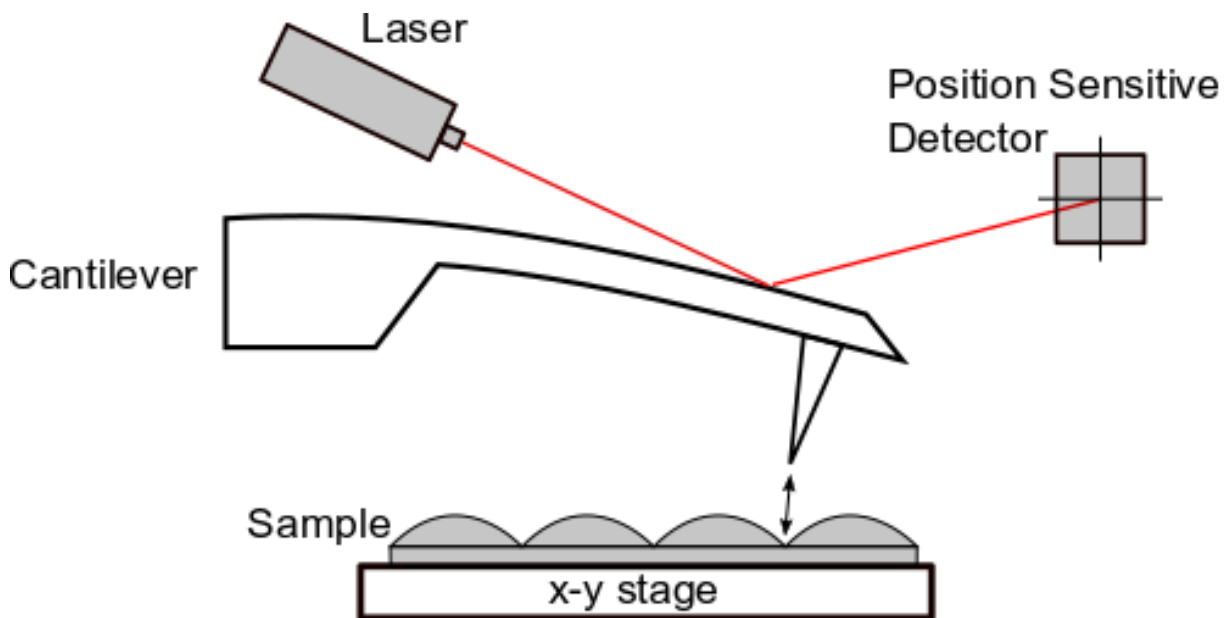


Figure 2.15: Schematic illustration of the general working principle of an AFM measurement. A oscillating cantilever with a sharp tip is moving either with direct contact or indirect contact (through interactions like van-der-Waals or electric/electrostatic forces) over the sample surface to track the profile via changes in oscillation that are observed with a laser that is reflected on the back of the cantilever onto a four quadrant detector.

Standard AFM measurements generate a height profile of the sample surface using van-der-Waals interactions of tip and sample. Hereby usually two different measurement modes are used. One possible operation of the AFM can be done in the so called "contact mode" in which the scanning tip is brought in direct contact with the surface. The second approach is called "tapping mode" in which the tip is not in constant direct contact with the surface but is oscillating a set height above the sample. With this mode the shift in oscillation frequency as well as the shifts in amplitude and phase of the cantilever oscillation can be recorded, giving additional information about the nature of the surface to construct the topological image.

While measuring AFM one has always to keep in mind that the topological image is not a real image but a constructed image. That means there are several factors influencing the image that can lead to a false representations and artifacts. One major contribution is the tip geometry itself. The sharper the tip, the better and more precise the recorded features will be. A broken and dull tip can also lead to a doubling of the image by interaction of two "tips" of one that is fragmented. The fine tuning of measurement parameters also plays a critical role for AFM, for example a high scanning frequency leads to a high tip velocity resulting in a broadening of measured features.

Apart from topological investigations there are SPM methods that target the electronic properties of a surface. One method of that category is Scanning-Kelvin-Probe-Force Microscopy, SKPFM is a specialized type of tapping mode where the tip is usually coated with e.g. platinum or a platinum-iridium alloy to make it conductive. With this and the necessary electric and electronic application (shown in figure 2.17) the difference between the potentials of surface and tip can be measured ( $V_{CPD}$ ) as shown in figure 2.16. With Tip and sample separated through a distance  $d$  there will be no electrical interaction and both Fermi levels  $E_F$  of the sample and tip (S and T respectively) will be aligned to the vacuum energy ( $E_V$ ) according to their respective work functions ( $\Phi_S$  and  $\Phi_T$ ). Bringing them closer together will lead to an alignment of Fermi levels through an electrical contact between them that leads to a formation of a contact potential difference ( $V_{CPD}$ ) between them. As shown later, this CPD is directly tied to the work function of the sample and by leveling out the CPD with an applied DC current it can be directly measured.

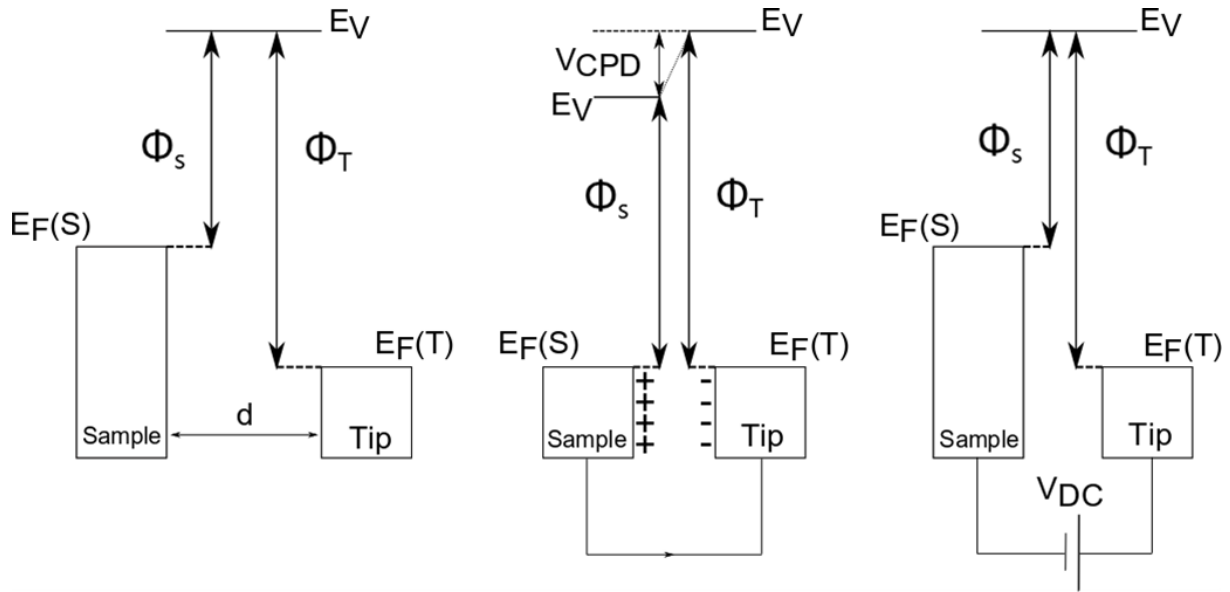


Figure 2.16: Representation of Fermi energies of Tip and Sample ( $E_F(T)$  and  $E_F(S)$ ) relative to the Vacuum energy ( $E_V$ ) and the corresponding work functions ( $\Phi_T$  and  $\Phi_S$ ). First sample and tip are separated by a distance  $d$  and have no electrical interaction (a). After bringing both into contact (b) both Fermi levels will align and equilibrate through a flow of current with a contact potential difference ( $V_{CPD}$ ) forming. c) applying a DC voltage to counter the CPD.

There are two main approaches (among others) like measuring the capacitance gradient<sup>75</sup> to measure the CPD of a sample. The first one is called Amplitude Modulated KPFM (AM-KPFM). This kind of technique is a dual pass measurement where with the first pass of the tip over the sample a standard Tapping-mode topography image is measured. The second pass however will be along the measured topographical profile with a pre-defined distance between sample and tip and without the tapping oscillation of the cantilever. Instead there will be a DC voltage applied to the cantilever that induces a vibration when there is a potential difference between tip and sample. The amplitude of this vibration will be sensitive to the potential difference and thus the CPD can be measured. Another approach to KPFM is called Frequency Modulated KPFM (FM-KPFM). Again this is a Tapping-Mode variation that, in contrast to AM-KPFM is a single pass technique, where in addition to the piezo-oscillation of the cantilever to detect the topography an AC signal is applied to the cantilever that induces an electrostatic force between tip and sample. According to Hooke's law this electrostatic force will influence the frequency of vibration.

In detail the shift in cantilever frequency  $\Delta f_0$  (at the AC frequency  $\omega_{ac}$ ) is proportional to the electrostatic force gradient  $\frac{\partial F_{\omega_{ac}}}{\partial z}$  that is, together with the applied AC and DC biases ( $V_{ac}$  and  $V_{dc}$ ) directly related to the contact potential difference ( $V_{CPD}$ ) as shown in equation 2.6.

$$\Delta f_0(\omega_{ac}) \propto \frac{\partial F_{\omega_{ac}}}{\partial z} = \frac{\partial^2 C}{\partial z^2} (V_{dc} - V_{CPD}) V_{ac} \sin(\omega_{ac} t) \quad (2.6)$$

The main difference between both methods is that AM-KPFM is more sensitive to potential changes whereas FM-KPFM comes with better spacial resolution.<sup>75</sup> Due to the nature of graphene having several topological features that can be of interest (or want to be avoided during CPD measurement) like wrinkles and bilayer patches, FM-KPFM proved advantageous in this work due to the good spacial resolution that allows rather precise identification of said features to exclude them for work function calculations. Figure 2.17 shows a general schematic of the technical realization of both AM- and FM-KPFM.

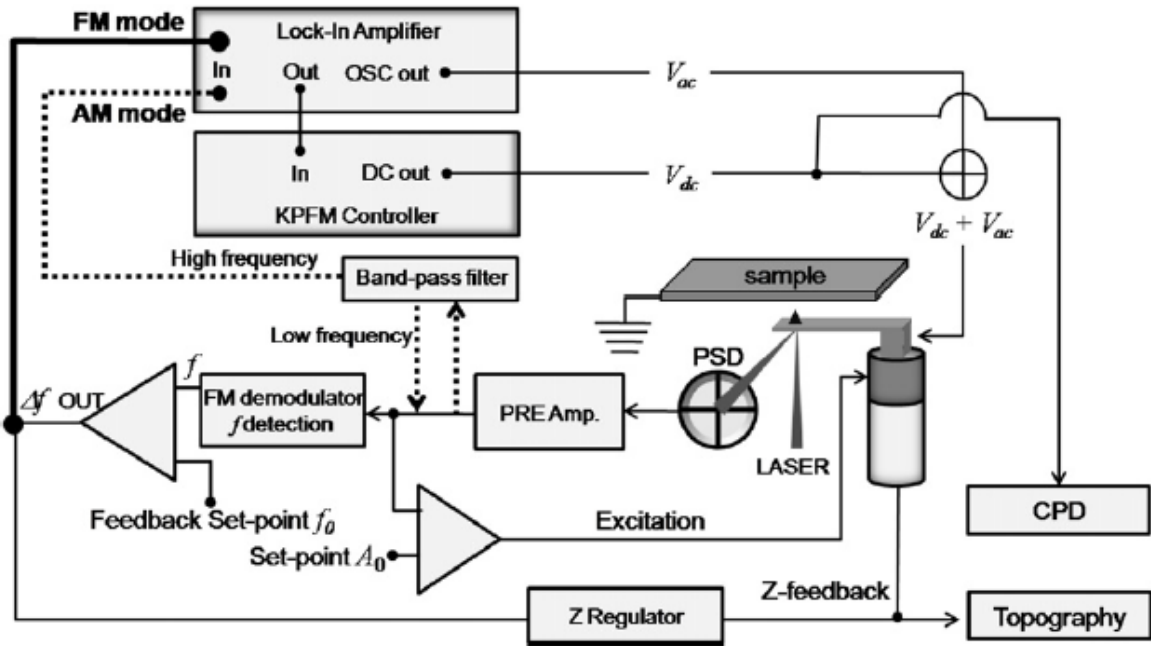


Figure 2.17: Overview over a standard KPFM setup. The normal AFM setup to measure topography is extended with a KPFM controller and Lock-in Amplifier to control the voltage applied to the tip to measure the CPD in either a frequency or amplitude modulated fashion (FM- and AM-modes). Adapted from Melitz *et al.*<sup>77</sup>

After measuring the contact potential difference it is possible to calculate the corresponding work function  $\Phi_S$  of the sample via equation 2.7. As it can be seen in eq. 2.7 besides the elementary charge  $e$  one has to know the work function  $\Phi_T$  of the tip. The tip work function can be obtained by measuring a surface with a known and stable work function like HOPG or Gold and calculation via the same eq. 2.7.

$$V_{CPD} = \frac{\Phi_S - \Phi_T}{-e} \quad (2.7)$$

However, in addition to electronic effects, the KPFM work function will also depend on the orientation-dependent interface dipole of deposited molecules. For example, it was demonstrated using hexaazatriphenylene-hexacarbonitrile deposited on graphene on quartz, that the work function of graphene can be varied from 4.5 eV to 5.7 eV by changing the surface orientation of the molecule from a planar to a vertically-inclined adsorption geometry, achieved through an increase the surface coverage.<sup>78</sup> Figure 2.18 depicts the relationship of the tip and sample work function to the density of states at the K-point of graphene, where the offset induced by surface adsorbed molecules  $W_0/m$  is shown.

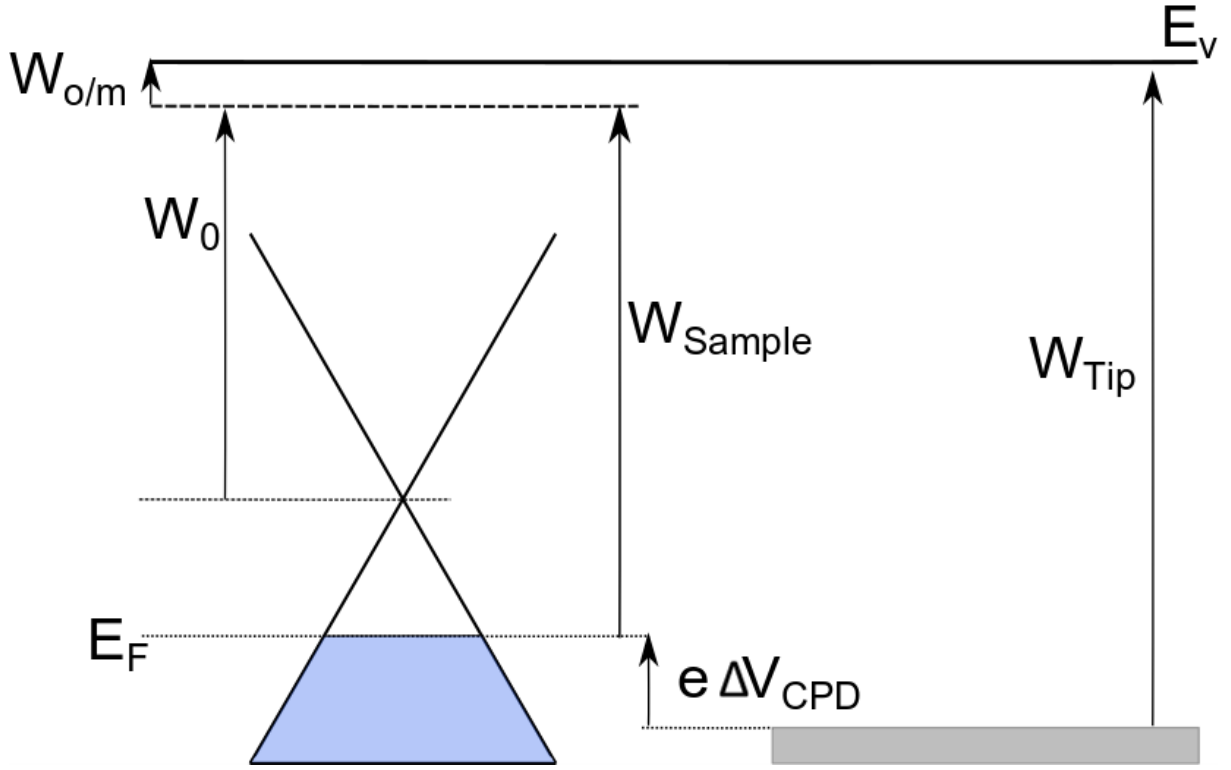


Figure 2.18: Relationship of tip work function ( $W_{Tip}$ ) and graphene work function ( $W_{Sample}$ ) relative to the Vacuum energy  $E_V$ .  $W_0$  describes the work function of completely neutral graphene but exposition of graphene to e.g. a substrate will change its Fermi energy  $E_F$ . The sample and tip work function are directly related over the measurable surface potential difference  $V_{CPD}$  and elemental charge  $e$  as shown in equation 2.7.  $W_{o/m}$  describes a possible offset of the work function with the presence of surface dipoles induced by adsorbates.

When integrating a material such as Graphene into device applications one has to consider its adhesion to different kinds of substrates and other materials that are involved in the device architecture like electrodes or solvents used for further deposition of additional materials. Without proper adhesion between all involved materials complex device structures can not reliably be realized. Thus knowledge of surface energies of modified graphene is key to reliably construct complex device architecture, due to adhesion being directly related to the surface energy<sup>79</sup> via the work of adhesion  $W_a$  as

$$W_a = \gamma_s + \gamma_l - \gamma_{sl} \quad (2.8)$$

with the liquid surface tension  $\gamma_l$  and the surface energy  $\gamma_s$ . However defining the term of surface energy is, especially for complex surfaces rather difficult and for the technological interest most times there will be no difference made between solid-surface tension (usually denoted as  $\gamma_s$ ) and the free Gibbs (of Helmholtz) energy of the surface (usually  $G^s$  or  $F^s$ ). Both are thus simply denoted as surface energy  $\gamma$ .<sup>79</sup> The surface energy of graphene is known for all kinds of configurations, like suspended, annealed, different substrates

and atmospheric conditions<sup>80,81</sup>, but non-covalently modifying the graphene surface will also lead to a change in surface energy that has to be considered, thus contact angle measurements have to be performed. One of the simplest approaches to access surface energies are contact angle measurements. In this type of measurement a droplet of liquid is deposited onto the surface that has to be investigated forming a liquid-solid interface. There are different kinds of model approaches available that are used to calculate surface energies out of contact angles<sup>79</sup>. The model used for this work is discussed later in section 3.4.

## 3 Non-Covalent Molecule/Graphene Heterostructures

### 3.1 Introduction

This work aims at a controlled non-covalent chemical doping of graphene. This type of doping is usually rather weak compared to other methods such as electrical doping<sup>39,74</sup> but has several advantages. Aromatic molecules can be easily deposited onto graphene without damaging the honeycomb lattice structure and due to the dopant being a small organic molecule, the engineering possibilities such as changing the donor/acceptor strength or adding secondary functionalities are numerous. To achieve non-covalent chemical doping the focus was set first on the molecule class of *N*-Heteropolycycles due to their broad variety of different structures and electronic properties that can be varied by either changing the substituents or variations of the core acene structure as discussed in section 2.1. Their  $\pi$ -systems additionally allow for a stronger interaction with graphene compared to aliphatic molecules which can be utilized for self-assembly and is crucial for reliable non-covalent functionalization.

To control the charge transfer interaction between molecules and graphene one has to understand the structure-property relationship. Thus, a broad palette of molecules is required in combination with a reliable deposition strategy. The more molecules are tested the better the overall understanding of the effects on graphene. This can potentially answer fundamental open questions such as: is the resulting shift in Fermi energy in graphene only related to the intrinsic electronic properties of the molecules? How strong is the influence of steric demanding substituents on the molecular packing and the charge transfer interaction? How does the deposition itself influence the overall graphene-molecule interaction? All those questions have to be addressed to form a overarching relationship of molecule structure and graphene modification, which can in turn be used to fine-tune properties in regard to the desired use of graphene in various possible applications (section 2). Access to a suitable set of molecules was granted through the Heidelberg collaborative research center "N-Heteropolyzyklen als Funktionsmaterialien" (DFG SFB1249). Within this interdisciplinary collaboration significant effort was dedicated to the synthesis polycyclic molecules for a variety of applications that can also be utilized for this project. In the end a conclusive evaluation of the most meaningful parameters influencing the doping of graphene will lead to knowledge of a structure-doping relation that will be useful to design suitable molecules effectively.

The molecular doping can readily be assessed through Raman spectroscopy in the case of graphene.<sup>82</sup> One additional fundamental parameter that will be affected through a modification of the intrinsic electronic structure is the work function which is of interest due to necessary alignment of work functions of e.g. electrodes and semiconductor in electronic devices to achieve optimal performances<sup>41,83</sup>. The work function will be ultimately affected by the Fermi energy shift, but to which degree? Will it follow the theoretical

correlation as depicted in section 2 or will the molecules themselves induce interactions that interfere, and if they do, to what extent can it be linked to the molecular structure and substituents? There are many examples in the literature on both the effects on the Fermi level and work function by molecular adsorption on graphene but mostly only with a small group of molecules and looking only at either DOS or work function changes.

When integrating graphene into applications knowledge of the electronic properties is key but there are additional properties that can be important to know. One of those parameters as mentioned in section 2 is the surface energy or adhesion. This often overlooked parameter will also be explored in this work on specific examples to test whether this parameter correlates to the structure of the deposited molecules.

The versatility of organic (aromatic) molecules can lead to opportunities beyond non-covalent dopants. Introducing secondary functionalities into the molecules can lead to a plethora of possible post-doping applications. As a proof of concept, two different concepts of post-deposition modifications are explored with ultra-violet oxidation and acid-treatment (i.e. protonation) of two *N*-Heteropolycycles subclasses.

To answer these questions, we developed a methodology that is based on a wet deposition process in ambient conditions. While it might appear more natural to perform such fundamental studies on ultraclean surfaces in ultrahigh vacuum conditions, we deliberately opted for the wet-chemical treatment for two reasons: Firstly, not all molecules can be evaporated, but readily deposited from solution. Secondly, we aimed to bridge the gap between the fundamentals of the molecular doping and real-world applications using widely available analysis tools. The main methods that were applied are confocal Raman spectroscopy to evaluate the changes in Fermi energy and ambient Kelvin-Probe-Force-Microscopy to investigate the influence on the work function of graphene. Furthermore commercially available graphene on Si/SiO<sub>2</sub> was used that comes with positive aspects, such as price and scale, but also negative aspects including transfer residues and pre-doping by the substrate. As already mentioned, this work is focused on the use of several different classes *N*-Heteropolycycles that are summarized in figure 3.1. The group of Tetraazapentacenes (TIPS-TAPs, figure 3.1 a) consists of five different molecules with increasing number of bromine substituents and a fourfold iodine substituted molecule. All TIPS-TAPs are equipped with solubility enhancing triisopropylsilyl-group that has a high steric influence that possibly hinders close packing of the molecule on graphene, but the effect is expected to be comparable in all derivatives, and thus does not influence the comparison of the molecules. The Tetraazaperopyrene (TAPPs, figure 3.1 b) species all have the same molecular D<sub>2h</sub> symmetry with more and less steric substituents as well as one molecule without the solubility enhancing perfluor-sidechains. For the Triangulenes (HTAs, figure 3.1 c) there were four different molecules available with varying substituents in a threefold D<sub>3h</sub> symmetry and a center nitrogen atom. A fifth HTA without substituents has a phosphorus atom instead of a nitrogen as center heteroatom.

It is to be expected that this PHTA will show overall different behavior compared to its nitrogen counterparts due to the fact that phosphorus is too large to be centered in the molecular plane making the structure bowl shaped compared to the planar NHTAs<sup>24</sup>. The last molecule family in testing were the Benzonaphthyridine (BNs, figure 3.1 d) derivatives with varying lengths of alkyl-sidechains.

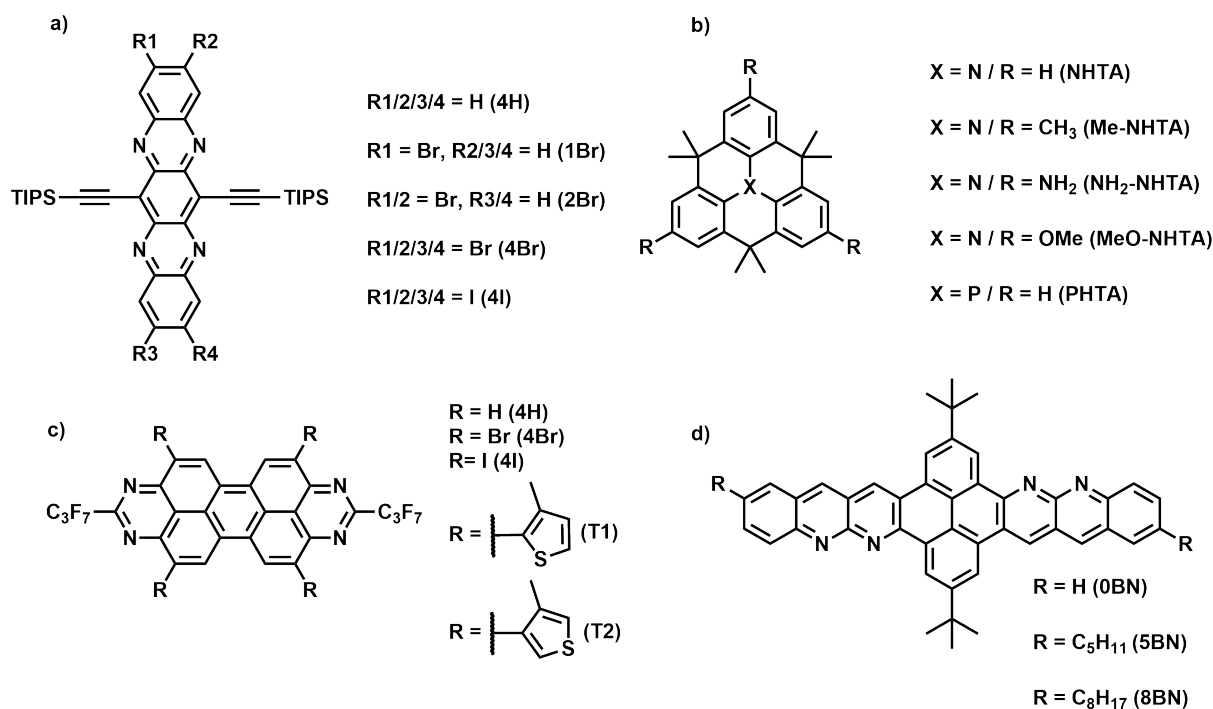


Figure 3.1: Summary of all *N*-Heteropolycycles used in this project: a) TIPS-Tetraazapentacenes with different substitutional patterns of bromine and iodine. TIPS-TAP-4H denotes only hydrogen substituents followed by one (TIPS-TAP-Br), two (TIPS-TAP-2Br) and four (TIPS-TAP-4Br) bromine substituents as well as four iodine substituents (TIPS-TAP-4I). b) Four different variations of *N*-Heterotriangulenes with either hydrogen (NHTA), methyl-groups (Me-NHTA), amino-groups (NH<sub>2</sub>-NHTA) or methoxy-groups (MeO-NHTA) as substituents. The fifth Heterotriangulene has hydrogen substituents and the center nitrogen atom is exchanged for a phosphorus atom (PHTA). c) Five different Tetraazaperopyrenes (TAPPs) with either four hydrogen (TAPP-H), bromine (TAPP-Br), or methylthiophen (TAPP-T1/T2) substituents. The fifth TAPP is called TAPP-n and is similar to TAPP-H but missing the perfluor sidechains. d) Benzonaphthyridines (BNs) with either pentyl- (5BN) or octyl-sidechains (8BN) or no alkyl-sidechains (0BN).

### 3.2 Sample Preparation and Deposition

Graphene being a zero-bandgap semiconductor<sup>52,84</sup> poses a problem when trying to identify doping effects. When graphene is exposed to standard atmospheric conditions there will be environmental effects altering the density of states of graphene such as for example adsorption of water molecules<sup>85-87</sup>. Additionally the substrate can have a doping-type effect<sup>88</sup> on graphene with Si/SiO<sub>2</sub> exerting p-type doping<sup>66</sup>. Preventing all those unwanted alterations of graphene would be possible by conducting all experiments with suspended graphene in a dry and inert-atmosphere or vacuum. This of course leads to an overall higher cost for all experiments due to the demand in specialized equipment and time. Again by keeping in mind that most applications of graphene in various devices and material hybrids employ ambient conditions<sup>7</sup>, the use of inert-conditions without substrate interactions is of less practical relevance. Thus it was necessary to design a protocol to allow for a comparison of all samples and measurements by reducing unwanted influences.

As a first cleaning step of the CVD-grown and wet-transferred graphene on Si/SiO<sub>2</sub> bought from Graphenea, the samples were annealed at 300 °C in an inert nitrogen atmosphere to remove the majority of adsorbed and more importantly intercalated (between graphene and substrate from the wet-transfer process) water that would lead to delamination of graphene during further processing. For all samples to be comparable to each other, one has to minimize environmental effects on graphene without intervening with the actual doping process of the molecules that is targeted. Thodkar *et al.*<sup>89</sup> developed a method to treat graphene with NMP to remove various adsorbates (e.g. water and polymer residues from the transfer processes) from the surface of Graphene by replacing them, resulting in a homogeneous NMP-coated graphene surface that was shown to result in consistent electrical properties over all samples studied. This treatment was done by submerging the annealed graphene samples in NMP at 70 °C over night with subsequent removal of any excess solvent with dry nitrogen

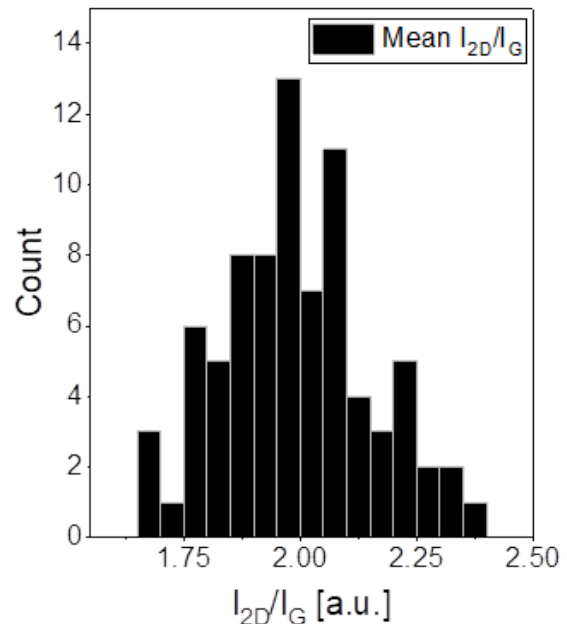


Figure 3.2: Histogram of mean 2D to G intensity ratio of N=79 samples with a mean value of 1.99 and a standard deviation of 0.15, showing the NMP treatment ensures a reproducible and reliable starting point for all Raman measurements.

gas. To confirm the reliability of this treatment, Raman spectra were taken after the NMP-treatment and analyzed before the molecules were deposited. The average Raman spectrum of a typical Raman map with 532 nm excitation is depicted in Fig3.3 and displays the characteristic Raman modes of graphene. To assess the sample homogeneity, the Raman 2D/G ratio was extracted from the individual spectra. Note that doping will impact the Raman spectrum in a number of ways (see chapter 2.2.3). However, the 2D/G changes most significantly in the regime of moderate doping that we expect from non-covalent functionalization. In addition, the intensity ratio can be readily extracted without data fitting making it the most feasible observable. A representative 2D/G histogram is displayed in figure 3.2 which shows, that the NMP-treatment indeed results in a fairly homogeneous sample with a well-defined Gaussian distribution of the 2D/G ratio centered around 2. Note that bilayer regions will yield a lower 2D/G ratio. However, since the distribution is fairly symmetric, the bilayer patches do not seem to have a significant effect on the average 2D/G ratio.. In addition to the electronic structure, one has to consider the defect density of the CVD-grown graphene before conducting the experiments. The representative Raman spectrum after NMP-treatment (figure 3.3) reveals that the overall defect density after preparation is rather low with an  $I_D/I_G$  ratio of about 0.03 which should not significantly affect the subsequent measurements.

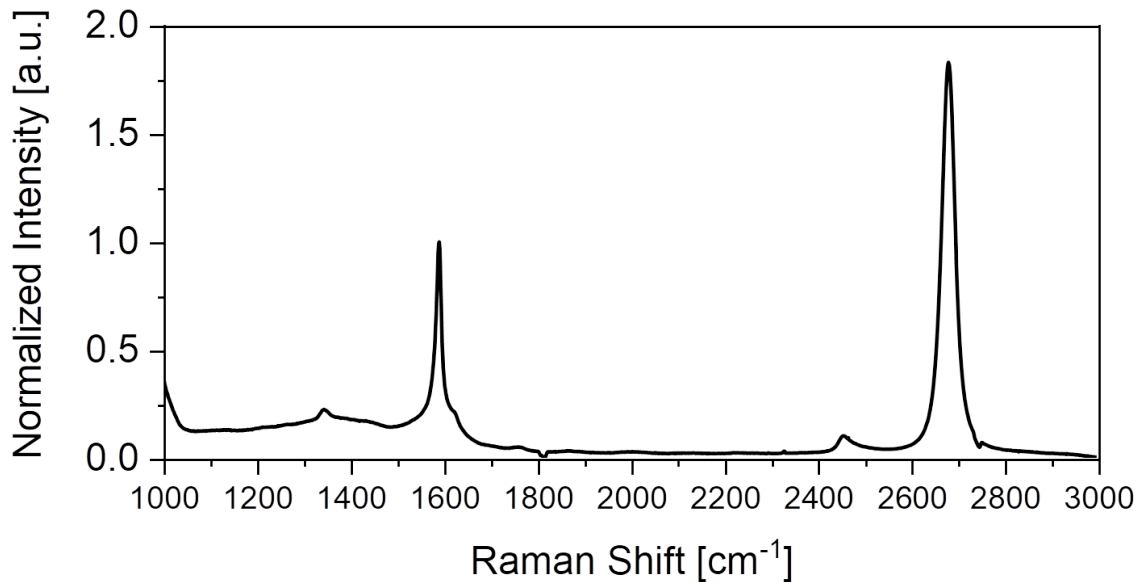


Figure 3.3: Mean Raman spectrum (excitation wavelength 532 nm) of  $\approx 300$  spectra taken over an area of two times  $65 \times 65 \mu\text{m}^2$  of a NMP-cleaned graphene sample, showing the typical graphene Raman bands around  $1585 \text{ cm}^{-1}$  (G-Band) and  $2680 \text{ cm}^{-1}$  (2D-Band). Only minor defects are visible with a very low intensity of both D- and D'-Band at  $1350 \text{ cm}^{-1}$  and  $1610 \text{ cm}^{-1}$  respectively, that should not interfere with following measurements.

To deposit the N-heteropolycyclic molecules onto graphene, the NMP-treated graphene samples were submerged in solutions (Toluene in most cases) of the molecules, with a concentration of  $10^{-4} \frac{\text{mol}}{\text{l}}$  for a desired time (depending on the experiment between 5 to 20 min). After this any excess solution was removed via dry nitrogen gas. The complete sample preparation process is illustrated in figure 3.4.

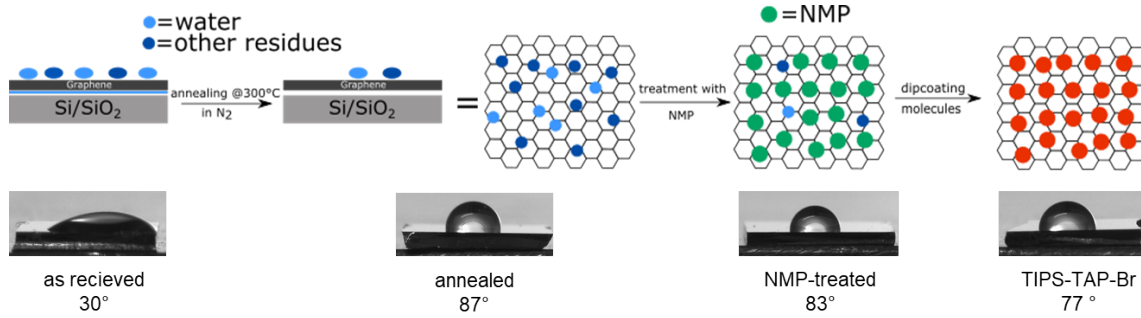


Figure 3.4: Sample preparation scheme; after initial annealing to remove intercalated water and residues the samples are treated with NMP for further cleaning and to achieve a homogeneous starting point to deposit the molecules onto graphene. Bottom row shows contact angle images with water demonstrating the increasing hydrophobicity after removing water and the changes of the surface due to different coatings.

The decision to primarily use toluene as a solvent for a dipcoating process was not only based on its ability to reliably dissolve all molecules equally, but also based on experiments done with TIPS-TAP-2Br to optimize the deposition parameters as described below.

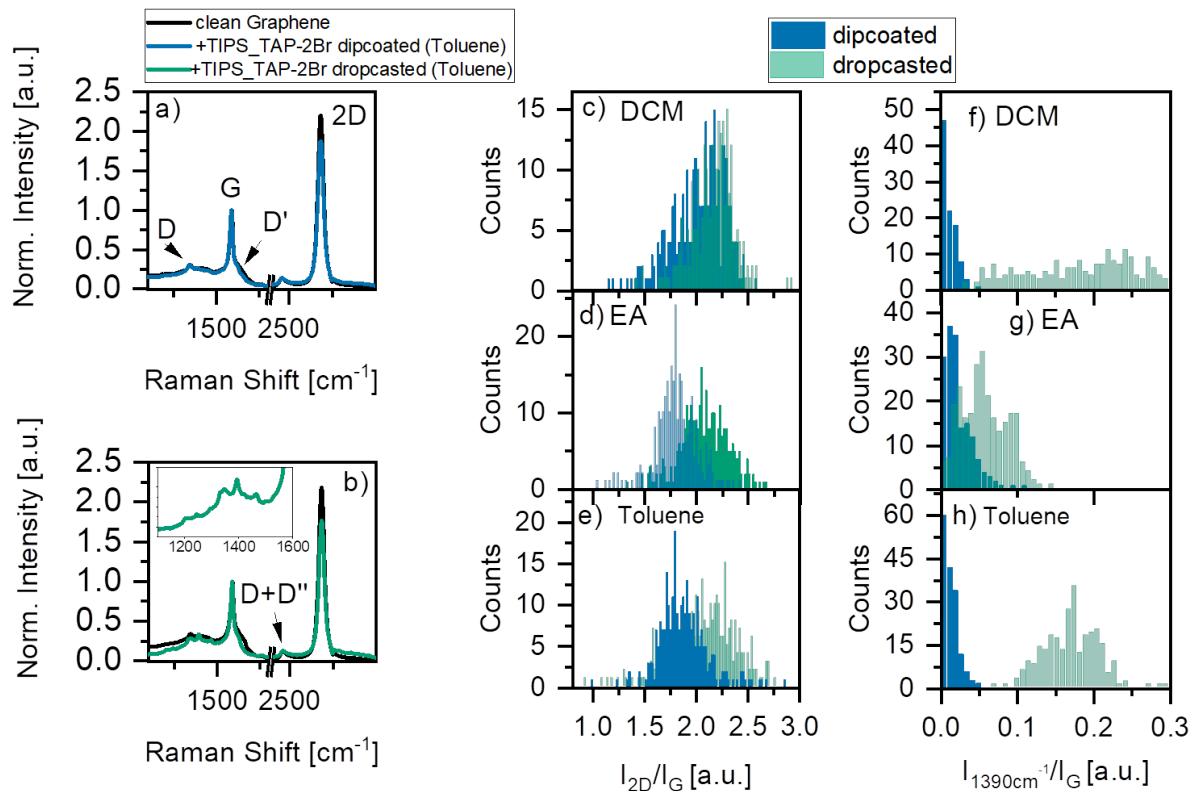


Figure 3.5: a)-b) average Raman spectra of TIPS-TAP-2Br deposited onto graphene (532 nm excitation) normalized to the G-Band compared to the same graphene sample area prior to deposition. The mean of 170 spectra over a  $65 \times 65 \mu\text{m}^2$  sample area is shown. Deposition by a) dip coating and b) drop casting. The inset in b) shows the Raman signature of the molecule. c)-e) Histograms of the intensity ratio of the graphene 2D and G band  $I_{2D}/I_G$  after deposition of the molecule by dip coating (black) and drop casting (blue) from different solvents. c) Dichloromethane, DCM, d) Ethylacetate, EA, e) Toluene. f)-g) Histograms of the intensity ratio of the highest molecule peak ( $\sim 1390 \text{ cm}^{-1}$ ) normalized to the graphene G-band. f) Dichloromethane, DCM, g) Ethylacetate, EA, h) Toluene.

TIPS-TAP-2Br was deposited by dip coating and drop casting, from three different solvents (Dichloromethane DCM, Ethylacetate EA, Toluene) with a concentration of  $5 \times 10^{-5} \frac{\text{mol}}{\text{l}}$ . Figure 3.5 a)-b) shows average Raman spectra normalized to the G-band (no baseline subtraction, 532 nm excitation) of the clean graphene reference in comparison to the spectra on the same sample area after deposition of TIPS-TAP-2Br by dip coating (figure 3.5 a) and drop casting (figure 3.5 b) from toluene, respectively. The typical graphene features<sup>62</sup> dominate the spectra in all cases: a G-band at  $\sim 1588 \text{ cm}^{-1}$  and a 2D-band at  $\sim 2685 \text{ cm}^{-1}$ . In both cases, the most dominant spectral change after deposition of the molecule is a drop in the 2D-band intensity relative to the G-band. In addition to the graphene signals, small features related to the molecule can be observed in the average spectra of drop-cast TIPS-TAP-2Br onto graphene (Figure 3.5 b, inset) with the most distinct one at  $1390 \text{ cm}^{-1}$ . The overall intensity of the molecule is rather low. On the one hand this might stem from a low coverage due to the low molecule concentration

used and the sterically demanding TIPS group. On the other hand, as later shown in figure 3.6, the molecules are electronically widely non-resonant at the excitation wavelength of 532 nm so that the Raman cross section is expected to be low. Nonetheless, we can use the Raman 2D/G intensity ratio ( $I_{2D}/I_G$ ) and the intensity of the molecule at 1390  $\text{cm}^{-1}$  relative to the G-band ( $I_{1390}/I_G$ ) as measure to evaluate both graphene doping ( $I_{2D}/I_G$ ) and surface coverage ( $I_{1390}/I_G$ ) with the molecule semi-quantitatively. A comparison of both intensity ratio distributions after dip coating and drop casting from the three different solvents is presented as histograms in figure 3.5 c)-h). As can be anticipated, more molecule is deposited by drop casting (blue) compared to dip coating (black), as seen from the  $I_{1390}/I_G$  ratio in figures 3.5 f)-h). Interestingly, the  $I_{2D}/I_G$  ratio seems to be widely unaffected by the amount of molecule with histograms peaking at similar  $I_{2D}/I_G$  as compared to the dip-coated samples. This might suggest that multiple stacks of molecules are formed by drop-casting, but that the molecules do not necessarily pack more densely on the graphene surface. Overall, drop casting results in a more inhomogeneous coating than dip coating which results in narrower distribution histograms. Therefore dip coating was used through the remainder of this study. Considering the solvent comparison, there is no significant variation, especially in  $I_{2D}/I_G$  ratios across the dip-coated samples. Distribution histograms are slightly narrower for toluene compared to DCM and EA, so that this solvent was chosen.

The resting time of the TIPS-TAP-2Br solution on the graphene substrate was also varied from 5 to 20 min. While some variations in the relative intensity of the molecule peaks were observed in as-deposited samples, the Raman spectra were virtually identical after rinsing the wafer with toluene to remove excess molecules. Thus, the washing step was included for subsequent work.

### 3.3 Deposition of Tetraazapentacene Derivatives (TIPS-TAPs)

To test whether the acceptor strength of the deposited molecules translates to the doping level of the graphene substrate, we have first chosen five derivatives of the tetraazapentacene family each with TIPS groups at the center of the core, but different halogenation patterns at the core edge (Figure 3.1). The synthesis of the derivatives is reported elsewhere.<sup>11,12,14,90,91</sup> The halogens at the core allow to tune the electronic structure systematically<sup>11,92</sup>. The LUMO level, which determines the acceptor strength, decreases in energy when introducing the halogen atoms. The halogenation also results in a change in the optical properties as illustrated by the absorbance spectra in Figure 3.6 (toluene,  $10^{-4}\text{M}$ ). The spectra show the expected characteristic structure of acene bands<sup>90</sup> between 500 nm and 700 nm. The overall number and distribution of peaks is similar for all TIPS-TAPs but the peak positions are subsequently red-shifted with increasing number of bromine substituents and increasing mass of the substituents (from -4Br to 4I) reflecting the change in oscillator strength.

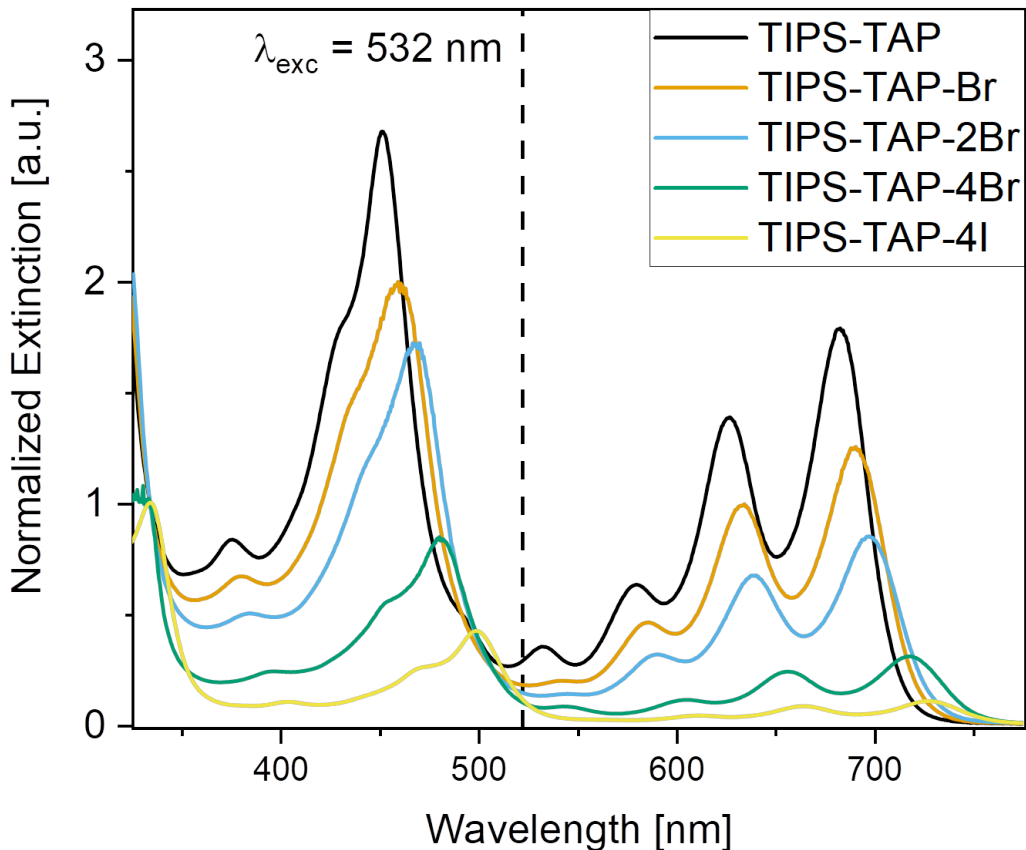


Figure 3.6: Normalized absorbance spectra of all TIPS-TAPs in toluene displaying the subsequent shift in absorbance by increasing number and mass of halogen substituents. All TIPS-TAPs show the typical acene absorption feature between 500 nm and 700 nm. The dashed line indicates the excitation wavelength of 532 nm used for Raman measurements.

The absorbance spectra also show that all TIPS-TAPs are not exactly and not equally resonantly excited by the Raman laser wavelength of 532 nm (dashed line) resulting in a difficult evaluation of coverage through molecular vibrations in the Raman spectra, as discussed further below.

The deposition of the molecules was carried out by dip-coating graphene as described in section 3.2 with the respective toluene solutions of the molecules. Unlike to the first evaluations, the concentration was increased to  $10^{-4} \frac{\text{mol}}{\text{l}}$  to ensure that the maximum coverage can be reached after a few minutes treatment.

Due to the NMP-treatment process before deposition of the molecules it was considered to use NMP itself as solvent for the TIPS-TAPs. However, concluding from the absorbance spectra in figure 3.7 which show a significantly different spectrum after 1 week attributed to decomposition due to the loss of most features, especially the acene bands, showing NMP is not a suitable solvent for this purpose.

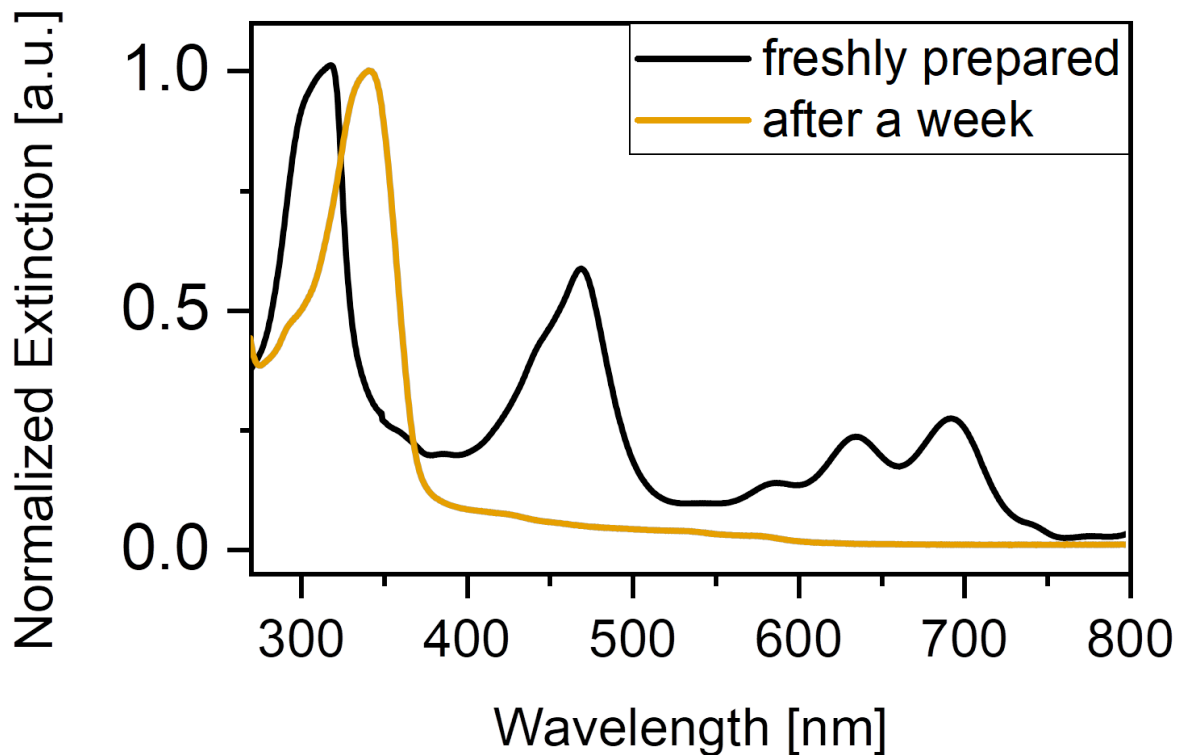


Figure 3.7: Absorbance spectra of TIPS-TAP-2Br freshly prepared in NMP (black) and after 7 days (yellow) demonstrating loss of most absorbance features attributed to decomposition.

As already mentioned in section 2.2.6 Raman spectroscopy is a powerful tool to investigate changes in electronic properties of graphene. Therefore Raman spectra were measured after deposition of the TIPS-TAPs to both identify shifts in Fermi energy and visualize molecular vibrations. Those spectra are shown in figure 3.8 with the characteristic graphene bands (G-band at  $1590\text{ cm}^{-1}$ , 2D-band at  $2690\text{ cm}^{-1}$ ) and also molecular vibrations with frequencies above the G-Band. The spectra displayed are mean spectra of two Raman-maps with an area of  $65 \times 65\ \mu\text{m}^2$  and 169 spectra each. All spectra are cleaned off bi- and multilayer spectra. Removing defective spectra was usually not necessary due to the careful selection of the measuring spots. Further details on the Raman measurements and evaluation can be found in section 8.

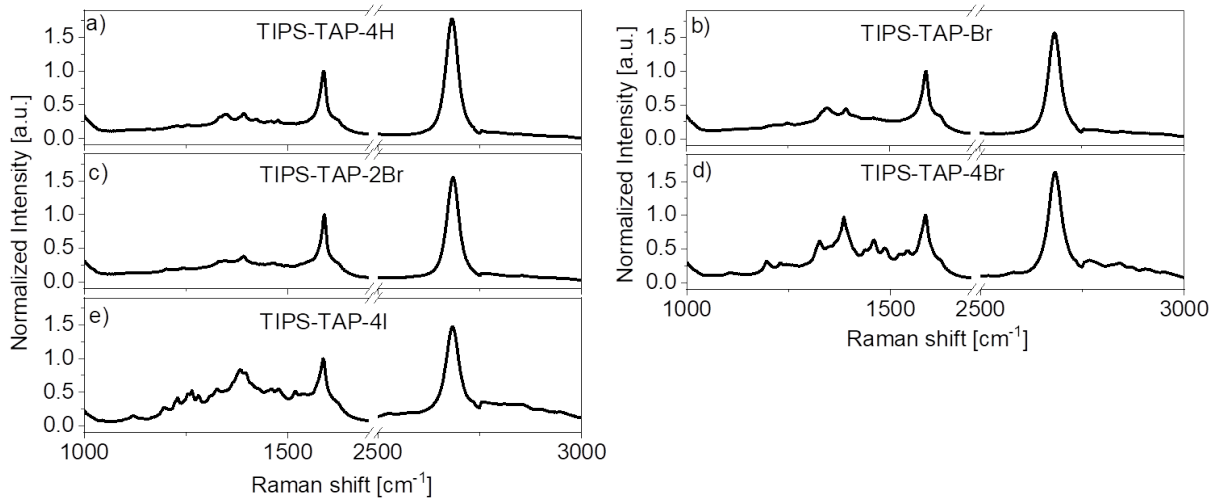


Figure 3.8: Mean and corrected Raman spectra for all TIPS-TAPs on graphene showing both graphene (G-band at  $1590\text{ cm}^{-1}$ , 2D-band at  $2690\text{ cm}^{-1}$ ) and molecule ( $1200\text{ cm}^{-1}$  to  $1600\text{ cm}^{-1}$ ) signals. No significant increase in defect density through processing can be observed due to low D'-band ( $1610\text{ cm}^{-1}$ ) intensity.

Prior to analyzing the modulation of the graphene electronic structure after deposition of the five different TIPS-TAP derivatives, the Raman modes of the molecules will be investigated as they might yield information on the molecular orientation relative to the surface. Raman signals from molecular vibrations were observed in the spectral region from  $1200\text{ cm}^{-1}$  to  $1600\text{ cm}^{-1}$ . This is confirmed by the calculated Raman spectrum of the unsubstituted TIPS-TAP derivative (see section 8) which is displayed in figure 3.9 f). The most intense vibration is observed at  $1330\text{ cm}^{-1}$ , with additional signals at  $\sim 1170\text{ cm}^{-1}$  and multiple peaks between  $1400\text{ cm}^{-1}$  and  $1650\text{ cm}^{-1}$ . It is thus important to verify, that these peaks do not significantly contribute to the intensity around the graphene G-band ( $1584\text{ cm}^{-1}$  to  $1588\text{ cm}^{-1}$ ), as this can potentially introduce an error in the analysis of the 2D/G ratio which will be discussed below. To test this, Raman measurements on dropcasted films of the molecules with a concentration of  $10^{-4}\ \frac{\text{mol}}{\text{l}}$  on an aluminum substrate were conducted. These are compared to the spectra of the molecules deposited on graphene

before and after washing with toluene for the five TIPS-TAP derivatives in figure 3.9 a)-e). No significant overlap of molecular vibrations with graphene are observed. In particular, the peak nearest to the G-band at  $1577\text{ cm}^{-1}$  is very weak and should not have an impact in the G-band intensity in particular in the spectra after rinsing with toluene where even the more intense molecular vibrations are hard to discern. In general, the experimentally observed and calculated Raman modes are in good agreement with each other. Some spectral shifts occur in the series of derivatives which we attribute to the different halogenation pattern on the acene core. Furthermore, in the measured spectra, more vibrations are discernible as in the calculated spectrum. This is because the calculations were performed on an individual, unsubstituted TIPS-TAP molecule without core halogenation and substrate interaction, respectively. For example, the mode at  $\sim 1230\text{ cm}^{-1}$  is the dominant vibration in TIPS-TAP-4Br and TIPS-TAP-4I, while it is absent in the calculated spectrum and the spectrum of TIPS-TAP-4H and significantly lower in intensity in TIPS-TAP-2Br and TIPS-TAP-1Br. We therefore attribute this peak to a vibration that involves the halogen atoms.

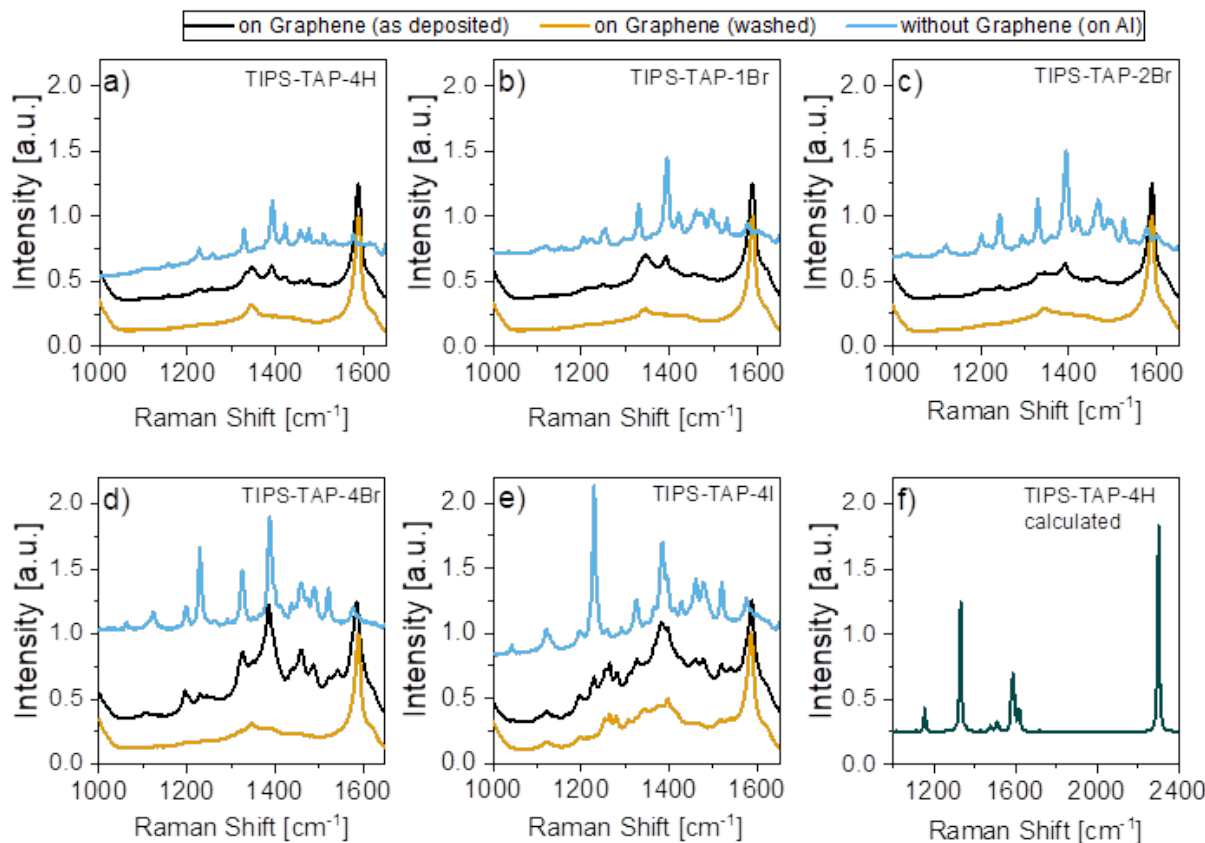


Figure 3.9: a) to e) Comparison of the molecule Raman bands on graphene as deposited (black), after washing (yellow) and without graphene (blue). The bare molecule spectra are baseline corrected to account for the large, unquenched fluorescence background. f) DFT calculated Raman spectrum of TIPS-TAP-4H.

When comparing the molecular Raman signature with and without graphene, some differences can be observed. For TIPS-TAP-4H, the reference spectrum looks similar to that on graphene whereas TIPS-TAP-1Br and -2Br show multiple signals between  $1100\text{ cm}^{-1}$  -  $1300\text{ cm}^{-1}$  as well as between  $1400\text{ cm}^{-1}$  -  $1550\text{ cm}^{-1}$  that are greatly reduced in intensity on graphene, relative to the molecular vibration at  $\sim 1390\text{ cm}^{-1}$  that remains clearly visible (at least before washing). For the TIPS-TAP-4Br all peaks with significant intensity remain visible on graphene except one peak at  $1579\text{ cm}^{-1}$  (corresponding to an acene core breathing mode), which seems to shift to lower wavenumbers. The most significant differences between pure molecule and molecule on graphene can be observed for TIPS-TAP-4Br and TIPS-TAP-4I. The high intensity feature at  $1229\text{ cm}^{-1}$  (which involves vibrations of the halogen atoms) is greatly reduced on graphene and new features can be observed around  $1265\text{ cm}^{-1}$ . Those differences can be attributed to the difference in molecular packing and stacking: In a dropcasted film on a substrate, we expect a random, disordered orientation of the molecules with no significant interactions with the substrate. In contrast, we anticipate a more ordered molecular orientation in the molecule film produced by dip coating graphene with strong substrate interactions. This leads to frustrated vibrations and different vibrational force constants that are reflected in changes of the Raman spectroscopic fingerprint (position and peak intensity ratios) of the molecule which provides (indirect) evidence for the self-assembly on graphene. Through the adsorption of an electronic acceptor various changes in the Raman spectra are expected. For example, the graphene  $I_{2D}/I_G$  Raman ratio is expected to decrease. The advantage of using the 2D/G ratio lies in the ability to determine the average ratio and distribution histograms without the necessity of data fitting. In addition, bilayer regions can be excluded by setting a cut-off based on the histogram shape. Typically, the distribution is Gaussian, but sometimes becomes asymmetric with a tail in the region of lower 2D/G ratios. For a relatively subtle modulation of the electronic structure of graphene as investigated here, it is thus beneficial to remove these spectra prior to calculating the average. In addition to the 2D/G ratio, it is expected that the G band shifts to lower wavenumbers and broadens with increasing doping level. To assess this, the G band region of the average spectra was fitted to 2-3 Lorentzians. In the spectra with insignificant intensity from molecule vibrations, 2 Lorentzians were used corresponding to the G and D' band. In some cases, for example TIPS-TAP-4Br), an additional Lorentzian was used to account for the molecular vibration. Note that bilayer regions are not excluded for this analysis method, as the fitting was applied to average spectra. The experimental Raman data from this study is shown in figure 3.10 where the changes in the Raman spectra of graphene are plotted as function of the LUMO level of the molecule. Within the set of molecules, a roughly linear scaling of the graphene  $I_{2D}/I_G$  Raman ratio, the G band position and the G band width with the DFT calculated LUMO levels can be observed. The positive slopes in the case of the 2D/G ratio and the FWHM of the G band, as well

as the negative slope in case of the G band position are consistent with the interaction of graphene with (weak) electron acceptors. On the one hand, this clearly demonstrates that the acceptor strength of the molecule indeed translates to the level of graphene doping. On the other hand, it suggests that the surface coverage with respect to the bottom layer of molecules in contact with graphene, is independent on the halogenation pattern and thus most likely directed by the TIPS group as anticipated.

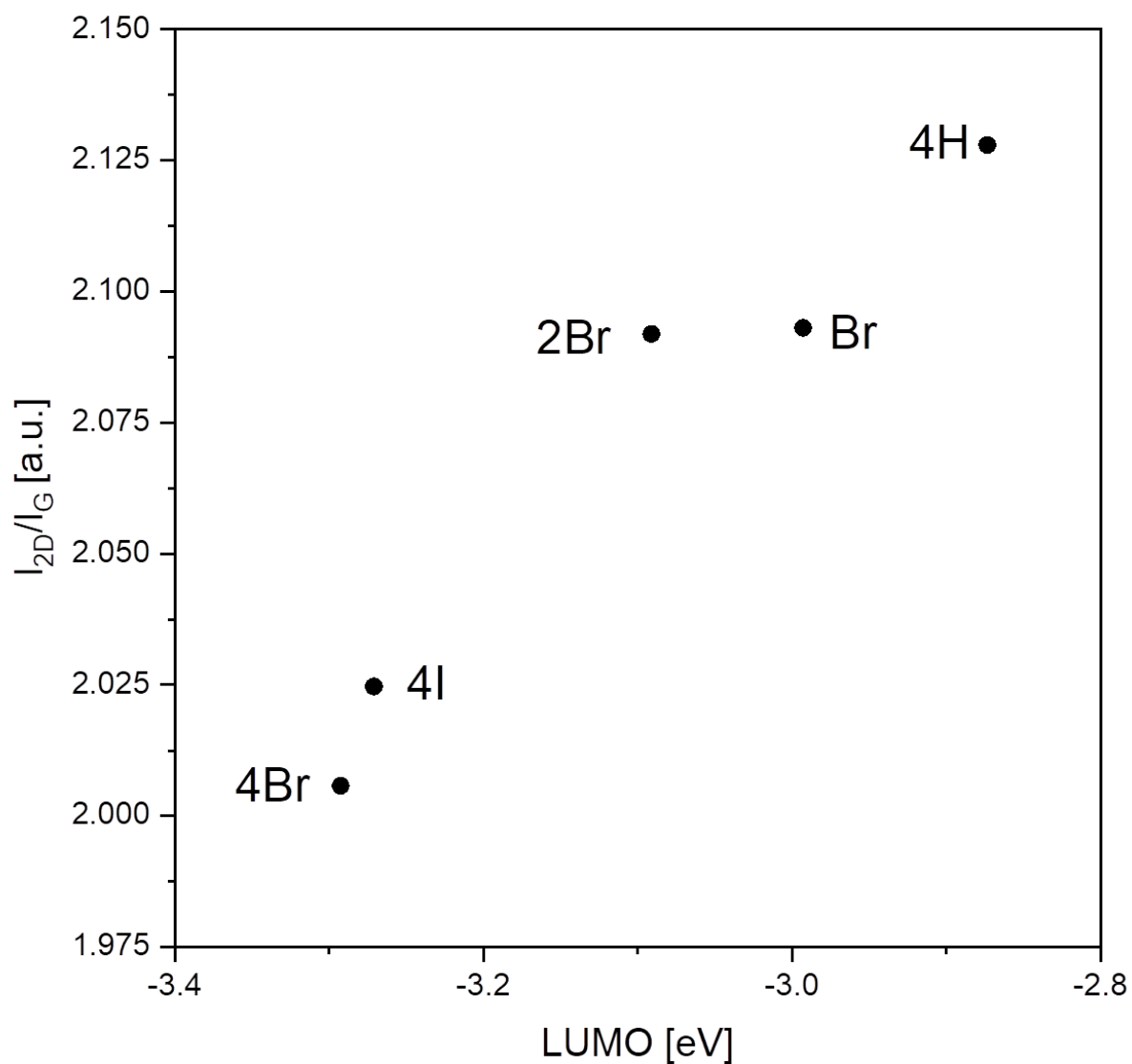


Figure 3.10: Raman intensity ratio in correlation with LUMO energies of the TIPS-TAP molecules showing an almost linear dependency between induced charge transfer and acceptor strength, that is in accordance to theory.

Doping of graphene should also result in a modification of the work function (WF) which can be measured through Kelvin probe force microscopy (KPFM). However, one has to keep in mind that dipole-moments introduced with adsorbed molecules will additionally influence the work function (as mentioned in section 2). As such, a comparison of the scaling of the work function across a set of molecules can potentially offer complementary results to the analysis based on the Raman spectra and give additional insights in both doping and surface orientation. To test this, KPFM measurements were performed on graphene dip-coated in solutions of the five different TIPS-TAP derivatives. Since the measurements were performed in ambient conditions, absolute values of the work function will be affected by humidity and other environmental influences. Nonetheless, a comparison across the samples is accessible when measured under the same conditions. Figure 3.11 shows representative KPFM topography (top row) and contact potential difference (CPD, bottom row) images of a set of samples including TIPS-TAP-4H (left) and TIPS-TAP-1Br (right). Both examples show a well defined graphene topology resolving wrinkles and bilayer patches as well as some sharply resolved defects. The corresponding CPD images are similarly well resolved; wrinkles and bilayers are nicely defined having a higher CPD as monolayer graphene<sup>93</sup>. Those two examples clearly demonstrate the advantage of using the frequency modulation (FM) instead of an amplitude modulation (AM) as the higher spacial resolution helps separating monolayer graphene from defects and multilayers.

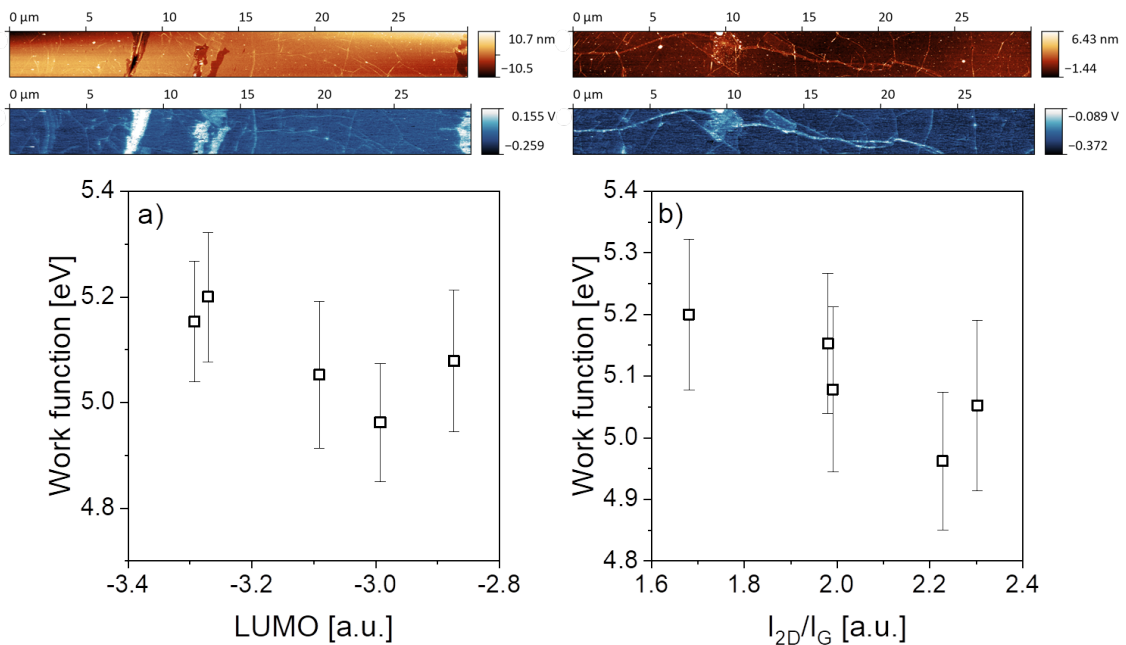


Figure 3.11: Top row: Examples of topography (orange) and contact potential difference (blue) scans. Bottom row: correlation of measured work function to LUMO energy (a) and Raman intensity ratio (b) of washed TIPS-TAP samples, showing the expected trends of a increasing work function with stronger acceptor interactions represented by LUMO energy and Raman 2D/G intensities.

Calculating the work function of the samples was done as elaborated in section 2.2.6 and the technical details of the measurement procedure are described in section 8. Three measurements per sample on different areas were performed and averaged. The work function varies weakly across the samples with values ranging from 4.9-5.2 eV which is consistent with weakly doped graphene measured in ambient conditions.<sup>94</sup> The resulting data is shown in figure 3.11 as function of the DFT-calculated LUMO energy of the molecules (a) and measured Raman intensity ratio (b). The work function of graphene is in first approximation directly related to the Fermi level of graphene that will change if graphene is in contact with donor or acceptor molecules. In the case of the TIPS-TAP derivatives which we classified as acceptor molecules, the work function should increase with decreasing LUMO energies. A similar trend should be observed for the correlation with the Raman intensity ratios for the reason that this parameter is tied to the Fermi level shift as well. While figure 3.11 roughly reproduces this trend, there is significant scatter in the data. A number of reasons can be identified: i) the overall difference across the sample is small. This is likely linked to the electronic nature of the molecules which are weaker acceptors than for example perylene bisimides<sup>95</sup> or the previously mentioned hexaazatriphenylene-hexacarbonitrile<sup>78</sup>. ii) Additional effects on the work function may arise from the molecular orientation. iii) Measurements were conducted in ambient conditions. Therefore, the absolute values will be depended on the overall environment including humidity to some extent. In spite of this, overall, the KPFM measurements confirm the results from the Raman analysis and suggest that graphene doping is defined by the acceptor strength of the molecule with negligible impact from the packing density.

### 3.4 Deposition of Tetraazaperopyrenes

After having established a suitable protocol to coat graphene and precisely evaluate the resulting changes in its electronic and surface properties, another set of molecules was investigated to further expand the trends seen for the TIPS-TAP family. Therefore Tetraazaperopyrenes (TAPPs) with different substituents, but same molecule symmetry were investigated. The structures of the derivatives together with their calculated HOMO and LUMO levels are depicted in Figure 2.2. While the HOMO is widely constant over the series of molecules, the LUMO varies significantly depending on the substitution pattern. Some of the derivatives (TAPP-Br, TAPP-I and TAPP-H) are stronger acceptors than the TIPS-TAP molecules under study in section 3.3. The absorbance spectra are shown in figure 3.12 and display a similar albeit shifted absorption profile for all molecules with the typical peropyrene-features visible between 400 nm and 500 nm<sup>96</sup>. The most striking difference across the samples is a broadening of all spectral features for both thiophene substituted TAPPs (-T1, -T2) compared to the unsubstituted or halogen substituted TAPPs. Furthermore, the thiophene-substituted derivatives are in resonance with the excitation wavelength of the Raman measurements which is expected to result in an enhanced intensity of their Raman vibrational modes.

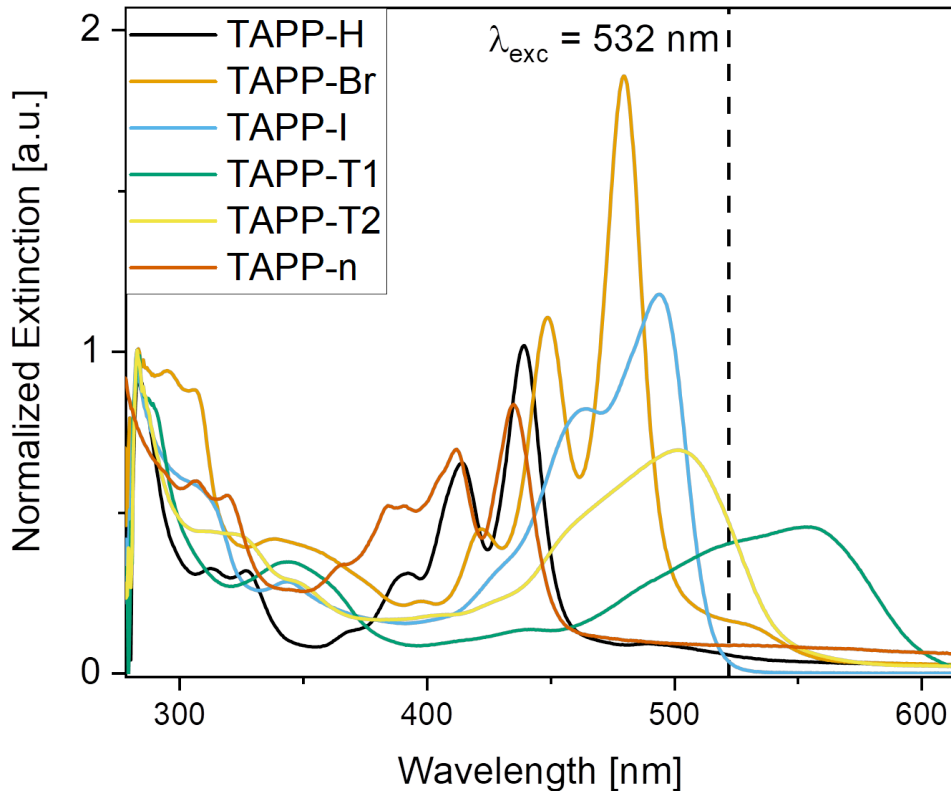


Figure 3.12: Normalized absorbance spectra of all TAPP molecules with the Raman excitation at 532 nm indicated with a dashed line. All spectra show a similar structure with typical peropyrene-core bands from 400 nm to 550 nm although for thiophene substituted molecules these bands are rather broad in comparison.

The solvent of choice for absorbance spectra and deposition on graphene was toluene for the TAPPs except for TAPP-n which is not equipped with the solubility enhancing perfluor sidechains<sup>17</sup>. For this molecule NMP was used as a solvent for processing due to the extremely poor solubility of TAPP-n in most common organic solvents. To allow for a comparison across all molecules, it was important to test whether it is possible to use NMP as processing solvent for the other TAPPs as well. To this end, absorbance spectra in NMP were taken for the remaining TAPPs that are shown with three examples in figure 3.13. For TAPP-H (figure 3.13, a)) the changes are not significant on the first glance, but after 6 days absorbance features around 450 nm have vanished completely. TAPP-H (figure 3.13, b)) shows an overall decrease in intensity, whereas TAPP-T1 (figure 3.13, c)) seems to decompose to a certain degree due to a significant loss in absorbance features. This demonstrates again - similar to the TIPS-TAPs - that NMP has to be used with caution in combination with complex organic molecules due to unpredictable changes in molecular compositions that could later lead to untraceable effects in conjunction with the deposition onto graphene. As already mentioned TAPP-n could only be deposited from a NMP solution. In order to obtain a meaningful comparison of all other TAPPs in NMP, the deposition from NMP was always carried out with fresh solutions that were monitored via absorbance spectroscopy prior to any deposition procedure to prevent the introduction of experimental errors.

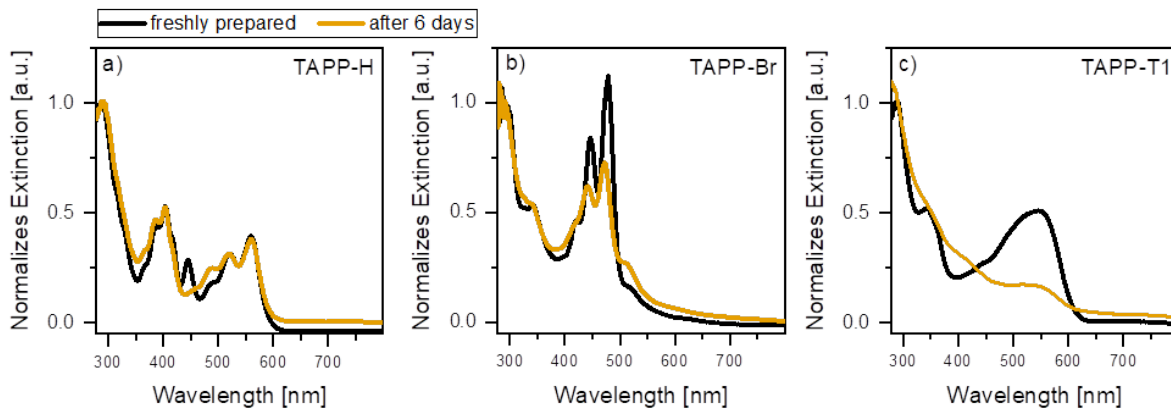


Figure 3.13: Normalized absorbance spectra of a) TAPP-H, b) TAPP-Br and c) TAPP-T1 in NMP both freshly prepared (black) as well as after 6 days (yellow). All spectra show changes occurring after 6 days. These are only minor for TAPP-H, but significant for TAPP-T1 which seems to undergo some kind of degradation.

The deposition process was carried out in analogy to the TIPS-TAP molecules with concentrations of  $10^{-4} \frac{\text{mol}}{\text{l}}$  for both Toluene and NMP solutions and dipcoating times of 10 minutes. Raman spectra were recorded with the established settings of 300 spectra over two spots on each sample. The bi- and multilayer corrected mean spectra are shown in figure 3.14. In all spectra, molecule vibrations can be observed below  $1500 \text{ cm}^{-1}$ . In addition TAPP-H, -T2 and -n show a molecule vibration rather close to the G-Band

of graphene (around  $1580\text{ cm}^{-1}$ ). Interestingly, the Raman signature of the molecule is less pronounced for the thiophene substituted derivatives in spite of anticipated resonance conditions based on the absorbance spectra in solution. The 2D-Band (around  $2680\text{ cm}^{-1}$ ) exhibits a much lower relative intensity compared to the reference sample (or all TIPS-TAP coated graphene samples), which is most obvious for TAPP-I where it is below 0.25. This would suggest a rather high shift in Fermi energy presuming that this 2D/G intensity ratio is a the result of only the electronic interaction between molecule and graphene. However, a comparison to the spectra of e.g. TAPP-I and TAPP-H reveals that the molecule vibration close to the G-band, visible for TAPP-H seems to be absent for TAPP-I. Considering that vibrations will shift with the introduction of heavier substituents (hydrogen compared to iodine) it might be possible that this vibration is shifted far enough to lower wavenumbers to overlap with the G-band giving rise to an overestimated apparent G-band intensity due to an overlap with molecular vibrations. This had to be taken into account prior to the extraction of intensity ratios.

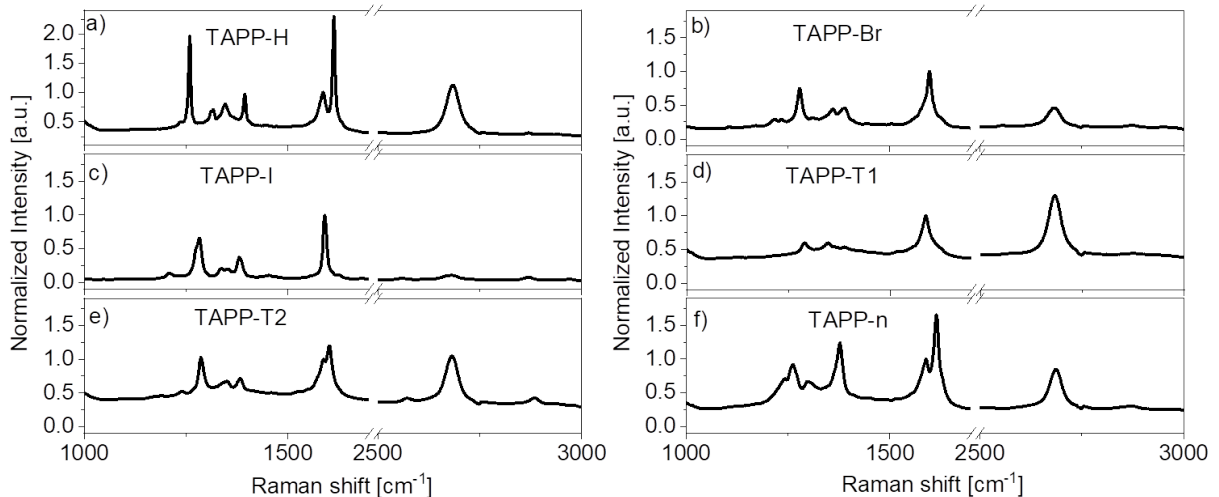


Figure 3.14: Mean and corrected Raman spectra for all TAPPs (532 nm excitation; dip-coated from toluene) on graphene showing both graphene (G-band at  $1590\text{ cm}^{-1}$ , 2D-band at  $2690\text{ cm}^{-1}$ ) and molecule ( $1200\text{ cm}^{-1}$  to  $1600\text{ cm}^{-1}$ ) signals.

To verify the overlap of molecular vibrations with the graphene G-band, Raman spectra of the pure molecule, dropcasted on aluminum substrates were recorded and are overlaid with the graphene Raman spectra in figure 3.15. Overall the molecule vibrations observed on graphene are in good agreement with the signals recorded without graphene, although there are shifts in their frequencies do to the different environments. Dropcasted films of the molecules likely consist of polycrystalline and amorphous, disordered components, whereas on graphene there are no comparable molecular ensembles and additionally frustrated vibrations due to the substrate interaction. Nonetheless this comparison makes clear why the observed graphene intensity ratios seem to be out of proportion. For e.g. TAPP-H the molecular vibration around  $1600\text{ cm}^{-1}$  is still separated to the G-band,

whereas for TAPP-Br, -I and -T1 it is shifted low enough to directly overlap with the graphene signal introducing an error to the apparent 2D/G intensity ratio.

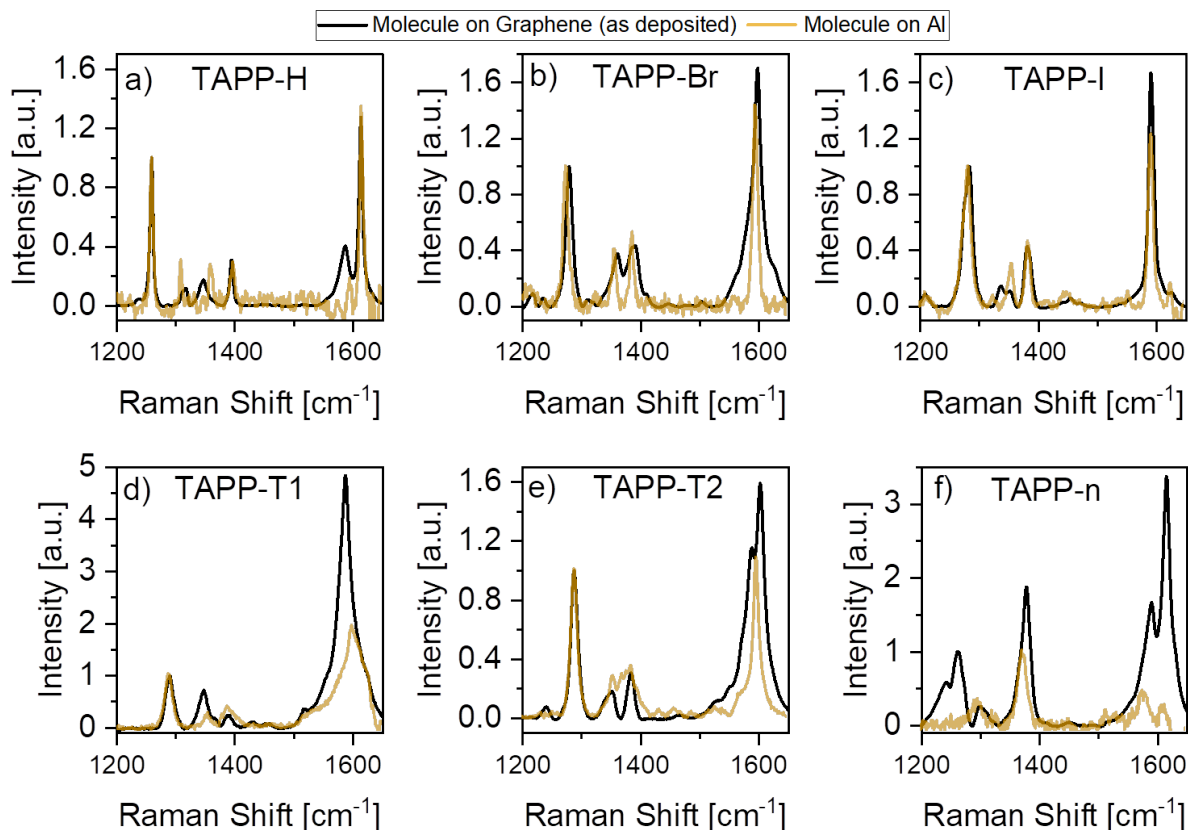


Figure 3.15: Comparison of the molecule Raman bands on graphene (black) and without graphene (yellow). The bare molecule spectra (532 nm excitation, dropcasted from toluene) are baseline corrected to account for the large, unquenched fluorescence background.

To gain access to the true G-band intensity all spectra in the G-band region were fitted to 3-4 Lorentzians using the information on the molecule peak intensity relations and positions extracted from the pure molecule spectra to set reasonable boundary conditions as constraints for the fit. Examples for the fitting results are shown in figure 3.16. To assess the viability of the fitting, the position and 2D/G intensity ratio are plotted against each other in figure 3.16e. In doped graphene, these two quantities should scale with each other, as is the case. With the fitting procedure being confirmed, it is also possible to compare the relative intensities of the molecular vibrations for both NMP and toluene processed samples which are displayed as bar graphs in figure 3.16f-g from samples measured directly after deposition and after washing. Overall the relative intensity of the molecule variations varies significantly with solvent and molecule structure. On the one hand, this might suggest different packing densities. However, on the other hand, the different resonance conditions (figure 3.12) will have an impact on the relative intensity of the molecular vibrations across the different molecules. However, as already mentioned

above, the thiophene-substituted TAPP are expected to be resonant, but show a low relative intensity of the vibrations strongly suggesting that the packing density in these cases is much lower than for the other derivatives. Regarding the difference between washed and as-deposited samples, there is no significant difference in relative molecule intensity for toluene as solvent. Samples dip-coated from NMP do show a significant decrease in molecule after washing with toluene suggesting a weaker interaction of the molecule with graphene, which can stem from residual NMP trapped between the molecule and graphene surface.

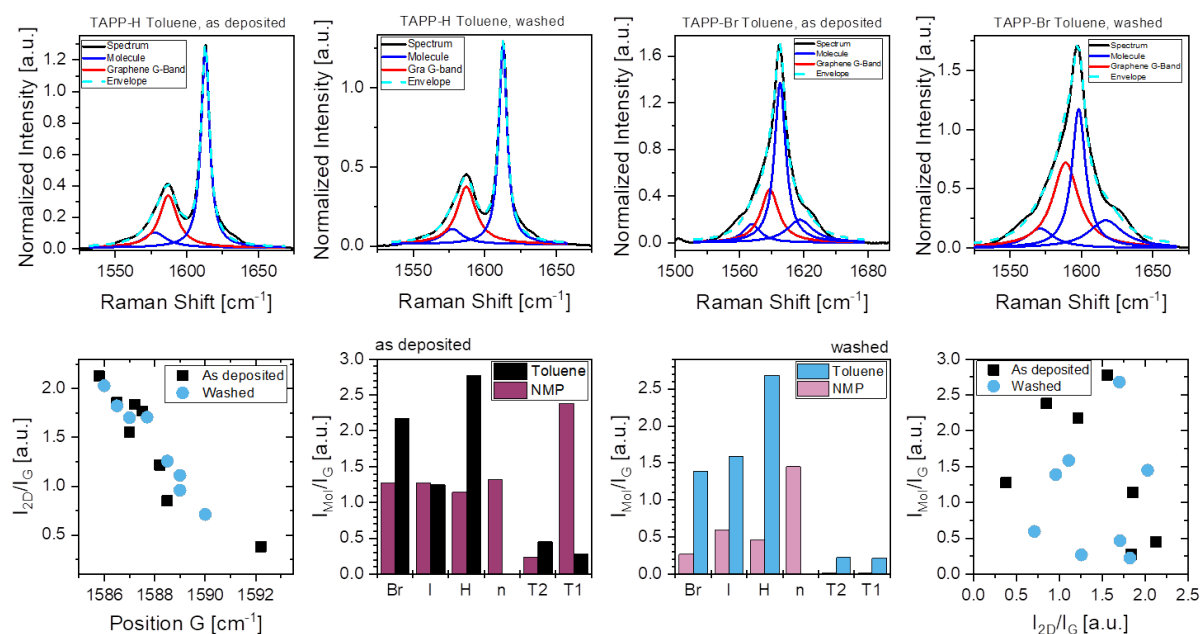


Figure 3.16: Summary of Raman spectroscopic results for all TAPPs. The top row shows examples how the different spectra were fitted to separate the molecule signal from the graphene G-Band. The bottom row shows from left to right the correlation of Raman intensity to the position of the G-band, the molecule Raman intensity for both NMP and toluene before and after washing as well as a plot of the relative intensity of the molecule vibration to the graphene Raman 2D/G ratio.

In spite of the semi-quantitative nature of the relative molecule intensity as measure for packing density, it is striking that a plot of relative intensity of the molecular vibration at around 1620  $\text{cm}^{-1}$  as function of the graphene 2D/G ratio in figure 3.16h clearly shows the absence of a correlation. This might suggest that the level of graphene doping is indeed independent on the packing density. If this was the case, a scaling of the graphene Raman 2D/G ratio with the acceptor strength of the molecules is expected. Figure 3.17 shows that this is indeed the case, as the Raman 2D/G intensity scales with the LUMO of the molecule.

In Fig. 3.17, the data obtained from TIPS-TAP is included for comparison. Strikingly, the data falls on the same curve. This strongly confirms the conclusion from the previous chapter that molecular doping of graphene is a function of the donor/acceptor strength of the molecule, irrespective of packing density.

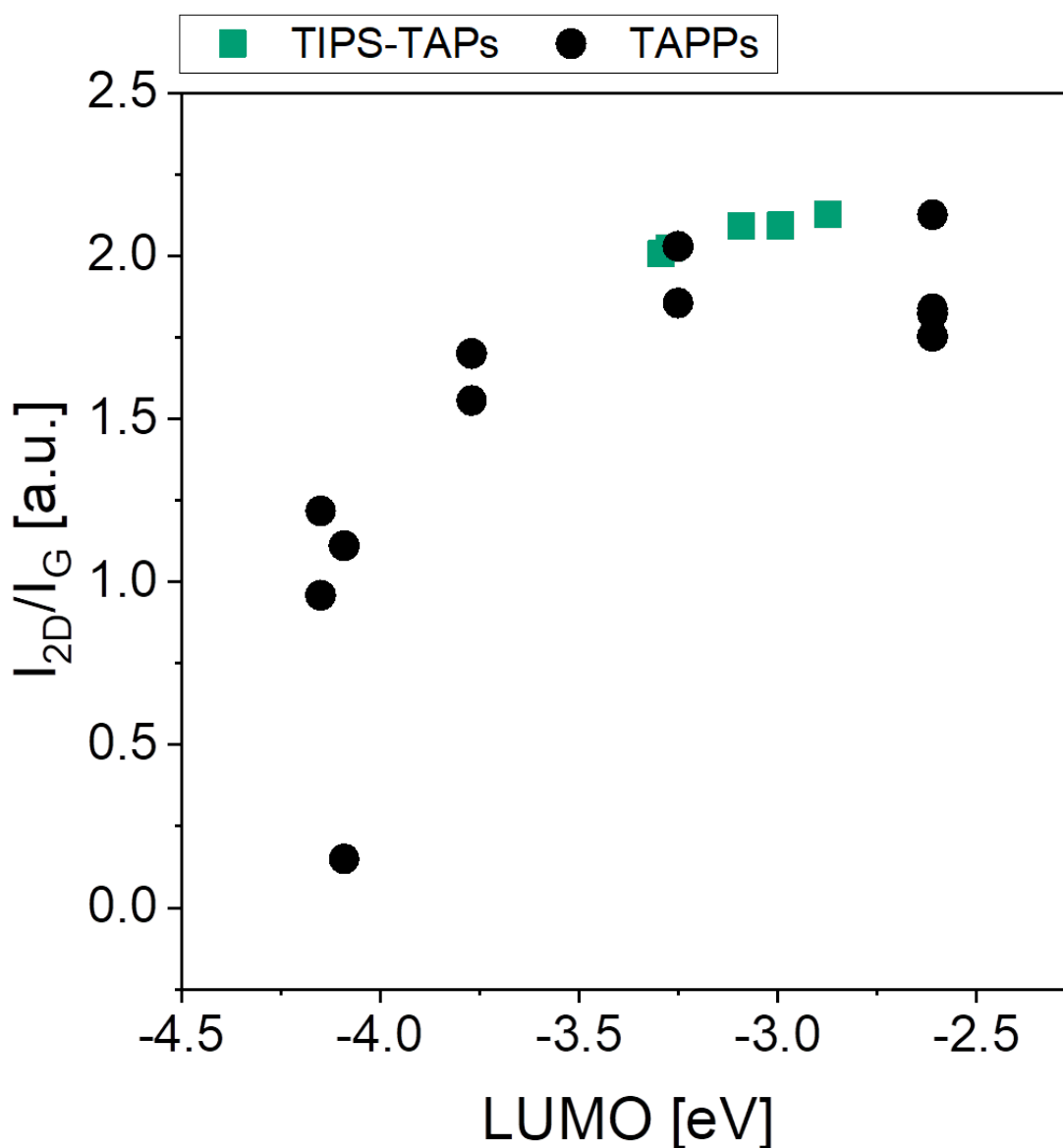


Figure 3.17: Correlation of the graphene Raman 2D/G intensity ratio as function of LUMO energy of the acceptor molecules. The scaling with the TAPP molecules is independent on whether access molecule was removed by washing (a). In addition, panel (b) shows that data from TIPS-TAPs (green) and TAPPs (black) fall on the same curve which is in fact not linear, but shows a sharp decrease in graphene 2D/G ratio for lower LUMO energies.

To further investigate the influence on graphene by interaction with the TAPP-derivatives work function measurements were conducted according to the established protocol. Only the washed samples are considered for comparison due to the significant influence of

surface dipoles that are dependent on molecular orientation that will change with larger amounts of molecule deposited<sup>78</sup>. Overall, the previously observed trend where low LUMO energies correlate to a higher work function (figure 3.18, a) is widely retained. Still there is a rather large scatter in the data, presumably due to the influence of the surface. This is nicely demonstrated by the difference in work function observed between both thiophene substituted TAPPs, that have the same LUMO energy of -2.61 eV, but result in different work functions when deposited on graphene. This can most likely be attributed to the orientation of the thiophene substituents being rotated out of plane for TAPP-T1<sup>19</sup> changing the packing behavior and introducing surface dipoles-effects that are manifested in an increase in the measured work function. Similarly, as seen with the TIPS-TAP derivatives, the work function scales reasonably with the graphene Raman I<sub>2D</sub>/I<sub>G</sub> ratio (figure \*b) since both quantities reflect the graphene doping. Although again there is a little more scatter observed for the spread of work functions for the TAPPs likely due to the different natures of substituents.

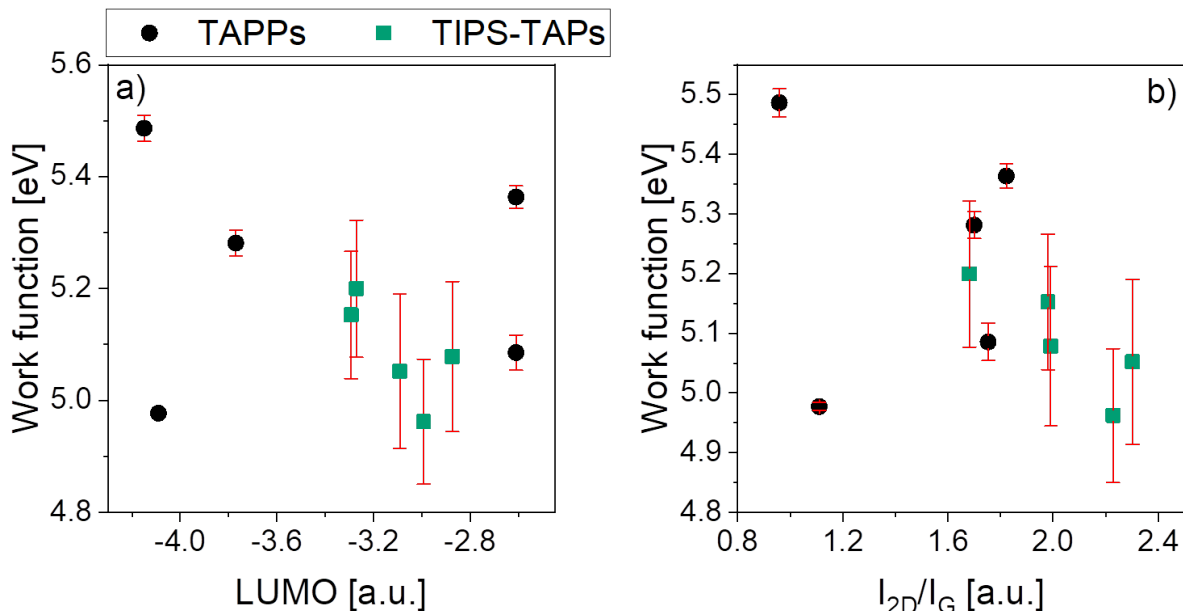


Figure 3.18: Correlation of work function to both LUMO energy of the molecules (a) and Raman intensity ratio (b) showing previous trends demonstrated with TIPS-TAPs continue with TAPPs as a different acceptor molecule family.

As mentioned in section 2, in addition to the modulation of the electronic properties of graphene, knowledge about surface energies can also be beneficial in later device integration. Naturally, deposition of organic molecules on any surface will change its surface energy. However, it is uncertain to which extent the surface energy of graphene is altered through non-covalent functionalization. To investigate this contact angle measurements were conducted, due to deposition of the TAPP derivatives on graphene seemed to result in a relatively robust coating, as the coverage of the TAPP derivatives on graphene showed no significant decrease in relative intensity of the molecular vibrations were ob-

served after washing with toluene, suggesting that those molecules have a rather high bonding strength to graphene. In combination with rather polar solvents used for contact angle measurements this ensures no significant loss of molecules between subsequent contact angle images. It should be noted that this was not the case of the TIPS-TAP molecules. Figure 3.19 shows an example set of optical images of droplets of five different solvents deposited on the TAPP-graphene surface which were used to measure the contact angles. The chosen solvents were water (surface tension,  $\gamma_l = 71.97$  mN/m), glycerin ( $\gamma_l = 63.06$  mN/m), dimethylsulfoxide (DMSO,  $\gamma_l = 43.54$  mN/m), acetonitrile (MeCN,  $\gamma_l = 29.29$  mN/m) and isopropanol ( $\gamma_l = 21.7$  mN/m).

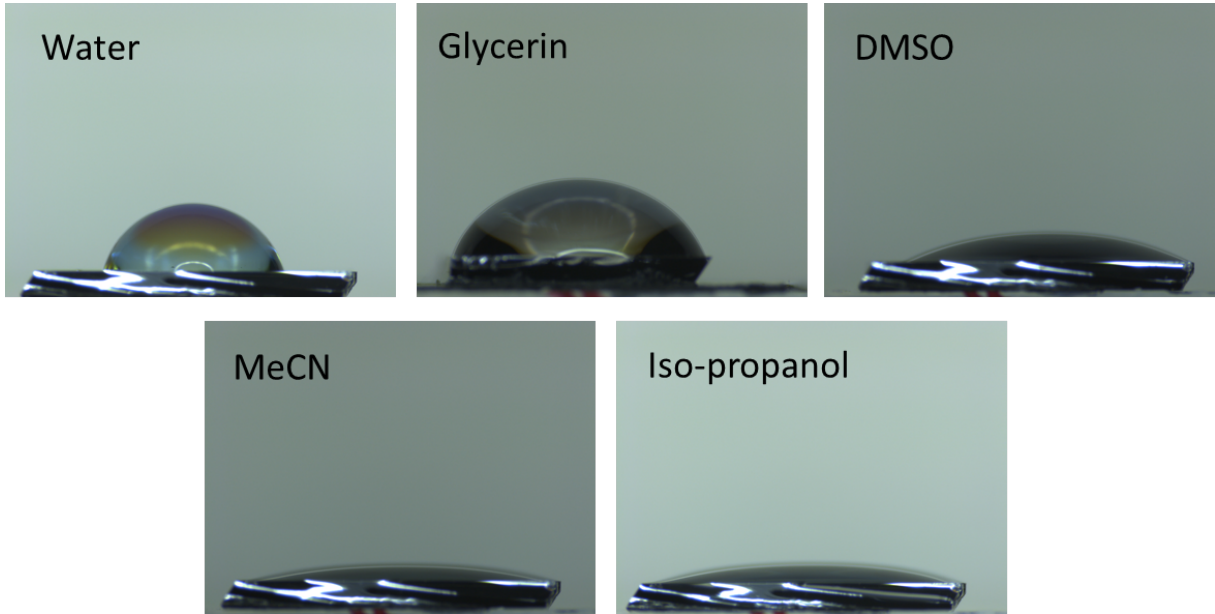


Figure 3.19: Examples for optical images after deposition of five different solvents( water, glycerin, dimethylsulfoxide (DMSO), acetonitrile (MeCN) and isopropanol) on the TAPP-Br-graphene substrate.

Contact angles were measured digitally using the ImageJ software on both sides of the droplet and both values were averaged. To derive the surface energy from the contact angles, Neumann's equation of state theory<sup>80,81,97-99</sup>

$$\cos\theta = -1 + 2\sqrt{\frac{\gamma_s}{\gamma_l}}e^{\beta(\gamma_s - \gamma_l)^2} \quad (3.1)$$

with the contact angle  $\theta$ , the surface tension  $\gamma_l$  of the solvent and the surface energy  $\gamma_s$  of the substrate was rearranged to equation 3.2.

$$\ln \left[ \gamma_l \left( \frac{1 + \cos\theta}{2} \right)^2 \right] = -2\beta(\gamma_s - \gamma_l)^2 + \ln(\gamma_s) \quad (3.2)$$

The left part of the equation can be calculated with knowledge of the measured contact

angles. Further rearranging the right side of equation 3.2 leads to a second order polynomial, which can be used to fit the data of the surface tension against the calculated left side of this equation and fitting the data with said polynomial will give both missing parameters  $\beta$  and surface energy. The plotted and fitted data for all TAPPs is shown in figure 3.20.

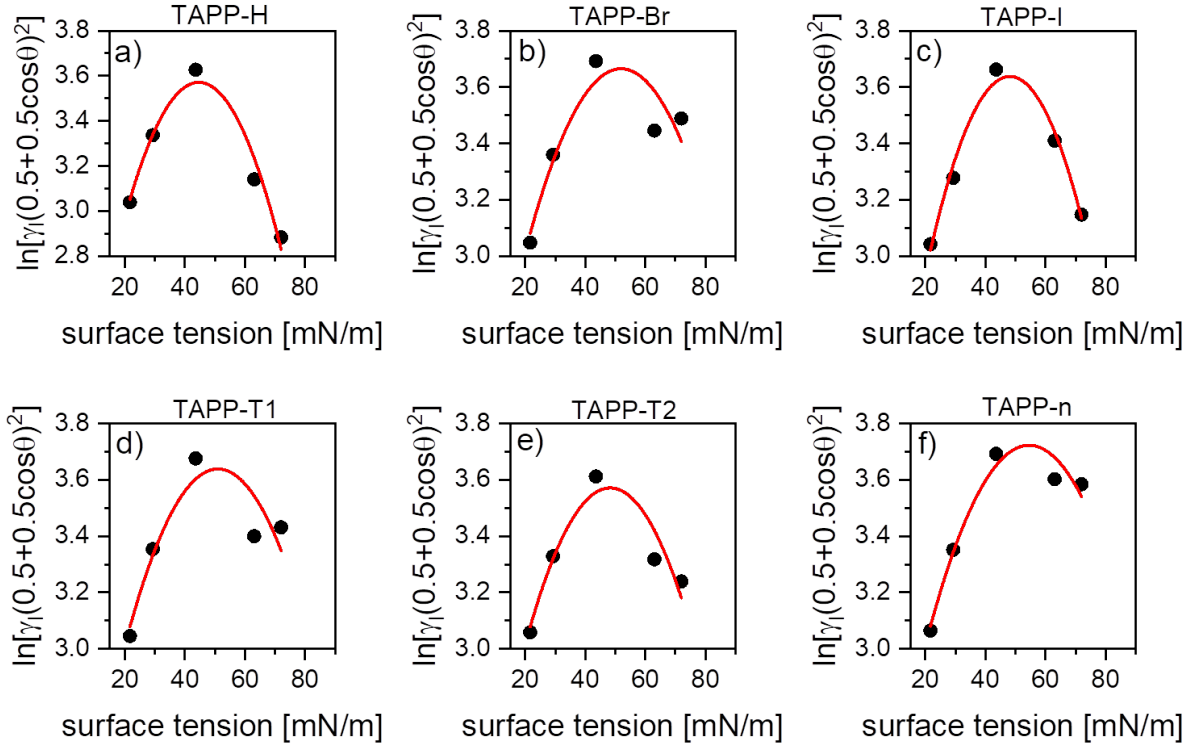


Figure 3.20: Polynomial fitting of calculated Neumann parameters  $\ln(0.5 + 0.5\cos(\theta))^2$  against the surface tension of the solvents used. From these plots and fits, the surface energy of the graphene-TAPP substrate can be calculated.

Following this procedure, the surface energies of the TAPP-modified graphene (on Si/SiO<sub>2</sub>) were obtained and the findings are shown in figure 3.21. Overall one can observe a variation of around 10 mN/m between the lowest value of around 45 mN/m (TAPP-H) to the highest value of around 55 mN/m (TAPP-n). The observed variation between halogen and thiophene substituted molecules ranges around  $\pm 5$  mN/m making it most likely not all too significant for device fabrication. However, it should be kept in mind that the overall surface energy of atomically thin graphene will also be influenced by the underlying substrate which seems to have a dominant contribution.

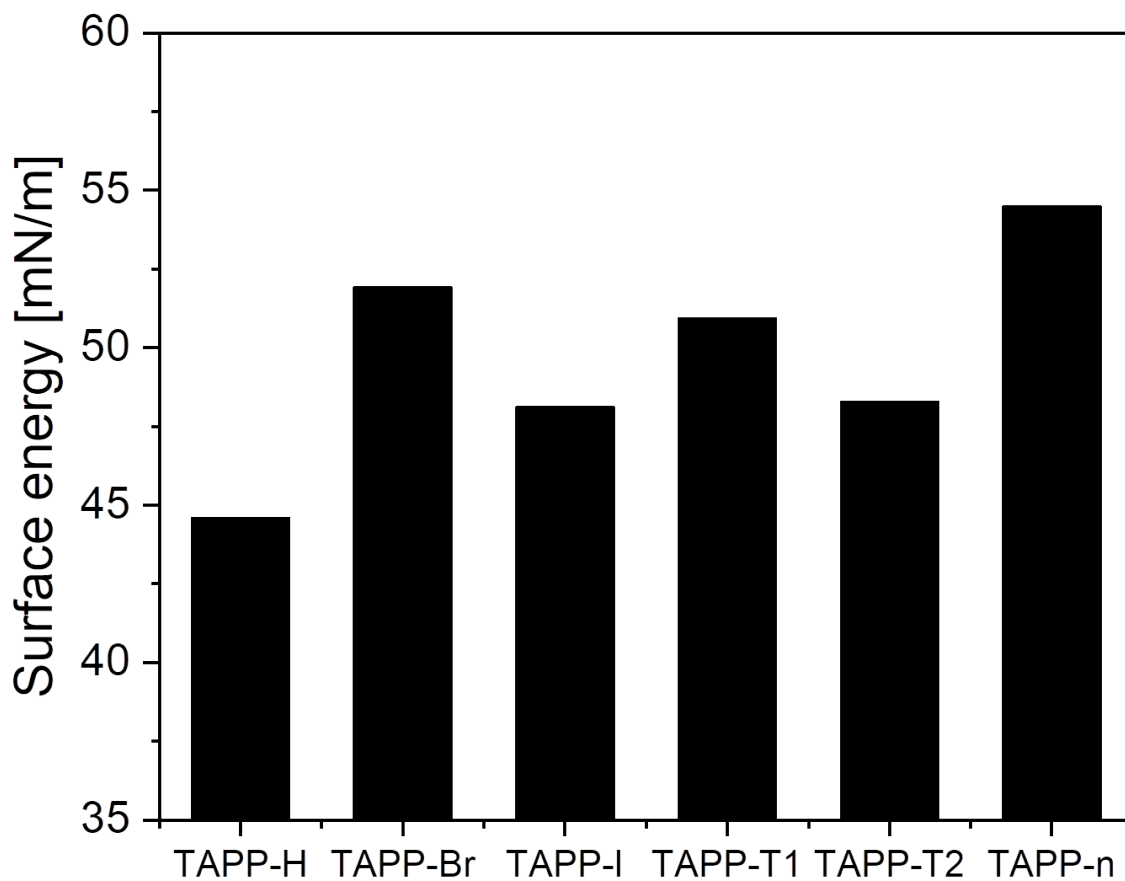


Figure 3.21: Surface energies for all TAPP molecules calculated with the Neumann model. Error values range between 0.01 and 0.025 and are thus not displayed.

## 4 Post-deposition Modification: UV Treatment and Protonation

Until now it was demonstrated that *N*-Heteropolycycles change both electronic and surface properties of graphene when assembled on the surface. Due to the versatile nature of organic molecules all kinds of additional functionalities can be introduced to tailor the properties further. In this chapter we explore two examples of such additional functionalities in the form of post-deposition modification with on-graphene oxidation of triangulenes (HTAs) and on-graphene protonation of benzonaphthyridines (BNs).

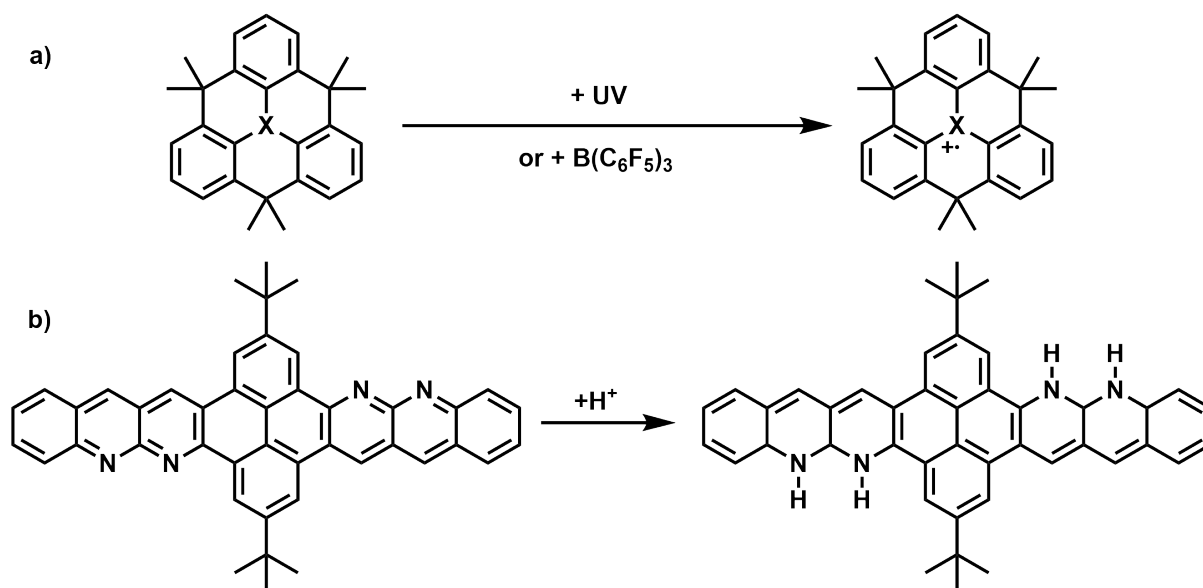


Figure 4.1: Possible modifications that can be achieved after deposition of molecules: a) oxidation of triangulenes to a radical cation with UV light or chemically with a borane<sup>23</sup>; b) protonation of the pyridinic nitrogen of benzonaphthyridines with mineral acids such as HCl.

## 4.1 UV-Treatment of Triangulenes (HTAs)

As before, the first step in investigating new molecules was to record absorbance spectra in particular to test potential resonance with the excitation laser in the Raman experiments. The normalized spectra in toluene are depicted in figure 4.2, all HTAs have a similar absorption profile with one single main absorption band around 300 nm without pronounced fine-structure. The absorbance in the UV region is to be expected due to the relatively small conjugated carbon backbone. In addition to that two molecules (MeO- and NH<sub>2</sub>) have a small absorption band, red-shifted to the main absorption. The triangulene derivative with a phosphorus atom at its center instead of nitrogen exhibits an ever further blue-shifted absorption that cannot be resolved due to the absorption of toluene in the UV region. Other solvents that have less absorption in this regime were unfortunately not suited for the HTAs. The dashed line in figure 4.2 indicates the Raman excitation that is of significantly lower energy than any absorption resulting in a non-resonant excitation, that is addressed later.

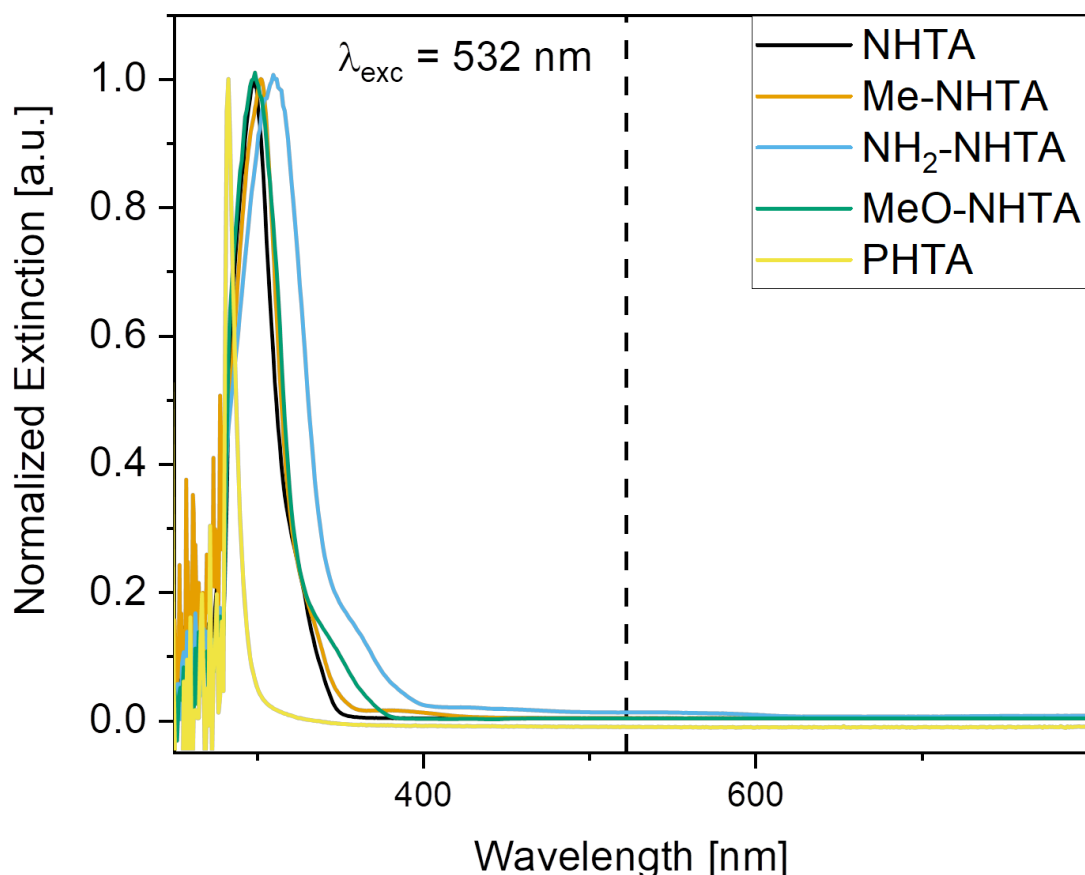


Figure 4.2: Normalized absorbance spectra of all HTAs in toluene and Raman excitation of 532 nm indicated as dashed line. All molecules show a single absorption band below 400 nm without pronounced vibronic fine-structure. For PHTA this absorption is blue-shifted to the solvent absorption region below 300 nm. Only for NH<sub>2</sub>- and MeO-NHTA a small additional absorption red-shifted to the main absorption can be observed.

As stated in the introduction of this section, the focus for the HTAs lies, in their ability to be oxidized to a stable radical cation. In addition, it should be noted that these molecules can be classified as electron donors in contrast to the previously investigated classes TAP and TAPP derivatives. The oxidation can be achieved via chemical oxidation<sup>23</sup> or potentially with ultra violet radiation as well, which would be a solvent-free alternative. To test this hypothesis, the solution of NHTA was irradiated for 2 hours with UV light (254 nm) and measured before and after via absorbance spectroscopy. As a reference, chemically-oxidized NHTAs were measured as well. These oxidized species have weakly-interacting counterions such as either  $\text{ClO}_4^-$  or  $\text{PF}_6^-$ . For the UV treatment of NHTA (4.3, a) an additional feature evolves at around 400 nm while the main absorbance feature is decreasing in its intensity. In comparison to that one can observe the same pattern of absorbance features for both chemically-oxidized molecules (4.3, b), even though the additional red-shifted feature appears at a different position, presumably due to the chemical environment being not exactly the same due to the counterions.

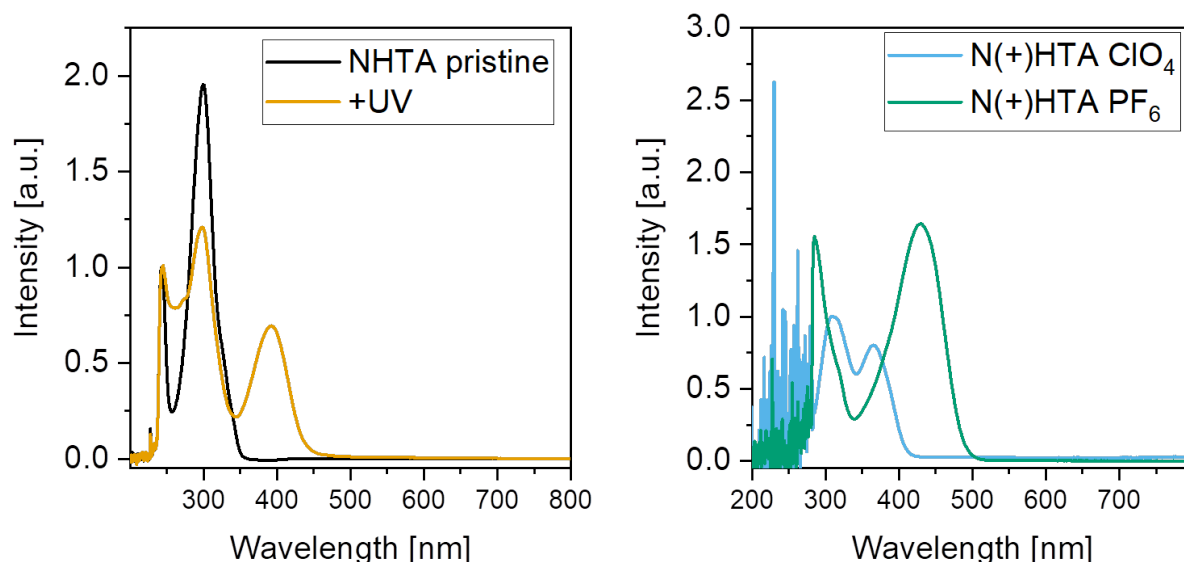


Figure 4.3: Comparison of NHTA treated with UV-light for 2h in chloroform solution (a) and chemically oxidized NHTA with two different weakly-interacting counterions (b). After UV treatment, NHTA shows a reduced intensity of the main spectral feature with an additional absorption at around 400 nm. Similar to that the chemical-oxidized species show the same pattern, however slightly shifted due to a different chemical environment.

The question arises, whether it is possible to achieve this kind of oxidation not only in solution, but also in films due to the relevant reaction taking place on graphene. For that purpose, NHTA was drop-casted onto a quartz substrate, irradiated and transmission spectra recorded. Again, after UV irradiation the same absorbance pattern can be observed (figure 4.4). Regarding the ratio of both absorbance features, it is evident that the conversion to the radical cation after irradiation is not complete or at least not as efficient as in solution which might stem from a lower mobility of the molecules in a film compared to a solvent environment.

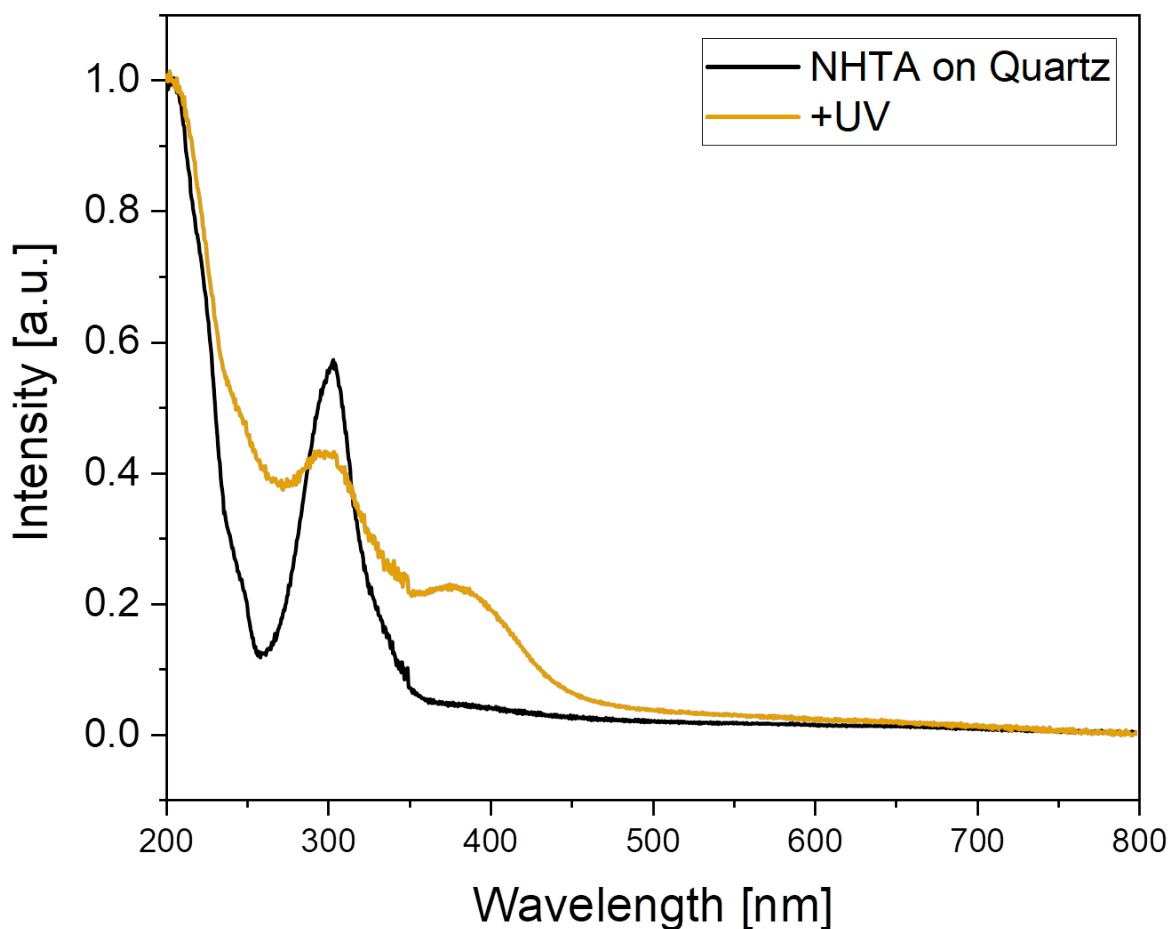


Figure 4.4: Comparison of drop-casted NHTA on quartz before (black) and after (yellow) 2h of UV irradiation (253 nm).

Nevertheless, this shows that conversion can take place on a substrate. In order to test whether the oxidation of the triangulenes on graphene through UV irradiation can be potentially used to modify the electronic properties of graphene, the established dip-coating protocol was used and the samples were measured with the standard Raman protocol, before and after 2h of UV irradiation after relocalising the same region. Prior to evaluating the Raman intensity ratio it is necessary to consider the possibility introducing defects into graphene with the UV radiation, as it is well known that UV radiation is capable of damaging the graphene lattice.<sup>100-102</sup> Figure 4.5 (left) shows the D- and G-band region of all average Raman spectra for all HTAs on graphene as well as a annealed graphene reference without any molecules. It is evident already from those spectra that the defect density does not significantly increase for molecule-coated graphene compared to the annealed reference. For better comparison the difference of the D to G ratio for all samples before and after UV treatment is shown as a histogram in figure 4.5 (right).

In contrast, the annealed reference however shows a significant change in D/G ratio with an increase of  $\sim 0.3$ , which is one order of magnitude higher than for the coated samples. This suggests that the molecules efficiently shield the graphene from damage. Interestingly, this is already achieved through the NMP treatment. Either way, this analysis shows that the 2D/G ratio can be assessed without variation in the defectiveness of the graphene playing a role.

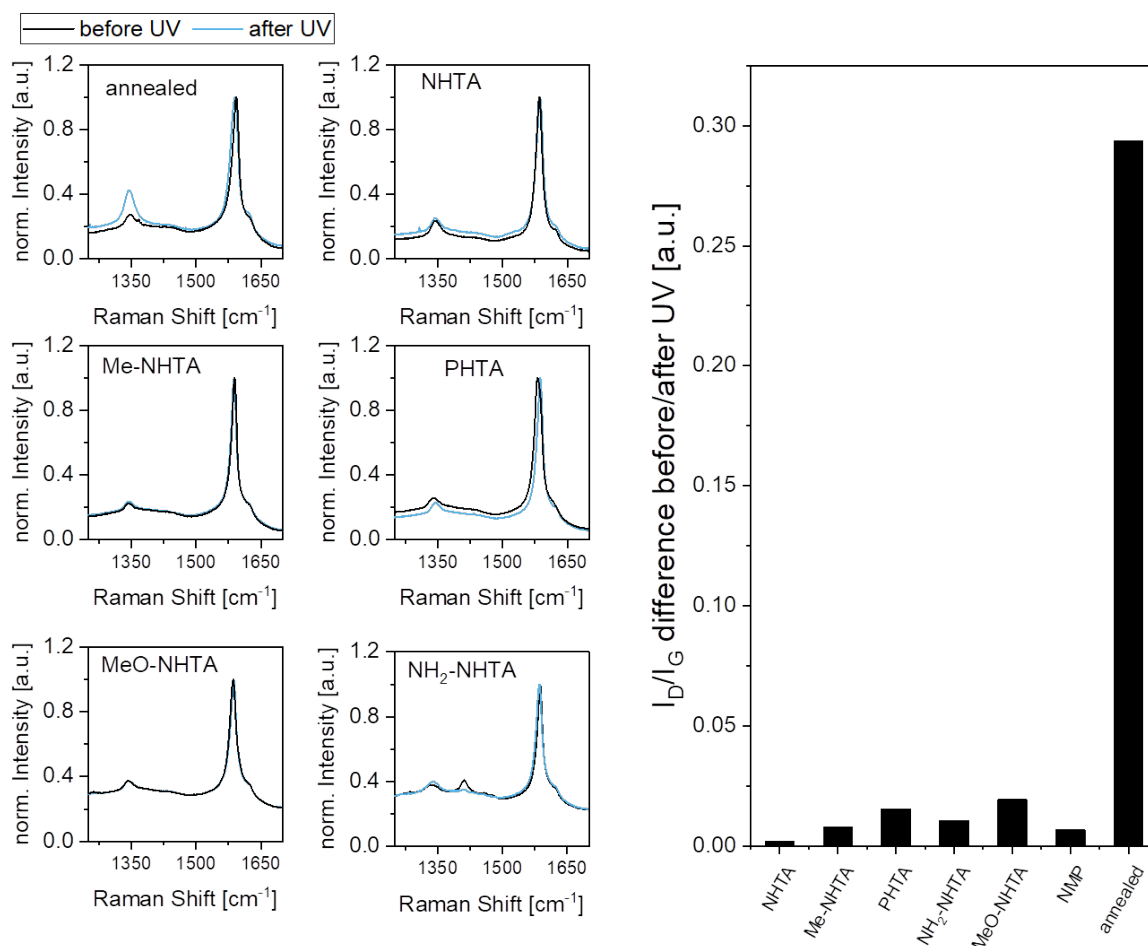


Figure 4.5: Normalized Raman spectra of all HTAs and an annealed reference showing G- and D-band region both before and after UV-treatment. Right: bar chart showing the change in D-band intensity after irradiation with no significant increase for coated samples, but for the plain graphene reference.

In addition, it is obvious that, in comparison to the Raman spectra of the previous molecules, almost no molecule vibration are visible as expected from the absorbance spectra (figure 4.2). A closer inspection of the Raman spectra of  $\text{NH}_2\text{-NHTA}$  reveals a small molecular signal around  $1400\text{ cm}^{-1}$ . This weakly resonant behavior can be confirmed by a more detailed investigation of the absorbance spectra (figure 4.6, b), where one can see a broad, low intensity absorption band between  $400\text{ nm}$  and  $600\text{ nm}$  that is resonantly excited by the  $532\text{ nm}$  Raman Laser. This small resonance also enables to record pure molecule spectra of drop-casted material on aluminum substrates (figure 4.6, a). The observed vibrations on graphene are in accordance to those measured without graphene and there seems to be no molecule vibration interfering with the G-band intensity. Due to structural similarity of all derivatives, we also expect no significant influence on the G-band intensity in the other cases, in particular due to the non-resonant excitation. Overall, these investigations nonetheless strongly suggest successful deposition.

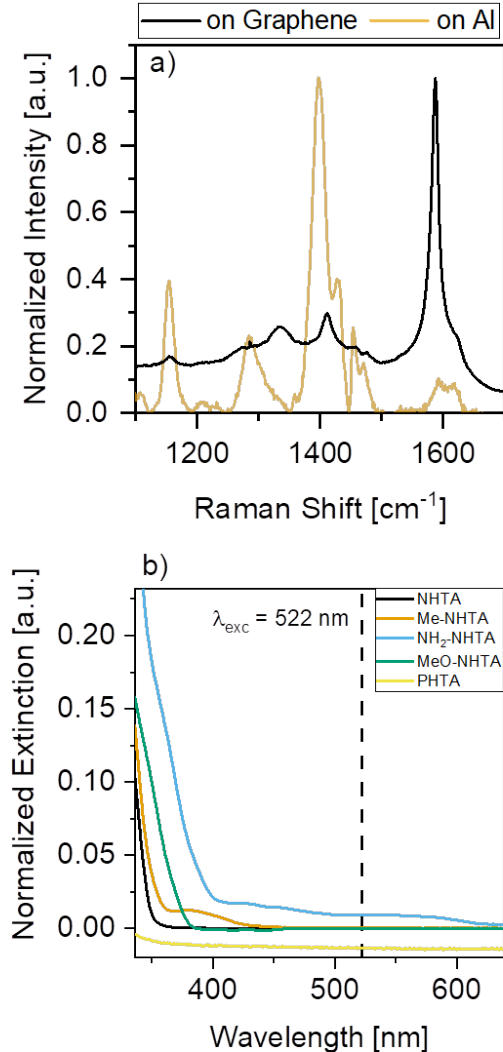


Figure 4.6: Overlay of molecular Raman vibrations for  $\text{NH}_2\text{-NHTA}$  (a) with (black) and without graphene (yellow) and zoom in on the absorbance spectra (b).

In the following the results of both Raman spectroscopy and KPFM will be discussed, which are summarized in figure 4.7. According to the theory (section 2.2.5) introducing more electrons into graphene should increase the Raman 2D/G intensity ratio of graphene. When starting at already p-doped graphene (due to the Si/Si<sub>2</sub> substrate) the Raman ratio will increase with increasing Fermi level to the point of neutrality, after which the Raman intensity ratio is expected to decrease again (figure 2.13). This trend is reflected in the Raman data (figure 4.7, a) where one can see an increase for all molecules after UV treatment except  $\text{NH}_2\text{-NHTA}$  where a minor decrease can be observed. Overall, the effect is not very pronounced. This is most likely due to rather weak interactions or low conversion rate to the radical cation. A full conversion and strong interaction that shifts the Fermi level past the neutrality point can be excluded due to chemical doping being

relatively moderate in its doping effect compared to electrical methods. Nonetheless, the trend is still observable and provides a proof of principle.

In contrast to the increase in the Raman 2D/G ratio, theory predicts a decrease in work function due to the shift to a higher Fermi level. The KPFM measurement results (figure 4.7, b) show this behavior as expected. This series of experiments shows, on the one hand, an example of post-deposition modification utilizing the ability of the trianguenes to be oxidized through UV-treatment. On the other hand, the overall approach circumvents the influence of molecular structure on the Raman and work function correlation. As seen previously for both TIPS-TAPs and TAPPs (figure 3.18) there is always an interplay between molecular orientation introducing additional shifts in work function and in case of the post-deposition modification of HTAs on graphene, the comparison before and after UV treatment occurs on the same sample region with the same molecular packing density and surface orientation, but different electronic properties, thus eliminating the structural factor that is present in all comparisons of molecule with different substituents. In spite of the effect being small, the theoretical cross-dependence of Raman intensity ratio and work function is observed. In future work, it will be important to increase the conversion rate or to apply the concept to other molecular systems with a more extended  $\pi$ -system that can be more easily observed.

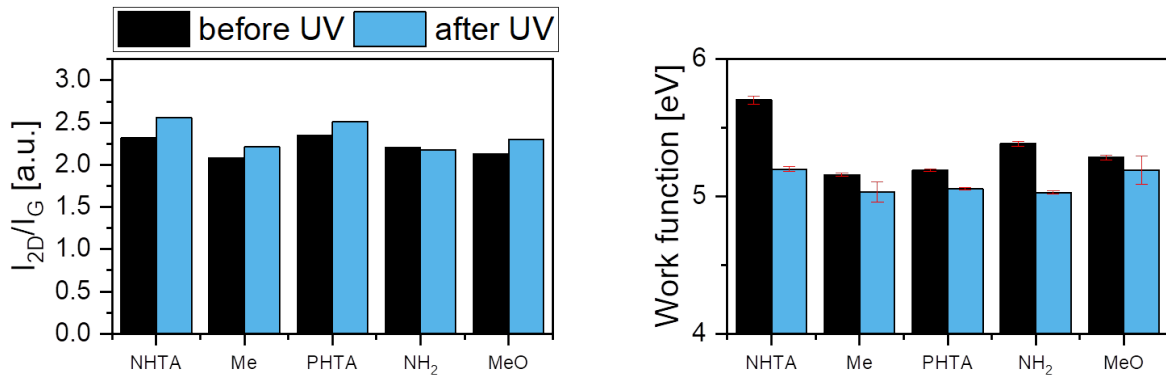


Figure 4.7: Summary of changes in Raman intensity ratio (a) and work function (b) before and after UV-treatment for all HTAs showing a corresponding trend of an increasing Raman intensity ratio with a decrease of the work function.

## 4.2 Protonation of Benzonaphthyridines

Another interesting property that potentially enables a secondary change of graphene properties after initial deposition of *N*-heteropolycycles is to protonate the *N*-functionality of the aromatic backbone using suitable acids. One type of molecules that can undergo this kind of protonation are benzonaphthyridines (BNs). The protonation can be followed by adsorption spectra. However, one has to bear in mind that the protonation can also have a significant impact on the solubility. This can lead to aggregation and a contribution from scattering to the optical spectra that are recorded in transmission mode. Thus, we refer to the spectra as extinction spectra in this case. The extinction spectra of both pristine and protonated BNs are displayed in figure 4.8 and show a change in the spectral profile. Overall, a red-shift and a broadening of the spectral features of the aromatic-backbone between 400 nm and 500 nm is observed that indicates a change in aromaticity due to protonation of the nitrogen sites of the acene structure. Qualitatively, the same behavior is observed for all three derivatives which can be rationalized based on the molecular structure, as to the only difference is the presence or absence of alkyl-sidechains with varying length. In addition to the red-shift and broadening of the transitions, a broad, featureless background is observed for 5BN and 8BN. We attribute this background to light scattering due to aggregation in the solvent used.

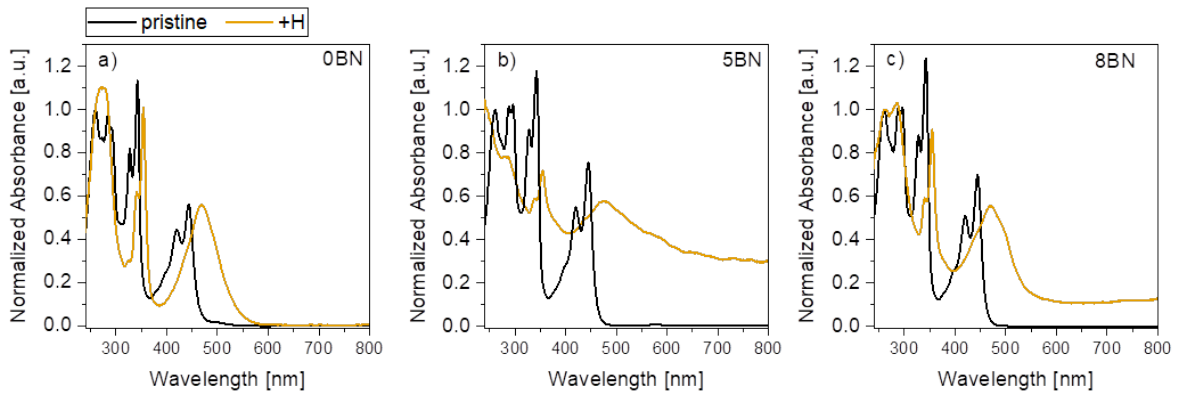


Figure 4.8: Comparison of pristine absorbance spectra (black) to spectra after protonation (yellow) for 0BN (a) 5BN (b) and 8BN (c) in toluene. Protonation was achieved by the addition of HCL. The characteristic electronic transitions of aromatic molecules are observed with vibronic fine structure. After protonation the transitions are red-shifted and the lowest energy transition is significantly broadened with no vibronic fine structure being observable any more.

To evaluate the impact on the graphene properties through protonation of the molecule, the BNs were deposited onto graphene through the established dip-coating followed by treatment with concentrated HCl. This treatment was done by dipping the graphene-molecule sample into the acid for 10 seconds with a subsequent gentle washing with distilled water and drying with nitrogen. In addition, the already protonated solution

was also used for dip-coating graphene to compare the on-graphene process to ex-situ protonation that was evidenced by extinction spectroscopy molecules. According to the extinction spectra, the resonance conditions are rather poor in the pristine molecules and it is thus expected that it will be difficult to see molecular vibrations in the Raman spectra (similar to HTAs and TAPs). However examining the Raman spectra (figure 4.9) molecular vibrations are well resolved and pronounced in all cases. For 8BN these are in accordance to the bare molecule spectra on aluminum. For 0BN and 5BN it was not possible to record vibrational spectra of the molecules due to an extremely strong fluorescence background that could not be eliminated. Apparently, the fluorescence is efficiently quenched through interaction with graphene. We attribute the pronounced vibrational modes after deposition on the graphene to a shift of the molecular absorbance into resonance. Overall the vibrations before and after HCl treatment look similar with only minor shifts and changes. However, the majority of vibrational modes might be only weakly affected through the protonation, in particular if it is incomplete which is likely. An in depth analysis including theoretical modeling of the main vibrational modes would be required to interpret the spectra comprehensively. This was not possible within the scope of this thesis. Nonetheless, an effect of the protonation on the graphene is manifested by an up-shift of the G-band in all cases which is most pronounced for 0BN.

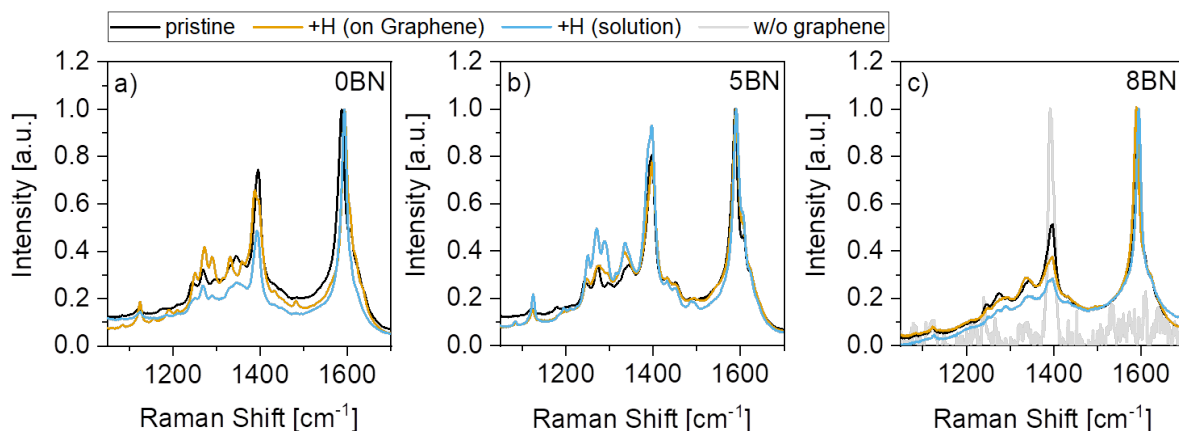


Figure 4.9: Comparison of Raman spectra around the molecular vibrations and the graphene G-band for 0BN (a), 5BN (b) and 8BN (c) as-deposited on graphene (black), protonated on graphene (yellow) and protonated in solution prior to deposition (blue). In the case of 8BN, it was possible to record a Raman spectrum on aluminum (gray).

To examine these trends in more detail, the Raman 2D/G intensity ratio was extracted and work function measurements conducted. The results of both are compared in figure 4.10. The first striking observation for the Raman intensity ratio (figure 4.10, a)) is the low ratio for 0BN compared to 5BN and 8BN. This is attributed to an increased packing density due to the missing alkyl-sidechains since the molecular core is otherwise identical (and hence the donor/acceptor strength). Note that the density of molecules per graphene area had no significant impact in the case of the previously investigated TIPS-TAP and

TAPP derivatives where the graphene doping was dominated by the electronic properties of the molecule. This is an interesting observation that merits further investigation in the future.

When focusing on the effect of protonation, a decrease in the 2D/G ratio is observed in all cases, sometimes more pronounced for on-graphene protonation, sometimes for depositing the protonated molecule. For 5BN and 8BN there seems to be a step by step transition from pristine molecule to protonated one with the on-graphene process being between the two references, indicating again an incomplete conversion. The same trend can be observed for the measured work function which shows an increase as expected from the decrease in Raman ratio in accordance with the theory. Again, similar to the HTAs the influence of surface dipoles on the work function are eliminated here by the comparison of the same (steric) structure of a molecule but different electronic properties. The changes are coherent in their trends both in Raman and KPFM measurements but the variations in absolute differences can currently not be fully rationalized, as they are more dependent on the length of the alkyl-sidechain than anticipated pointing towards significant differences in molecular packing density on graphene, which might also have an impact in the conversion efficiency

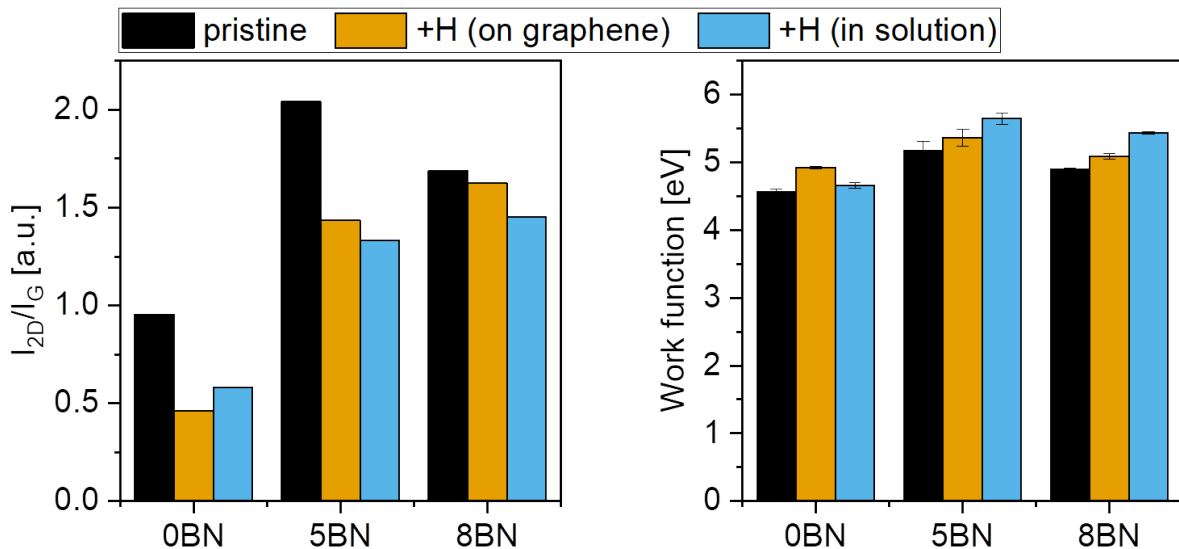


Figure 4.10: Summary of Raman (a) and work function measurements (b) for as-deposited BNs on graphene (black), protonated on graphene (yellow) and protonated in solution (blue).

## 5 Beyond Graphene: *N*-Heteropolycycles on Molybdenumdisulfide

### 5.1 Introduction

Depositing aromatic molecules on graphene will naturally be guided by the interactions between both molecular and graphene  $\pi$ - $\pi$  systems, thus leading to a self assembly of the molecules on the graphene surface. As discussed in detail in previous chapters, all interactions still depend on a range of different parameters, but the initial organization on the surface will be mediated by the aromatic interactions. This molecular self-assembly then leads to a charge transfer between both systems that results in a shift in Fermi energy of graphene through non-covalent chemical doping and opening a band gap.

Looking beyond graphene to other two-dimensional materials one of the more popular classes are transition metal dichalcogenites (TMDs) such as tungstendisulfide ( $\text{WS}_2$ ) or molybdenumdisulfide ( $\text{MoS}_2$ ). In general, those materials have a structure consisting of  $\text{MX}_2$  units, where M denotes a transition metal and X are chalcogen atoms. For the monolayer material this results in a transition metal layer that is surrounded by two chalcogenite layer both on top and bottom. Those materials can be produced by exfoliation in similar ways as describes for graphene due to the bulk TMD crystals consisting of layers that are only weakly bonded by van-der-Waals interactions<sup>103</sup>. In addition to exfoliation CVD-growth of TMDs is also a viable method in producing large areas of single crystal films<sup>104</sup> or flakes.<sup>105,106</sup>

TMDs show, similar to other two-dimensional materials, promising properties for electrochemical applications and electronics due to their semi-conducting properties that transition from a indirect band-gap semiconductor in the bulk phase to a direct-band gap in monolayers.<sup>107</sup> The progression of the bandstructure from bulk to monolayer material is shown in figure 5.1

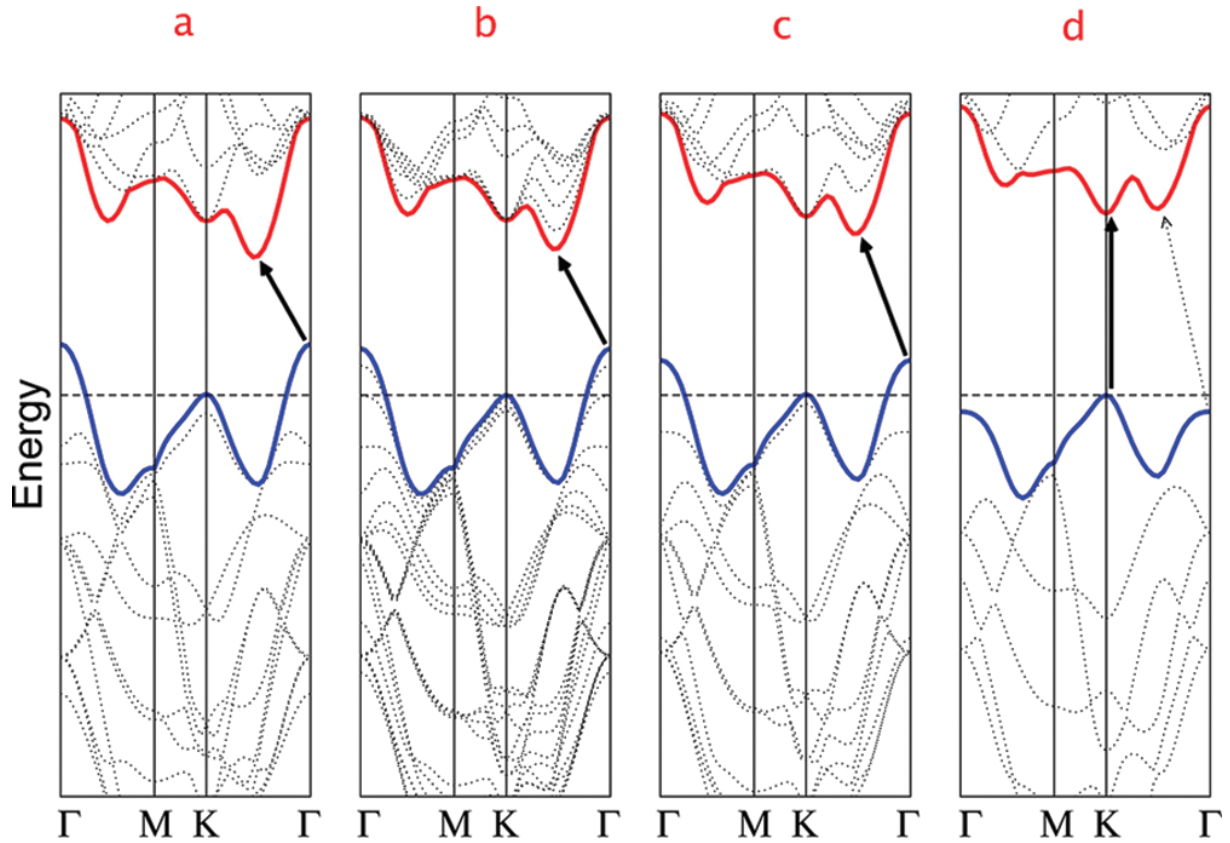


Figure 5.1: Evolution of the electronic band structure of MoS<sub>2</sub> from an indirect (a) to a direct band-gap semiconductor (d), by layer reduction. Adapted from Splendiani *et al.*<sup>107</sup>

Modifying these properties to improve and specifically engineer them to the desired application is an important step to further increase their utility in line with work on graphene. This can be done by covalent, non-covalent or coordinative attachment of molecules onto the TMD surface.<sup>108,109</sup> In our case, we again try to achieve a modification using a non-covalent assembly of the aromatic molecules. As with graphene, the main tool for identifying electronic changes in the material will be Raman spectroscopy. As described more in detail in section 5.2 the Raman spectrum is sensitive to electronic changes of the material itself.

However, with those materials lacking a large  $\pi$ -system, the molecular self-assembly seems not as intuitive compared to graphene. Although there is ongoing research regarding this<sup>108</sup> extending our already established deposition and evaluation protocols from graphene to other materials was worth considering. MoS<sub>2</sub> was chosen as model system for follow up experiments. In a similar fashion to the experiments with graphene, the following experimental work aims at a more detailed understanding of the interplay of organic molecules deposited on MoS<sub>2</sub>, to see whether and to what extent the electronic structure of MoS<sub>2</sub> can be influenced by non-covalent interactions, while, compared to other methods<sup>110</sup> keeping the pristine crystal structure of the material unaltered. To this end, the same methodology as developed for graphene was applied, using a dipcoating process in conjunction with Raman measurements to identify possible changes in the electronic structure.

The following chapters will first provide an overview over the electronic properties of MoS<sub>2</sub> as a basis for the subsequent evaluation of the acquired data of the Raman measurements.

## 5.2 Vibrational properties and Raman spectroscopy of MoS<sub>2</sub>

Similar to graphene, it is important to first understand the electronic and spectroscopic properties of the parent material to be able to rationalize the changes that will be introduced by non-covalent interactions with organic molecules. The crystal structure of MoS<sub>2</sub> (and comparable TMDs) is shown in figure 5.2. It consists of three single-atom layers with the transition metal between two layers of chalcogenite arranged in a honeycomb structure. Due to this structure, its Brillouin zone is similar to that of graphene<sup>111</sup> but with the main difference that TMDs are direct-bandgap semiconductors compared to the zero-bandgap nature of graphene. To be precise, the direct-band-gap is a property that emerges in TMDs when they are reduced to a single monolayer. Bulk TMDs show in contrast to monolayers a indirect band-gap.<sup>112</sup> In the following, TMDs are always referred to their respective monolayer due to the research done exclusively on single-layer material produces by CVD. To study the electronic properties and their changes we can utilize the same tools as in graphene, mainly Raman spectroscopy.

The evolution of the Raman modes from bulk to monolayer MoS<sub>2</sub> are well studied and contain information regarding the electronic structure. Group-theoretical investigations<sup>111</sup> reveal the existence of several Raman active modes for both a resonant and non-resonant excitation. Due to the excitation wavelength of 532 nm used in the following experiments (to keep measurements comparable to those done on graphene regarding the molecule excitations) the complex combination modes that become active under different resonance conditions will be disregarded here.

The four main lattice vibrations can be denoted (with respective Raman shift in parenthesis), according to group theory as E<sub>2g</sub><sup>2</sup> (32 cm<sup>-1</sup>), E<sub>1g</sub> (286 cm<sup>-1</sup>), E<sub>2g</sub><sup>1</sup> (383 cm<sup>-1</sup>) and A<sub>1g</sub> (408 cm<sup>-1</sup>). The E<sub>2g</sub><sup>2</sup> is related to two layers vibration against each other and therefore absent in the investigated monolayer samples. With the E<sub>1g</sub> mode being forbidden in measurements with a backscattering configuration only the E<sub>2g</sub><sup>1</sup> and A<sub>1g</sub> are relevant for our investigations. While the E<sub>1g</sub> mode corresponds to a in-plane vibration, the A<sub>1g</sub> originates from a out-of-plane vibration (schematic shown in figure 5.2)

It was shown that these two modes are sensitive not only to the layer number but also strain and charge carrier density and thus make identifying doping related changes possible.<sup>113</sup> The A<sub>1g</sub> mode will shift to lower wavenumbers with increasing charge carrier density and vice versa. The overall shifts however are rather small and are in a range of about 0.5 cm<sup>-1</sup> per 10<sup>13</sup> charge carriers per cm<sup>2</sup>, thus making precise measurements necessary to reduce any kind of scatter in the data that is not related to the doping effect. Regarding the E<sub>2g</sub><sup>1</sup> mode and its sensitivity to strain, a change in strain of about 0.1 % will lead to a shift of roughly 0.5 cm<sup>-1</sup>, but in our setup there are only minor changes to strain expected since the same area is probed pre- and post-deposition of molecules.

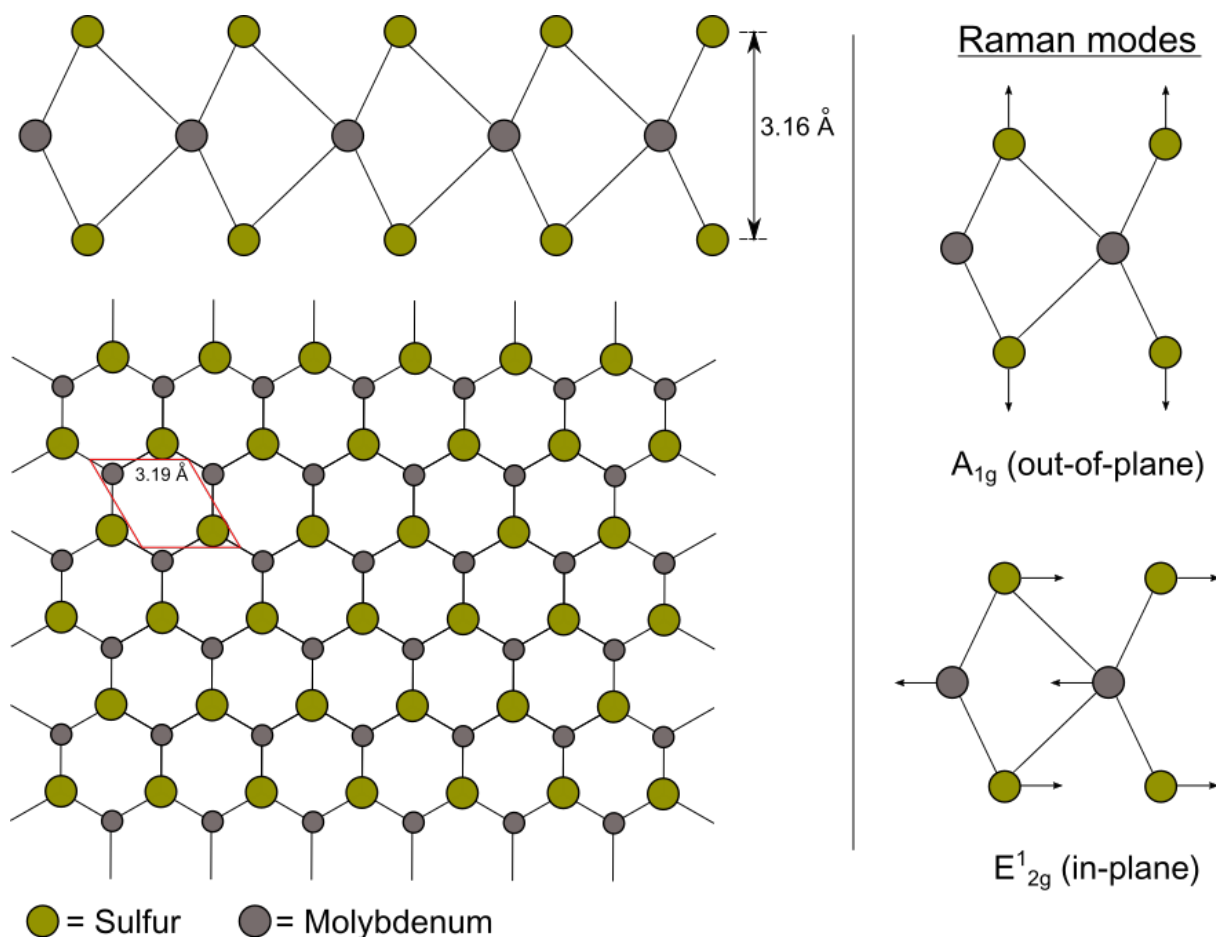


Figure 5.2: Structure of a MoS<sub>2</sub> monolayer from the side and top with corresponding in- and out-of-plane Raman modes.

When evaluating the Raman shifts to identify electronic changes, one has to keep in mind that, unless the material is measured in vacuum and in a free-standing state, there will be intrinsic doping. As shown previously (sections 2.2 and 3) graphene suffers from an intrinsic p-doping on Si/SiO<sub>2</sub> substrates. In case of MoS<sub>2</sub> there will be also a significant intrinsic doping stemming from the substrate that has to be considered. For MoS<sub>2</sub> on Si/SiO<sub>2</sub> an intrinsic n-doping is typically observed<sup>114</sup> in contrast to other substrates such as sapphire or mica. Additionally the intrinsic strain is also rather high on Si/SiO<sub>2</sub>, but that can be neglected in the following experiments, due to the molecules not introducing significant additional strain by simple deposition on MoS<sub>2</sub>.

### 5.3 Deposition of *N*-Heteropolycycles

To investigate the modification of MoS<sub>2</sub> through the deposition of *N*-Heteropolycycles the same deposition protocol was used as previously established for graphene. All solutions used were again 10<sup>-4</sup> mol/l and the dip-coating time was 10 minutes. Following the same reasoning as with graphene, commercial CVD-grown MoS<sub>2</sub> flakes from 6Carbon-Tech were used for the following experiments.

To verify the initial properties of the CVD-grown MoS<sub>2</sub>, Raman spectra were taken of the clean and unprocessed material. Figure 5.3 shows a representative Raman spectrum of the MoS<sub>2</sub> flakes with both the E<sub>2g</sub> and A<sub>1g</sub> vibrations visible at 384 cm<sup>-1</sup> and 405 cm<sup>-1</sup> respectively. Additionally a large broad signal around 4000 cm<sup>-1</sup> can be observed, that can be attributed to photoluminescence of MoS<sub>2</sub> when using the excitation wavelength of 532 nm. The signals at 520.6 cm<sup>-1</sup> and 980 cm<sup>-1</sup> stem from the Si/SiO<sub>2</sub> substrate. The ratio of the Raman to photoluminescence can be regarded as optical quality indicator of the sample, as doping, defectiveness and strain will have an even more pronounced effect of the photoluminescence than on the Raman modes<sup>107,115</sup>. With a PL to Raman (A<sub>1g</sub>) ratio around 11 the MoS<sub>2</sub> is sufficient for this experimental purpose. Since, unlike the CVD graphene MoS<sub>2</sub> was directly grown on Si/SiO<sub>2</sub>, the MoS<sub>2</sub> was used without any further cleaning or processing.

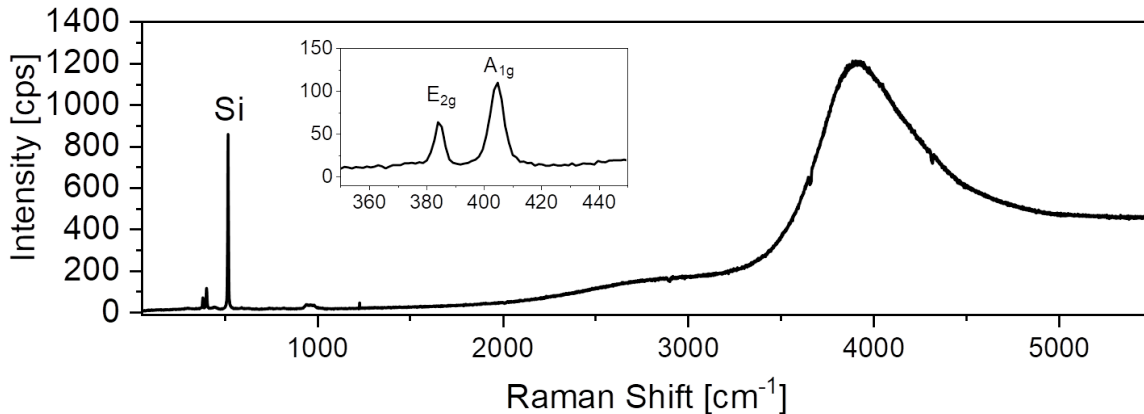


Figure 5.3: Raman spectrum of an as-grown MoS<sub>2</sub> flake showing the Raman signals of the underlying Si/SiO<sub>2</sub> substrate (520.6 cm<sup>-1</sup>, 980 cm<sup>-1</sup>) the E<sub>2g</sub> and A<sub>1g</sub> modes of MoS<sub>2</sub> at 384 cm<sup>-1</sup> and 405 cm<sup>-1</sup> respectively (insert) as well as a broad signal at 4000 cm<sup>-1</sup> related to the photoluminescence.

The molecules that were tested with MoS<sub>2</sub> are shown in figure 5.4 and include three tetraazaperopyrenes, a benzonaphthyridine and a perylenebisimide as an additional reference. The deposition of a similar PBI on MoS<sub>2</sub> has been investigated elsewhere previously<sup>116,117</sup> which allows for a comparison to the state of the art in literature. For the TAPPs and BN, molecules were chosen that showed a good molecular signal intensity on

graphene as well as good quenching of fluorescence without having too large substituents that could disrupt molecular assembly. Thus TAPP-H, -Br, and -I as well as 0BN were chosen, as they are the simplest variations of both classes of molecules, excluding TAPP-n that would require again NMP as different solvent for deposition.

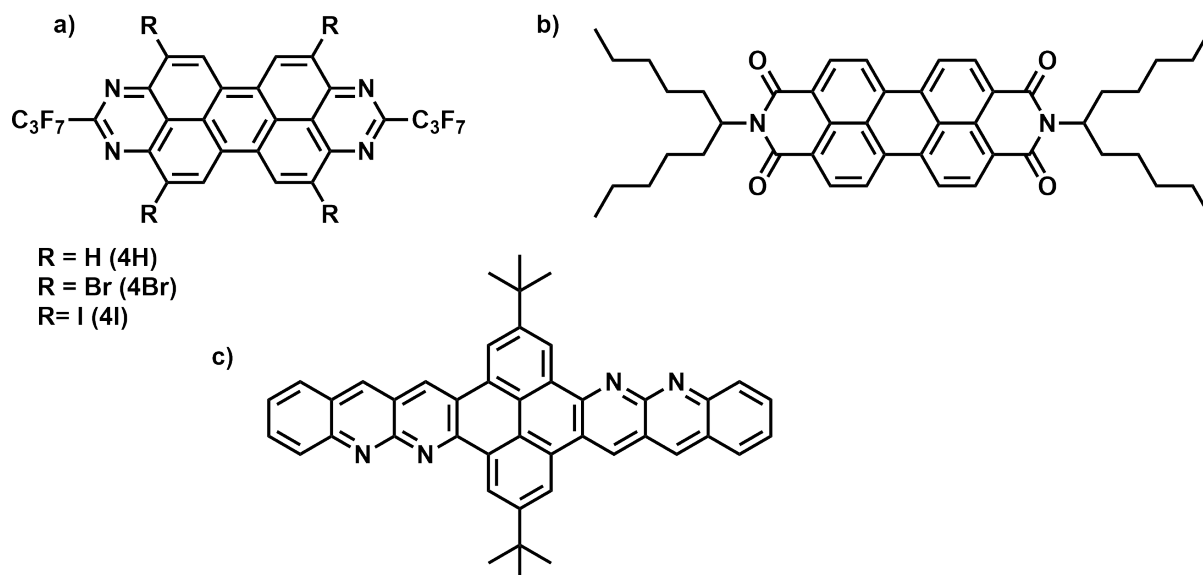


Figure 5.4: Overview of molecules deposited on MoS<sub>2</sub>. a) tetraazaperopyrenes (TAPP-H, -Br, -I), b) swallow-tail perylenebisimide (st-PBI) and c) benzonaphthyridine (0BN).

As st-PBI is a newly introduced molecule for this chain of experiments, its absorption properties were assessed in analogy to all other molecules. The absorbance spectrum is shown in figure 5.5 and it can be observed that it exhibits a similar characteristic profile compared to the TAPPs (section 3.4, figure 3.12), but with a red-shift that results in the molecule to be resonantly excited by the 532 nm Raman wavelength. This direct excitation might lead to a rather strong fluorescence in the Raman spectra if there is no fluorescence quenching present. Additionally it is the only molecule that is resonantly excited at the used Raman wavelength at all, which increases the sensitivity of the Raman measurements towards deposited molecule due to a higher Raman cross section. The absorbance spectra of the other molecules are displayed in figure 4.8 of section 4.2.

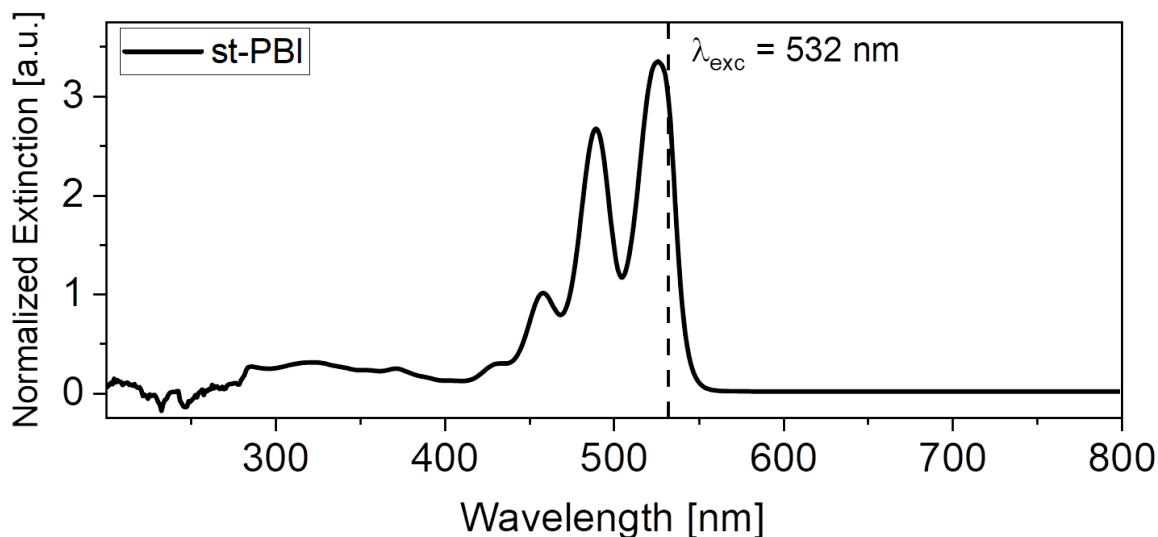


Figure 5.5: Absorption spectrum of st-PBI in toluene with a concentration of  $10^{-4}$  mol/l as it was used for deposition. Dashed line indicates the Raman excitation.

The second step in characterizing st-PBI, to draw a viable comparison to the other molecules, was to deposit it on graphene first, to see the impact on the Fermi energy, molecule intensity and fluorescence quenching. Note that similar PBIs have been extensively investigated in conjunction with graphene<sup>118</sup> and were found to form a densely packed layer on CVD graphene when deposited from solution with the aromatic cores in a vertical configuration. The resulting mean Raman spectrum, measured as described previously, is shown in figure 5.6 and reveals rather strong molecular vibrations below the G-band of graphene at  $1590\text{ cm}^{-1}$  as well as a vibration almost overlapping with the G-band itself. As such, the Raman modes of st-PBI are similar to those of the TAPPs, which is to be expected given their closely related molecular structure. Also similar to the TAPPs the Raman intensity ratio between 2D- and G-band is fairly low with a value of 0.75, showing that this molecule exhibits rather strong charge transfer. One key difference in the Raman spectrum compared to the TAPPs however is the abundance of additional smaller signals, especially around the 2D-band of graphene, that can be attributed to vibrations of the alkyl-chains that make up the swallow-tail-substituents. Regarding the fluorescence of the molecule, the Raman spectrum is not significantly affected by any background indicating again a packing that enables fluorescence quenching with graphene in agreement with literature<sup>119</sup>. Note that the intensity ratio of the molecular vibration to the graphene G-band exceeds previously reported intensity ratios using a PBI that were achieved after optimization of the packing density<sup>73</sup>. This conforms the robustness of the elaborated deposition protocol

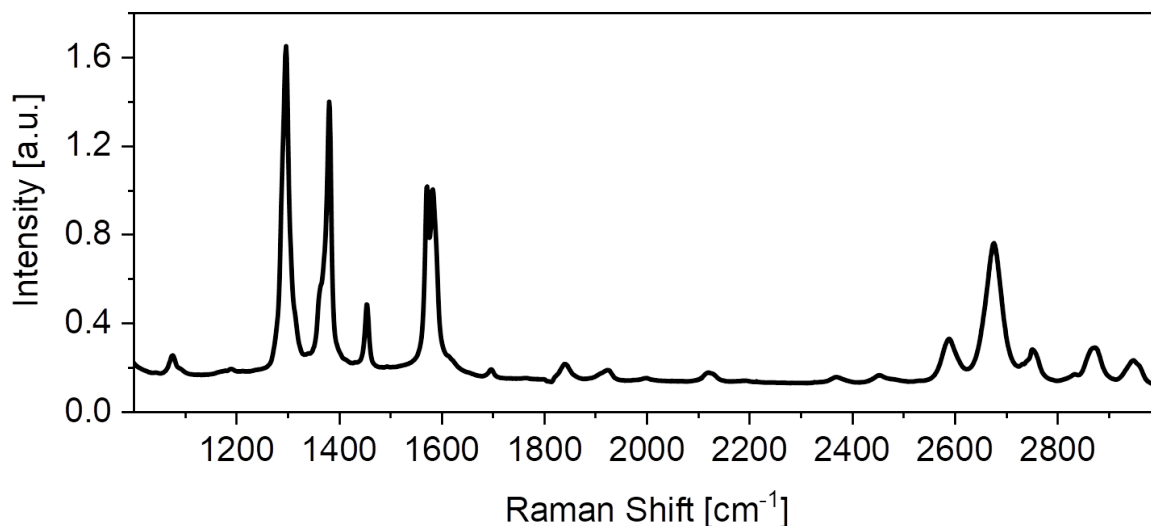


Figure 5.6: Raman spectrum of st-PBI on graphene showing a similar vibrational structure to the other perylenes with a vibration close to the graphene G-band at  $1590\text{ cm}^{-1}$  and a  $I_{2D}/I_G$  ratio of 0.75. Signals around the 2D-band at  $2690\text{ cm}^{-1}$  are related to vibrations of the alkyl-substituents.

With a comparison to literature established, all molecules under investigation were deposited onto  $\text{MoS}_2$  and evaluated using Raman spectroscopy.

The Raman measurements were carried out similar to graphene with two-dimensional maps recorded and the mean values of the desired parameters (details see section 8) extracted.

As a first comparison of  $\text{MoS}_2$  with all different molecules, the mean Raman spectra are displayed in figure 5.7. All perylene-based related molecules show a good intensity of their Raman vibrations comparable to the measurements done on graphene, as well as no apparent fluorescence, except for st-PBI. Here the excitation is resonant as shown previously in the absorbance spectrum (figure 5.5) compared to the off-resonant conditions for the three TAPP molecules. Therefore a small fluorescence background is visible for st-PBI but the molecular vibrations and the  $\text{MoS}_2$  features are still clearly discernible, showing that there is still quenching from the  $\text{MoS}_2$  present and in agreement with literature<sup>117</sup>. A comparison of those molecular vibrations to the bare molecule as done with the other molecules was not possible due to a strong fluorescence emerging without graphene or  $\text{MoS}_2$ .

One major difference can be observed with the 0BN-molecule, since here, the molecular vibrations are barely visible and not resolved as well as on graphene (figure 4.9), which suggests a rather sparse packing of the molecule on the material, although its acceptor strength is comparable to TAPP-H (figure 6.3).

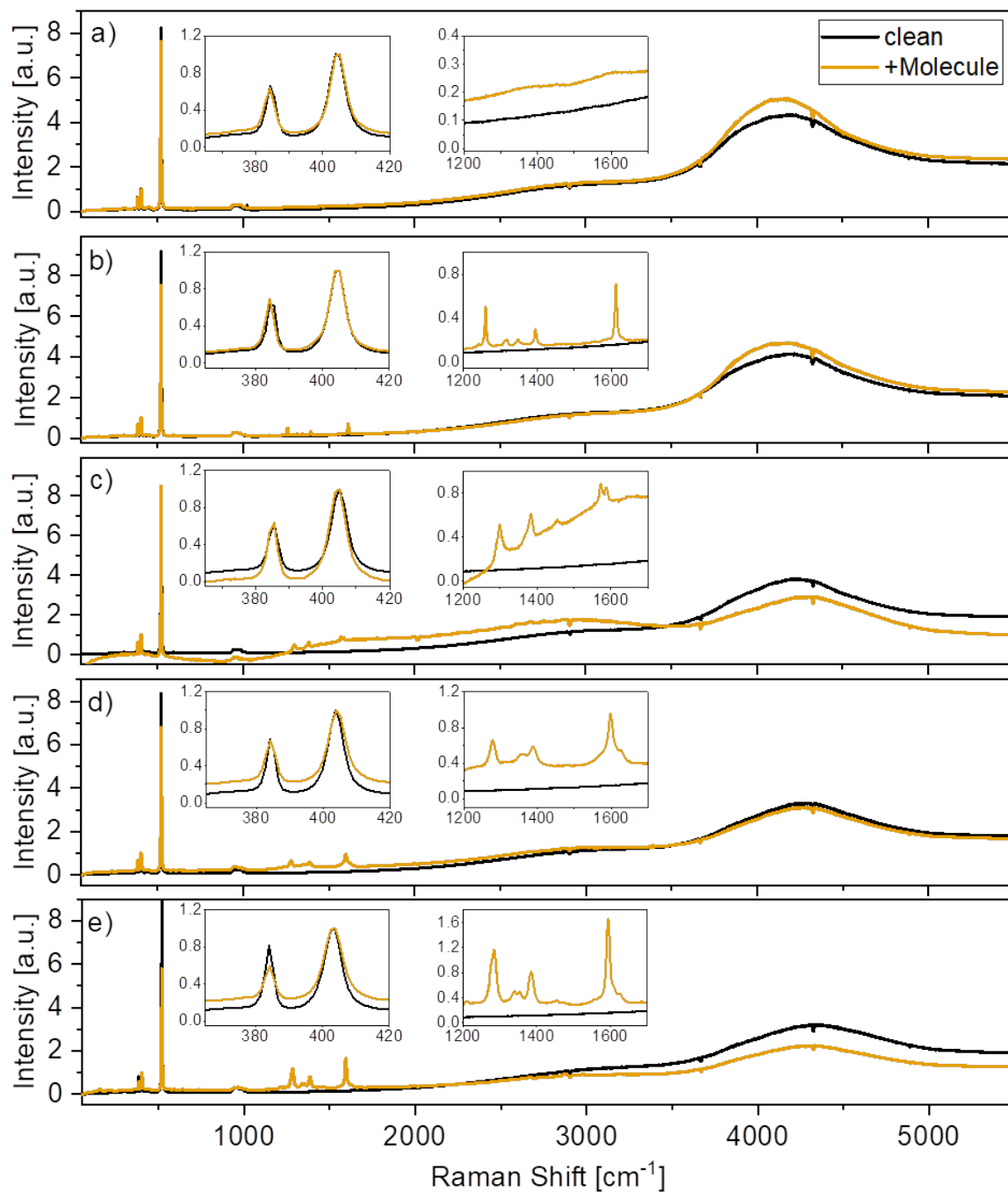


Figure 5.7: Raw (with only a constant baseline subtracted) Raman/photoluminescence spectra of pristine (black) and molecule-treated (yellow) MoS<sub>2</sub> for 0BN (a), TAPP-H (b), st-PBI (c), TAPP-Br (d) and TAPP-I (e). Inserts show magnifications of the MoS<sub>2</sub> and molecule vibrations.

As described above, both MoS<sub>2</sub> Raman signals are sensitive for strain ( $E_{2g}$ ) and carrier density ( $A_{1g}$ ). To visualize the effects on strain and carrier density, both spectral positions are correlated against each other in figure 5.8. All data points are mean values extracted from the measured Raman maps excluding regions with only bare Si/SiO<sub>2</sub> substrate. For each molecule-MoS<sub>2</sub> combination, 3 to 4 flakes were measured and averaged. The gray dashed lines indicate either equal strain or equal carrier density and are constructed with data from exfoliated MoS<sub>2</sub><sup>113</sup> and serve as a useful tool to identify changes in this overall small range of Raman shifts that is common for MoS<sub>2</sub> spectra<sup>120</sup>.

The first change that is visible is a distinct redshift for the  $E_{2g}$  position after deposition of the molecules, which indicates increasing strain in the material. In this case, strain might be not intuitive and misleading due to the material remaining flat on the substrate after treatment, but considering a vibration will always be influenced by its environment, adding an additional layer of molecules will lead to a certain constraint of vibrations thus leading to an effect that is similar to strain.

Regarding the shifts in carrier density, there is a small shift to lower concentrations visible for most acceptor-type molecules (TAPPs and OBN, figure 5.8 a), which is in agreement with theory and previous results on graphene. Overall the shift of carrier density is dependent on the properties of each molecule and individual MoS<sub>2</sub> flake, but the mean shift of all measurements (blue data points) shows a tendency to a reduced carrier density.

In contrast, st-PBI shows, an opposite trend regarding the carrier density which is tracked by a downward shift of the  $A_{1g}$  spectral position related to increasing electron density (figure 5.8 b). The changes in strain are comparable to the trends observed for the acceptor-type molecules.

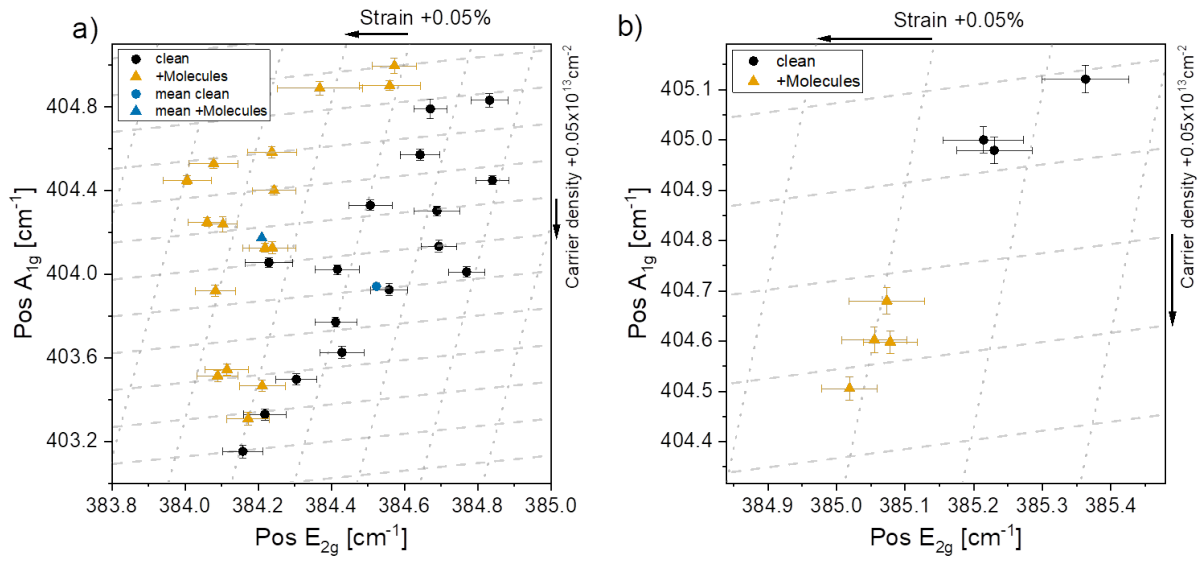


Figure 5.8: Plot of MoS<sub>2</sub> A<sub>1g</sub> versus E<sub>2g</sub> position representative of the carrier to strain ratio for MoS<sub>2</sub> flakes before (black) and after (yellow) molecule deposition. Blue data points show average over all measurements before and after treatment. Gray dashed lines indicate changes in strain ( $\pm 0.05\%$ ) and carrier density ( $\pm 0.05 \cdot 10^{13} \text{ cm}^{-2}$ ) based on exfoliated MoS<sub>2</sub><sup>113</sup>.

To understand this apparent discrepancy, it is important to consider the electronic structure of the molecules in more detail, especially the HOMO and LUMO energies (figure 6.3) to explain the acceptor/donor interactions. In case of the TAPPs (HOMO below -6.5 eV, LUMO  $4\pm 0.2$  eV) and 0BN (HOMO at -5.3 eV, LUMO at -3.3 eV), the LUMO energies lie close to the LUMO of MoS<sub>2</sub> at -4 eV.<sup>121</sup> Due to substrate interactions, we can assume that the MoS<sub>2</sub> is slightly n-doped.<sup>114</sup> This intrinsic n-doping and the aligned LUMO energies of the molecules suggest that the p-doping effect is the result of a charge transfer of the additional charge carriers of the substrate interaction to from MoS<sub>2</sub> to the LUMO of the molecules. With a difference of almost 2 eV, a charge transfer between the HOMO of MoS<sub>2</sub> (-6.1 eV) and the LUMO of the molecules seems unlikely. This is illustrated in figure 5.9 a).

A similar picture is observed at first glance in case of the st-PBI molecule. Here, the HOMO and LUMO energies are at -5.8 eV and -3.7 eV respectively. This should then lead to a similar charge transfer process as derived for the TAPPs and 0BN. However an increase in MoS<sub>2</sub> charge carrier density can be observed (figure 5.8). Taking the absorbance spectra into account, the PBI will be resonantly excited in the Raman measurement. This excitation during measurement could lead to a population of the LUMO level that then results in a charge transfer to MoS<sub>2</sub> due to the MoS<sub>2</sub> LUMO lying below the corresponding LUMO of st-PBI thus resulting in an observed n-doping of MoS<sub>2</sub>, as illustrated in figure 5.9 b).

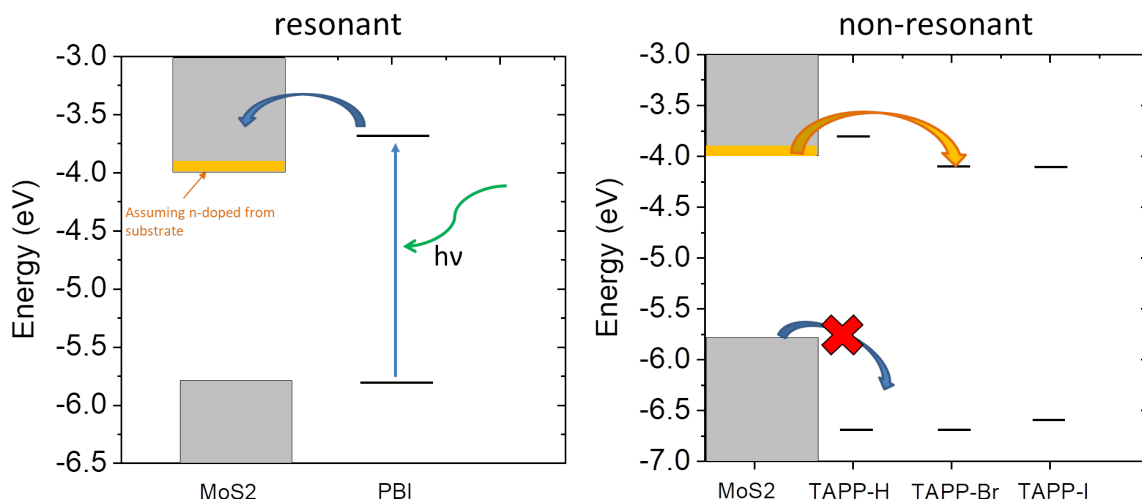


Figure 5.9: Graphical illustration of HOMO/LUMO level alignment and possible charge transfer processes in MoS<sub>2</sub> when in contact with organic molecules. a) resonant process with st-PBI resulting in n-doping. b) non-resonant process with TAPPs resulting in photo-induced p-doping.

In addition to changes in the Raman modes of MoS<sub>2</sub>, the deposition of molecules has an impact on the Raman photoluminescence (PL). From the average spectra (figure 5.7) the PL area was calculated by integrating the PL signal after subtraction of a horizontal baseline. As seen in figure 5.7 the overall fluorescence of the deposited molecules is rather low and seems not to overlap or interfere with the PL signal of MoS<sub>2</sub>, making this extraction of the PL area a viable method to evaluate possible changes in PL. In figure 5.10 a) it can be observed that the changes in PL are in correlation with the carrier density of the material represented by the A<sub>1g</sub> Raman mode of MoS<sub>2</sub>. Here, each data point corresponds to the result from mapping an individual MoS<sub>2</sub> flake before and after deposition of the respective molecule. Overall it can be seen that higher charge carrier densities (corresponding to lower A<sub>1g</sub> Raman shifts) lead to a lower overall PL and vice versa. Changes in strain on the other hand (represented by the E<sub>2g</sub> mode, figure 5.10 b) shows no clear correlation with the integrated PL area, which is to be expected due to the strain not being sensitive to the charge carrier as elaborated in section 5.2. When comparing the calculated PL before and after molecule deposition, one can distinguish the different molecules due to molecule specific trends of the PL. 0BN seems to lead to a constant PL area after deposition that is independent from the original PL. A similar trend can be observed with the deposition of TAPP-I where the resulting PL is also independent of the PL of the respective flake prior to deposition. The main difference between those two molecules however is the absolute magnitude of the PL, with 0BN showing a almost three times larger PL area than TAPP-I. In contrast to that TAPP-H shows only a minor increase in PL after deposition and TAPP-Br exhibits on average a small decrease in PL. The swallow-tail PBI, as the only donor type interaction shows a rather strong decrease in PL after deposition. The findings are summarized in the plot of PL area after deposition of the molecule as function of the PL area of the same flake prior to deposition. Unfortunately, a full interpretation of the data is beyond the scope of this work, as it would require extensive statistics on a high quality MoS<sub>2</sub> where the initial strain was released. However, it is clear that the optical properties of CVD MoS<sub>2</sub> can be significantly altered through noncovalent functionalization.

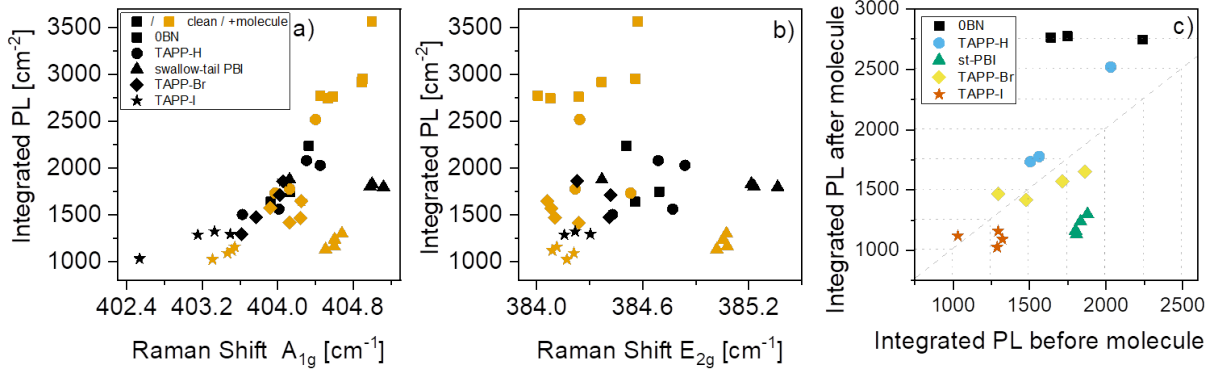


Figure 5.10: Integrated photoluminescence in comparison to both A<sub>1g</sub> (a) and E<sub>2G</sub> (b) Raman shifts as well as a correlation of photoluminescence before and after molecule deposition (c). The diagonal dashed lines in c) indicates the area of no change in PL after deposition, horizontal and vertical dotted lines indicate constant PL.

As already mentioned, to measure Raman shifts before and after deposition of molecules, Raman mapping was performed and the data averaged over the flakes. These measurements can also be used to visualize the intensity distribution of both MoS<sub>2</sub> and molecule to investigate the homogeneity of the coverage. Figure 5.11 shows the intensity of the A<sub>1</sub> vibration of MoS<sub>2</sub> and the most intense vibration of TAPP-H. All contour maps show the outline of the measured flakes, due to the intensity of the A<sub>1g</sub> mode not being affected by the doping. The maps were adjusted during measurements to also include some areas besides the flakes to better image them in relation to the bare Si/SiO<sub>2</sub> substrate. The homogeneous intensity of the A<sub>1g</sub> mode confirms no variations in MoS<sub>2</sub> thickness. The molecular vibration at 1610 cm<sup>-1</sup> also outlines the flakes rather well showing that the self assembly primarily occurs on MoS<sub>2</sub> and not on the blank substrate. The distribution of molecule on the flake itself appears not perfectly homogeneous which hints to a seeding at several spots where the self-assembly takes place separately, or the local formation of multilayers. However, complementary techniques with higher lateral resolution would be required to shine light on the details of the self-assembly. This low amount of spectra that basically represents pixel size and thus rather low resolutions is simply a result of keeping the measurement time per flake in an acceptable range. Higher resolution images are possible but will take significantly longer and one has always to consider a balance between measurement time and possible use of the acquired data. Nonetheless the collected data confirms a specific interaction occurring between molecules and MoS<sub>2</sub> that is absent for the substrate leading to this rather distinct local deposition through self-assembly.

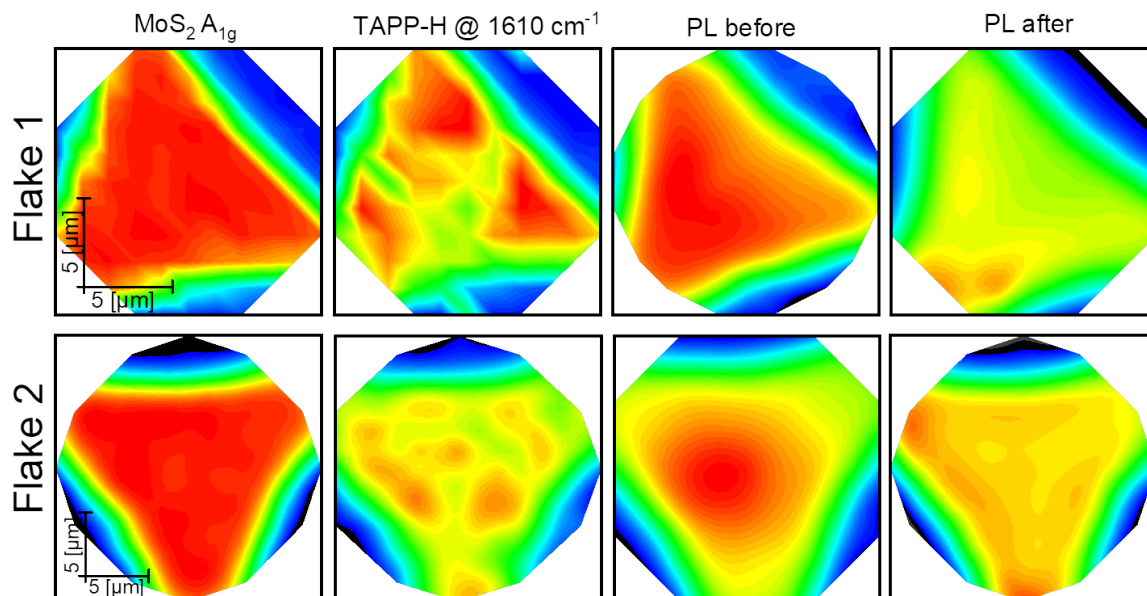


Figure 5.11: Examples of spacial distribution of Raman intensities for MoS<sub>2</sub> (A<sub>1g</sub> mode) and TAPP-H @ 1610 cm<sup>-1</sup> for two different flakes. Color scale ranges from blue for no to low intensity to red for high intensity.

A further property of MoS<sub>2</sub> that is affected by the interaction with the molecules is the photoluminescence, that can be seen as the broad Raman signal around 4000 cm<sup>-1</sup> (figure 5.3). The change in photoluminescence after deposition of TAPP-H (figure 5.11) seems not to be correlated to the distribution of the molecule itself since the PL is decreased homogeneously over the center flake area in contrast to the clustered molecule deposition. To further investigate whether the deposition behavior changes with different substituents for the series of TAPP derivatives, contour maps for TAPP-Br and TAPP-I were also constructed from the Raman measurements. Considering the same molecular vibration (differences in Raman shift are due to different force constants created by heavier substituents) for TAPP-Br (figure 5.12), one can distinguish a clear difference to TAPP-H. The self-assembly still takes only place on the flake itself and not on the SiO<sub>2</sub> substrate as the intensity of the molecular vibration outlines the MoS<sub>2</sub> flake similar to the A<sub>1g</sub> vibration of MoS<sub>2</sub> itself but in contrast to TAPP-H, TAPP-Br seems to be more evenly distributed on the surface without forming major clusters. At the edges of the measured Raman map, in the direction of the tips of the MoS<sub>2</sub> triangles however, an increased molecule intensity can be observed hinting at a more clustered deposition in this area. The PL shows here no correlation to the molecule distribution as well. Flake 1 displays a PL decrease in proximity to the edges while Flake 2 only shows a slight overall decrease in PL intensity after TAPP-Br deposition.

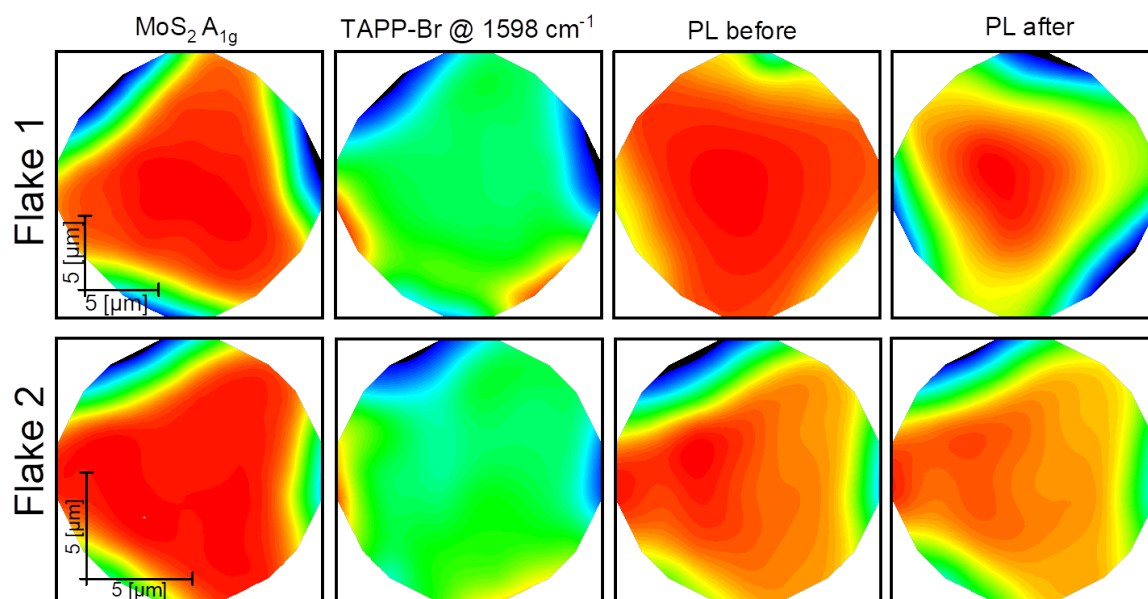


Figure 5.12: Examples of spacial distribution of Raman intensities for MoS<sub>2</sub> (A<sub>1g</sub> mode) and TAPP-Br @ 1598 cm<sup>-1</sup> for two different flakes. Color scale ranges from blue for no to low intensity to red for high intensity.

A similar result to the TAPP-Br deposition can be observed for TAPP-I, with again a rather homogeneous distribution of molecule over the MoS<sub>2</sub> flake with emerging molecule clusters toward the tips of the triangle (figure 5.12). As with all other molecules the molecule targets the MoS<sub>2</sub> for self-assembly leaving the substrate un-coated. The overall changes in PL for TAPP-I are minor and show no significant difference in PL near the clusters of molecules observed in the contour map for the molecular vibration.

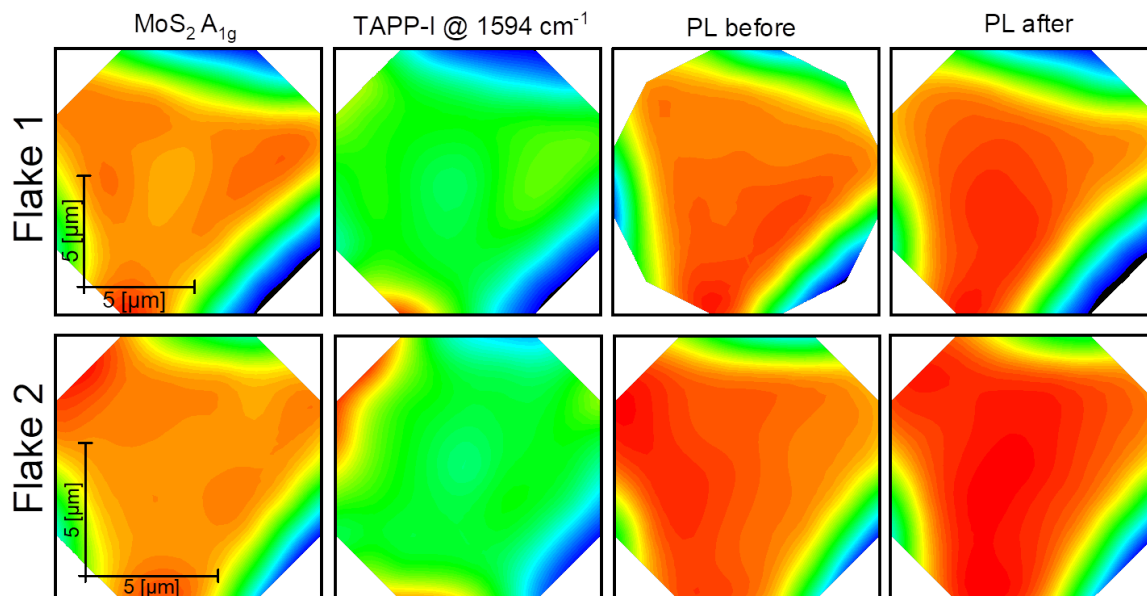


Figure 5.13: Examples of spacial distribution of Raman intensities for MoS<sub>2</sub> (A<sub>1g</sub> mode) and TAPP-I @ 1594 cm<sup>-1</sup> for two different flakes. Color scale ranges from blue for no to low intensity to red for high intensity.

Comparing the molecule intensity of TAPP-H to that of 0BN (mean spectra, figure 5.7) one can clearly see that there is a huge difference with 0BN showing almost no molecule intensity at all compared to the results on graphene (figure 4.9). While the resonance condition for TAPP-H and 0BN are comparable (slightly more favorable for TAPP-H) on MoS<sub>2</sub> they seem to exhibit different packing behaviors on MoS<sub>2</sub> compared to graphene. Considering the  $\pi - \pi$  interaction governing the assembly on graphene something else has to be the key factor on MoS<sub>2</sub>. Both molecule do not have any large and steric demanding substituents that could interfere with the packing on the surface, thus the assembly is most likely dependent on intrinsic properties like donor/acceptor strength. Looking back at the induced Raman shifts in graphene that are as shown, related to the FMO energies in figure 3.17 and 4.10, TAPP-H ( $I_G/I_{2D} = 1.7$ ) shows a weaker acceptor interaction than 0BN ( $I_G/I_{2D} = 0.95$ ) suggesting that a strong (in this case) acceptor interaction on graphene does not translate directly to MoS<sub>2</sub>. This can be seen in figure 5.9 with the alignment of both LUMOs being significantly different, with TAPP-H having a LUMO energy of -3.77 eV and 0BN of -3.3 eV compared to MoS<sub>2</sub> with -4 eV.

In conclusion, transferring the deposition protocol from graphene to MoS<sub>2</sub> was successful and even though there were no additional optimizations done for MoS<sub>2</sub> very encouraging preliminary results were obtained. Mean spectra of the MoS<sub>2</sub>/molecule structures reveal a quenching of fluorescence since no major contribution to the background can be discerned and the molecule vibrations are clearly visible. However, there is a major difference in molecule intensity between the perylenes and the benzonaphthyridine, with the second showing very little intensity after deposition in contrast to the experiments

on graphene. The donor/acceptor interactions can be clearly identified and separated, although the overall doping effect is still rather small as seen already on graphene. For acceptor-type molecules, the strain-charge carrier plot reveals a decrease in charge carrier density as expected while donor-type interactions produce an increase in carriers. The strain is increasing about 0.1 % on average after deposition which can be neglected. The difference in MoS<sub>2</sub> charge carrier density after deposition of the different acceptor-type molecules is attributed to a reduction of the intrinsic MoS<sub>2</sub> n-doping in the case of TAPP and a photo-induced charge transfer in the case of the PBI which is resonantly excited by the Raman excitation wavelength.

Correlation of the observed Raman photoluminescence to the induced charge carrier density and thus the A<sub>1g</sub> Raman shift shows a clear dependence that suggests a higher overall PL with a lower charge carrier density. However, comparing the PL before and after molecule deposition shows different behaviors for all molecules suggesting a more complex mechanism behind the influence on the PL than just a charge transfer interaction modifying the charge carrier density. Evaluation of the overall distribution of molecules on the MoS<sub>2</sub> flakes also shows distinct differences within the same family of TAPPs, with TAPP-H assembling in a more clustered fashion whereas TAPP-Br and TAPP-I show a more homogeneous distribution over the flakes.

In any case, it is clearly demonstrated that all perylene-based molecules have a high tendency to self-assembly on MoS<sub>2</sub>, while for example 0BN has nit. Comparing the molecule intensity of TAPP-H to that of 0BN (mean spectra figure 5.7) one can clearly see that there is a significant difference with 0BN showing almost no molecular vibrations in contrast to the results on graphene (figure 4.9). While the resonance condition for TAPP-H and 0BN are comparable (only slightly more favorable for TAPP-H), these two classes of molecules exhibit a different packing on MoS<sub>2</sub> contrasting the results from graphene. Considering the  $\pi$ - $\pi$  interaction governing the assembly on graphene, some other key factor is apparently responsible for the assembly on MoS<sub>2</sub>. Both molecules are not equipped with sterically demanding substituents that could interfere with the packing on the surface. Thus the assembly is most likely dependent on other properties such as donor/acceptor strength. While the LUMO of the TAPPP derivatives align reasonably well with the conduction band edge of MoS<sub>2</sub> (figure 5.9), this is not the case for 0BN with a LUMO energy of -3.3 eV. In the case of weakly doped MoS<sub>2</sub>, no charge transfer is expected. Thus, the results suggest that donor/acceptor interactions are at the origin of the self-assembly of *N*-heteropolycycles on MoS<sub>2</sub>. In summary, these results reveal a range of interesting phenomena that are worth investigating in future research projects to further unravel the more complex mechanisms behind molecule-TMD interactions. A further step here could be to investigate the local doping changes in MoS<sub>2</sub> by optimizing the Raman measurements to focus on the positional changes of the A<sub>1g</sub> mode in correlation to the molecule intensity. For this kind of analysis however, the Raman map resolution (i.e.

number of spectra) has to be increased to really pinpoint small local changes. Of course at this point the spectral range of the spectra has to be reduced to only include MoS<sub>2</sub> and molecule vibrations, to keep the overall measurement time per map at a reasonable time. In addition, complementary characterization techniques are required such as reflectivity, STEM/EDX, micro-XPS, or TOF-SIMS to name a few. In addition, it will be beneficial to work with free-standing MoS<sub>2</sub> where strain and substrate interactions were released prior to the measurements. Nonetheless, these preliminary investigations clearly demonstrate the potential of Raman spectroscopy to screen for interesting molecule-material combinations as foundation for future work.

## 6 Conclusions and Outlook

This thesis was aimed at gaining detailed insight into the structure-effect relation of non-covalent graphene/*N*-Heteroacene and MoS<sub>2</sub>/*N*-Heteroacene heterostructures. Achieving that was done by initially depositing a broad selection of *N*-Heteropolycycles (figure 6.1) onto CVD-grown graphene using a solution based dip coating procedure, to then extend the experiments to MoS<sub>2</sub> with the knowledge gained from graphene.

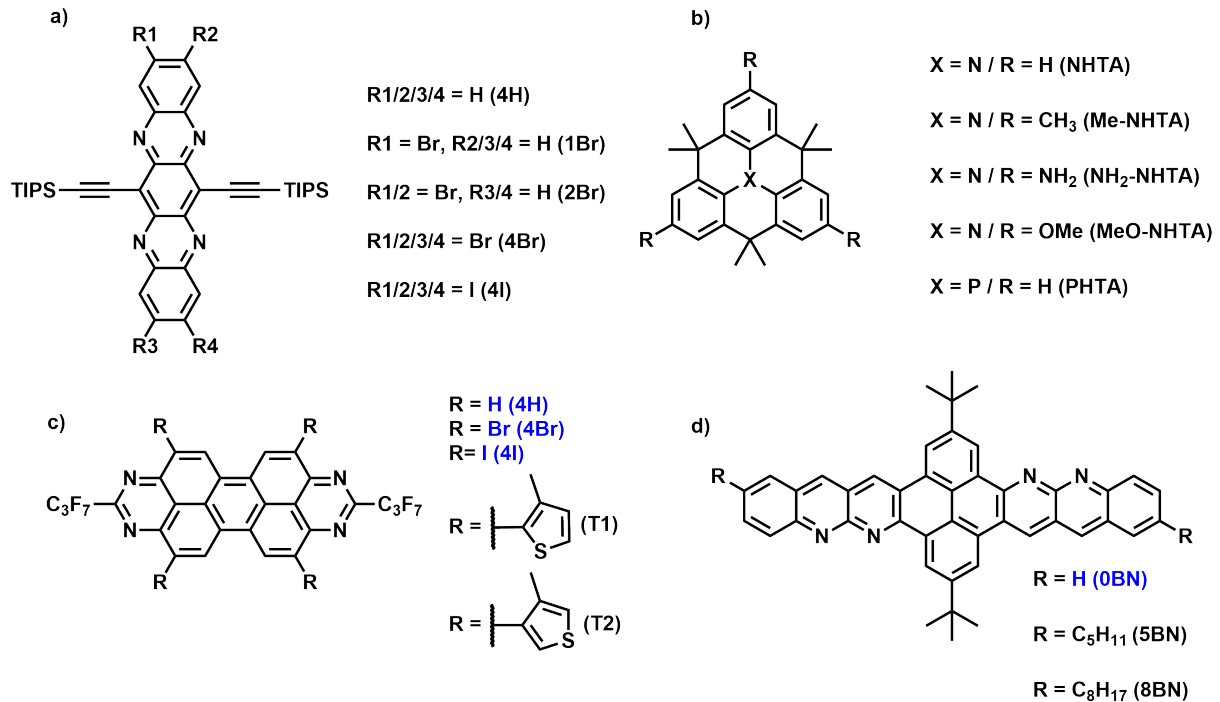


Figure 6.1: Summary recap of molecule families under investigation throughout this work. a) Tetraazapentacenes with different halogenation patterns. b) Triangulenes with different para-substituents. c) Tetraazaperopyrenes with different, more and less steric fourfold substituents. d) Benzonaphthyridines with different lengths of alkyl-sidechains. Blue marked molecules were the ones tested on MoS<sub>2</sub>.

Prior to all experiments involving graphene the molecules were investigated for their optical properties and resonance conditions for the later Raman measurements by absorption spectroscopy. The absorption spectra for all molecules depicted in figure 6.2 show that almost all molecules are excited non-resonant except the to thiophene-substituted TAPPs, which have their absorption bands red-shifted enough to fall onto the 532 nm Raman wavelength. Considering the Raman measurements these non-resonant conditions still lead to discernible Raman bands for all molecules except the triangulene family, where the overall absorption is too far blue-shifted resulting in only very minor Raman features.

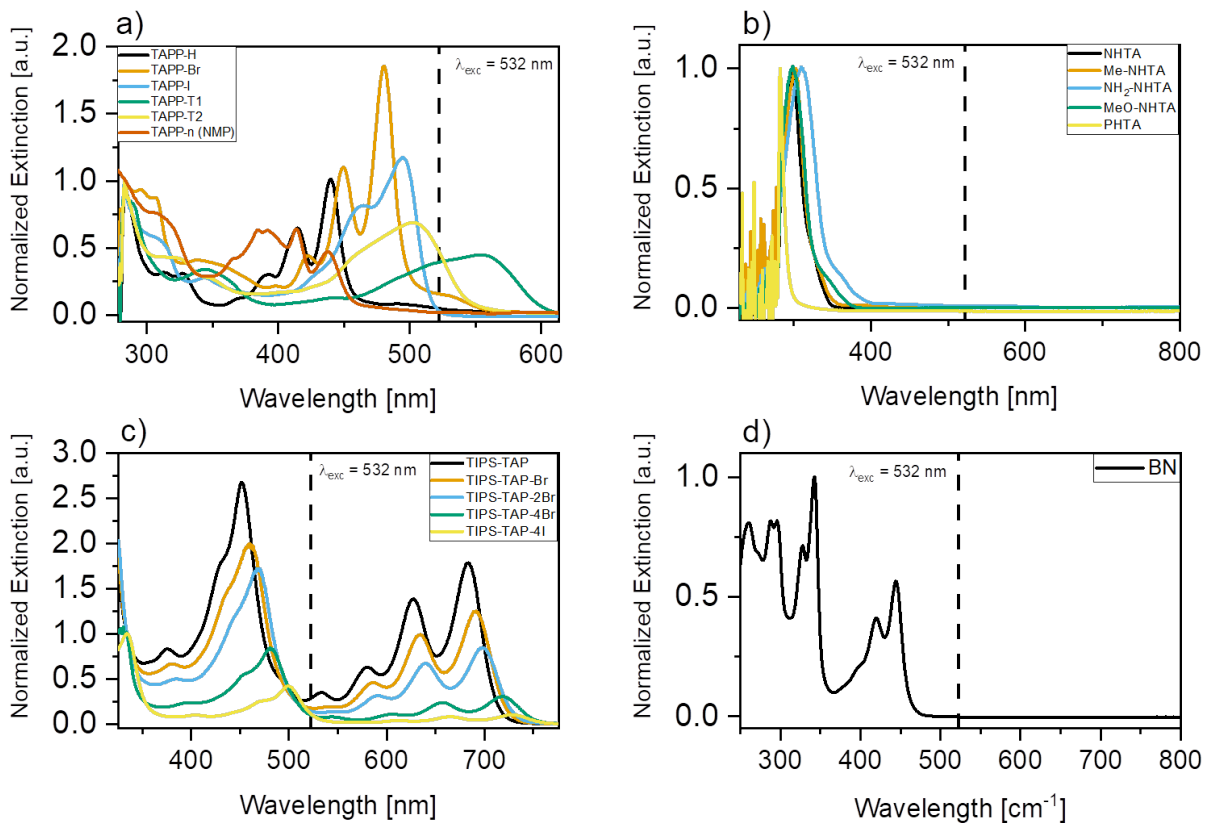


Figure 6.2: Summary of all UV-vis spectra for all molecule solutions for a) Tetraazaperopyrenes, b) Triangulenes, c) Tetraazapentacenes and d) Benzonaphthyridines. Note that all spectra are in Toluene except TAPP-n (NMP) and all BNs (Chloroform).

Another important property apart from the resonance conditions are the frontier molecular orbital energies (i.e. HOMO and LUMO) to see, whether the molecules will act as an acceptor or donor molecule when in contact with graphene (Fermi energy eV). A summary of the HOMO/LUMO energies over the range of all molecules can be seen in figure 6.3 and shows that the triangulenes will exhibit donor-type behavior, whereas the other three molecule families will exert acceptor-type interactions.

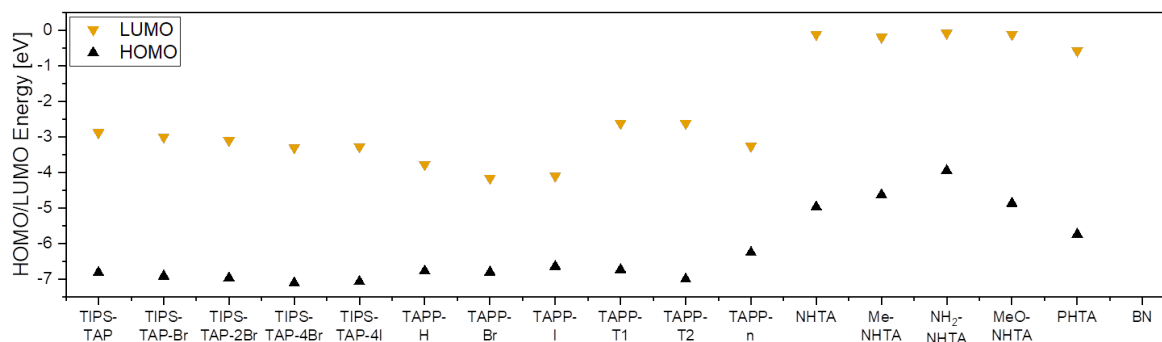


Figure 6.3: Overview over the range of different HOMO (black) and LUMO (yellow) energies of all investigated molecules.

Before the commercial CVD graphene could be used a cleaning procedure had to be established first. Water and polymer residues that are leftovers of the wet transfer process of graphene onto Si/SiO<sub>2</sub> wafer were cleaned off by rinsing the graphene with methanol and annealing in inert conditions at 300°C. A subsequent NMP-treatment step was done following a protocol from Thodkar *et.al.*<sup>89</sup> to further reduce the amount of adsorbed residues and to level out the electronic properties of graphene to achieve a reliable comparability over all samples and measurements.

The first steps to formulate a reliable deposition protocol of the Heteroacenes was done with one derivative of the TIPS-Tetraazapentacene family (TIPS-TAP-2Br) by comparing different solvents and deposition techniques. Dipcoating was compared to a dropcasting method with the result of dipcoating being the more favorable technique due to the overall more homogeneous deposition over the sample as was shown by the statistical analysis of Raman intensity ratios. In case of the question which solvent is most suited Toluene showed the best results in combination with dipcoating. Thus the general heterostructure preparation was done by dipcoating out of Toluene. After deposition of the molecules Raman spectra were measured to extract the intensity ratio of the graphene 2D- and G-band due to their sensitivity towards shifts in Fermi energy induced by the charge transfer between molecules and graphene. The Raman intensity ratios were correlated with the energies of frontier molecular orbitals; for acceptor type molecules the LUMO energy and for donor type molecules the HOMO energy was considered (figure 6.3).

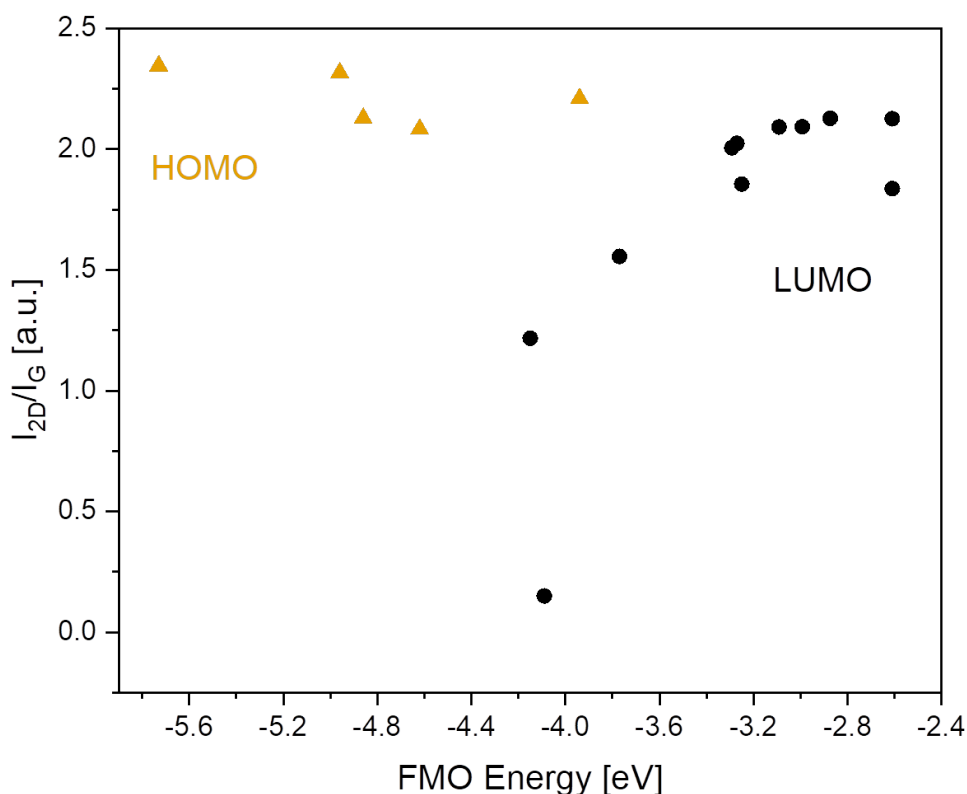


Figure 6.4: Summary of measured Raman intensity ratios in relation to the Frontier Molecular Orbital (FMO) energies for both acceptors (LUMO, black) and donors (HOMO, yellow).

To further test the impact of heteroacene deposition on the electronic properties of graphene, KPFM measurements were carried out to investigate possible changes in work function that are tied to the Fermi level shifts. As shown in figure X the data for acceptor-type interaction (represented by the LUMO energy in black) follows a non-linear trend of a decrease in Raman intensity ratios with decreasing LUMO energy as expected. However it seems there is a rather sharp cut-off around -4.2 eV that is in the same range as the work function of our CVD-grown graphene in ambient conditions<sup>122</sup> suggesting rather strong charge transfer interactions. Going to lower FMO energies with donor-type molecules lead on the other hand again to an increase in Raman intensity ratio as the overlap between graphene and molecular orbitals gets less favorable. However, to truly identify this overarching behavior there are still more data points needed, especially around the transitional region between donor- and acceptor-type doping, which makes further molecule synthesis effort important.

The second part of characterization of the graphene/heteroacene structures was focused on investigating the changes in work function of the system that are closely related to the Fermi level shifts. To do that, ambient KPFM measurements were carried out. To mini-

mize the impact of additional shifts in work function due to surface dipole formation the sample were mildly washed with toluene to ensure a low layer number of molecules. The resulting data nicely follows the theoretical trend of a decreasing work function with either increasing FMO energy or the corresponding Raman intensity ratio. However, the data show a reasonable amount of scattering due to the still heavy influence of surface dipoles. Especially molecules that have substituents that are oriented out of the molecular plane, e.g. the methyl-groups of all Triangulenes will increase the work function significantly overshadowing the modulation resulting from the Fermi level shift alone. Therefore it is always crucial to not only look at the doping (or Fermi energy shift) but also identify the work function of the system separately.

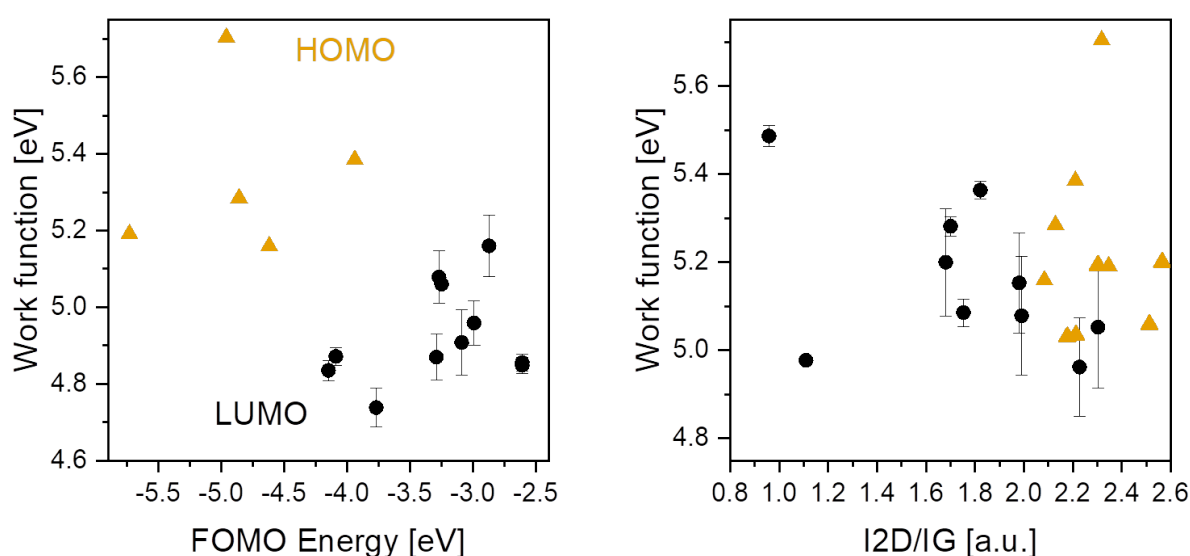


Figure 6.5: Left: summary of measured work functions in correlation to either HOMO energies (yellow) for donors and LUMO energies (black) for acceptors. Right: summary of work function correlated to the measured Raman intensity ratios.

With the deposition of organic aromatic molecules it is possible to induce further property changes apart from the charge transfer interaction to modulate the Fermi energy of graphene. Two different approaches in additional modification after deposition were explored with the UV oxidation of triangulenes to a stable radical cation and the acid mediated protonation of benzonaphthyridine. Apart from the change in interaction between molecule and graphene it was first important to evaluate that both the UV irradiation and HCl treatment of the graphene/heteroacene systems does not effect graphene by mainly introducing a high amount of defects. Experiments with UV treatment as well as HCl show that there is no significant increase in defect density in graphene thus the follow up measurements regarding changes in charge transfer are a result of the alteration of

the molecular structure. For the oxidation of the triangulenes it is expected that the electron density of graphene will increase due to the electron transfer which can indeed be observed with the Raman intensity ratios. However the overall changes are rather small, most likely due to an incomplete conversion of all deposited molecules. Regarding the changes in work function an opposite trend of a decrease is to be expected that can also nicely be demonstrated. Here the overall impact is slightly more significant than with the Raman measurements.

The observations with the HCl treatment of Benzonaphthyridines also confirm the expected trends and suggest that the on-graphene modification through acid-treatment leads to an incomplete conversion. The overall trends are consistent and as far as it is measurable the molecule protonated in solution shows the same Raman vibrations as the molecule protonated on graphene.

Those two series of experiments nicely demonstrate the additional possibilities of non-covalent graphene modification that is enabled through the vast number of possible functionalities that can be synthesized, to further improve the

It could be demonstrated that with precisely engineering the donor or acceptor strength of aromatic molecules a broad range of Fermi energy shifts can be realized in graphene. Even larger substituents like Methylthiophene or even the TIPS-solubility groups will not influence the van-der-Waals interactions between aromatic core and graphene significantly thus still making self assembly on graphene possible. Of course at a certain point bulky substituents will exert an influence, for example if the substituents drastically increase the aromatic core to graphene distance or if they start shielding the aromatic core.

Engineering the changes in work function of graphene are more complex due to both Fermi level shift and surface dipole induced by the molecules are responsible for the resulting work function, therefore it is always crucial to consider not only the electronic properties of the molecule but also its three dimensional structure if one wants to achieve control over the work function modification as well.

Lastly with the established protocols for deposition and Raman measurements the experiments were extended beyond graphene onto a well known TMD model system with CVD-grown MoS<sub>2</sub>. Here it could be nicely demonstrated that the factor governing the self assembly seems to be the acceptor/donor strength of the molecules due to the lack of  $\pi$ - $\pi$  interactions. A rather weak acceptor shows a very low Raman intensity compared to on-graphene measurements as one of the stronger acceptor molecules. Additionally it could be visualized that the dipcoating process, which relies on self assembly of the molecule on the target material leads to an assembly of molecule predominantly on MoS<sub>2</sub>-flakes leaving the underlying Silicone/Oxide substrate clean. The overall shifts in carrier density are in a comparable range to results found in the literature<sup>113,114,120</sup> and show, in combination with strain an expected trend of a reduction in carrier density through acceptor type interactions.

Overall, exploring and understanding the mechanisms behind non-covalent molecular doping on graphene leads to a variety of possibilities to fine tune the graphene properties to precisely fit the needs for all kinds of applications. The methodology developed from the well behaved model system graphene can then be transferred to other non-carbon nanomaterials like TMDs to further explore the possible modifications and tuning of these systems on the basis of non-covalent doping that was tested and analyzed on a rather controlled and understood substrate.

## 7 Bibliography

### References

1. da Silva Filho, D. A., Kim, E.-G. & Brédas, J.-L. Transport Properties in the Rubrene Crystal: Electronic Coupling and Vibrational Reorganization Energy. *Advanced Materials* **17**, 1072–1076 (2005).
2. Podzorov, V., Pudalov, V. M. & Gershenson, M. E. Field-effect transistors on rubrene single crystals with parylene gate insulator. *Applied Physics Letters* **82**, 1739–1741 (2003).
3. Takahashi, T., Takenobu, T., Takeya, J. & Iwasa, Y. Ambipolar organic field-effect transistors based on rubrene single crystals. *Applied Physics Letters* **88**, 033505 (2006).
4. Nichols, V. M. *et al.* Assessing the Potential of Peropyrene as a Singlet Fission Material: Photophysical Properties in Solution and the Solid State. *The Journal of Physical Chemistry C* **117**, 16802–16810 (2013).
5. Smith, M. B. & Michl, J. Recent advances in singlet fission. eng. *Annual review of physical chemistry* **64**. Journal Article, 361–386 (2013).
6. Wang, L., Sofer, Z. & Pumera, M. Will Any Crap We Put into Graphene Increase Its Electrocatalytic Effect? eng. *ACS nano* **14**, 21–25 (2020).
7. Randviir, E. P., Brownson, D. A. & Banks, C. E. A decade of graphene research: production, applications and outlook. *Materials Today* **17**, 426–432 (2014).
8. Klauk, H. *et al.* High-mobility polymer gate dielectric pentacene thin film transistors. *Journal of Applied Physics* **92**, 5259–5263 (2002).
9. Pramanik, C. & Miller, G. P. An improved synthesis of pentacene: rapid access to a benchmark organic semiconductor. eng. *Molecules (Basel, Switzerland)* **17**. Journal Article Research Support, U.S. Gov't, Non-P.H.S., 4625–4633 (2012).
10. De Angelis, F., Gaspari, M., Procopio, A., Cuda, G. & Di Fabrizio, E. Direct mass spectrometry investigation on Pentacene thin film oxidation upon exposure to air. *Chemical Physics Letters* **468**, 193–196 (2009).
11. Anthony, J. E. Functionalized acenes and heteroacenes for organic electronics. eng. *Chemical reviews* **106**, 5028–5048 (2006).
12. Anthony, J. E., Brooks, J. S., Eaton, D. L. & Parkin, S. R. Functionalized pentacene: improved electronic properties from control of solid-state order. eng. *Journal of the American Chemical Society* **123**, 9482–9483 (2001).

13. Chen, J., Martin, D. C. & Anthony, J. E. Morphology and molecular orientation of thin-film bis(triisopropylsilylethynyl) pentacene. *Journal of Materials Research* **22**. PII: S0884291400025954, 1701–1709 (2007).
14. Engelhart, J. U. *et al.* Halogenated Symmetrical Tetraazapentacenes: Synthesis, Structures, and Properties. eng. *The Journal of organic chemistry* **81**, 1198–1205 (2016).
15. Chu, M. *et al.* Halogenated Tetraazapentacenes with Electron Mobility as High as 27.8 cm<sup>2</sup> V<sup>-1</sup> s<sup>-1</sup> in Solution-Processed n-Channel Organic Thin-Film Transistors. eng. *Advanced materials (Deerfield Beach, Fla.)* **30**, e1803467 (2018).
16. Lim, Y.-F., Shu, Y., Parkin, S. R., Anthony, J. E. & Malliaras, G. G. Soluble n-type pentacene derivatives as novel acceptors for organic solar cells. *Journal of Materials Chemistry* **19**, 3049 (2009).
17. Geib, S. *et al.* Tuning redox chemistry and photophysics in core-substituted tetraazaperopyrenes (TAPPs). eng. *Chemistry (Weinheim an der Bergstrasse, Germany)* **19**, 13811–13822 (2013).
18. Hahn, L. *et al.* Core Halogenation as a Construction Principle in Tuning the Material Properties of Tetraazaperopyrenes. eng. *Chemistry (Weinheim an der Bergstrasse, Germany)* **21**, 17691–17700 (2015).
19. Hahn, L. *et al.* (Oligo-)Thiophene Functionalized Tetraazaperopyrenes: Donor-Acceptor Dyes and Ambipolar Organic Semiconductors. eng. *The Journal of organic chemistry* **82**, 12492–12502 (2017).
20. Geib, S. *et al.* 1,3,6,8-Tetraazapyrenes: synthesis, solid-state structures, and properties as redox-active materials. eng. *The Journal of organic chemistry* **77**, 6107–6116 (2012).
21. Yasuto Fujimaki, Keisuke Ogumi, Kosei Hayashi & Hiroti Watanabe. Evaluation of the Effect of pi Conjugate Plane Distortion on the HOMO-LUMO Level of Nanographene by Photoemission Yield Spectroscopy in Air. *The Japan Society for Analytical Chemistry* **67**, 693–697 (2018).
22. Peter Ribar, Tomas Solomek, Loic Le Pleux, Danies Häussinger, Alessandro Presciomone, Markus Neuburger, Michal Jurice. Donor-Acceptor Molecular triangles. *Synthesis*, 899–909 (2017).
23. Zheng, X. *et al.* One-electron oxidation of an organic molecule by B(C<sub>6</sub>F<sub>5</sub>)<sub>3</sub>; isolation and structures of stable non-para-substituted triarylamine cation radical and bis(triarylamine) dication diradicaloid. eng. *Journal of the American Chemical Society* **135**, 14912–14915 (2013).

24. Hirai, M., Tanaka, N., Sakai, M. & Yamaguchi, S. Structurally Constrained Boron-, Nitrogen-, Silicon-, and Phosphorus-Centered Polycyclic p-Conjugated Systems. eng. *Chemical reviews* **119**, 8291–8331 (2019).
25. Hammer, N., Schaub, T. A., Meinhardt, U. & Kivala, M. N-Heterotriangulenes: Fascinating Relatives of Triphenylamine. eng. *Chemical record (New York, N.Y.)* **15**, 1119–1131 (2015).
26. Kohl, B. *et al.* Attractive Dispersion Interactions Versus Steric Repulsion of tert-Butyl groups in the Crystal Packing of a D<sub>3h</sub>-Symmetric Tris(quinoxalinophenanthrophenazine). eng. *Chemistry (Weinheim an der Bergstrasse, Germany)* **22**, 646–655 (2016).
27. Madaan, A. *et al.* 1,8-Naphthyridine Derivatives: A Review of Multiple Biological Activities. eng. *Archiv der Pharmazie* **348**, 837–860 (2015).
28. Kim, J. H. *et al.* Novel Organic Semiconductors Based on 1,5-Naphthyridine–2,6-Dione Unit for Blue-Selective Organic Phototransistor. *Advanced Optical Materials* **8**, 2000695 (2020).
29. Sahoo, P. K. *et al.* Mechanochemical Synthesis, Photophysical Properties, and X-ray Structures of N-Heteroacenes. *European Journal of Organic Chemistry* **2016**, 1283–1291 (2016).
30. Novoselov, K. S. Nobel Lecture: Graphene: Materials in the Flatland. *Reviews of Modern Physics* **83**, 837–849 (2011).
31. Geim, A. K. Nobel Lecture: Random walk to graphene. *Reviews of Modern Physics* **83**, 851–862 (2011).
32. Simpson, D. nmat1849 Geim Progress Article.indd.
33. Barth, A. & Marx, W. *Graphene - A rising star in view of scientometrics* 2008.
34. Wick, P. *et al.* Classification framework for graphene-based materials. eng. *Angewandte Chemie (International ed. in English)* **53**, 7714–7718 (2014).
35. Balandin, A. A. Thermal properties of graphene and nanostructured carbon materials. eng. *Nature materials* **10**, 569–581 (2011).
36. Balandin, A. A. *et al.* Superior thermal conductivity of single-layer graphene. eng. *Nano letters* **8**, 902–907 (2008).
37. Changgu Lee, Xiaoding Wei, Jeffrey W. Kysar & James Hone. Measurement of the Elastic Properties and Intrinsic Strength of Monolayer Graphene. eng. *Science (New York, N.Y.)* **321**, 385–388 (2008).
38. Stankovich, S. *et al.* Graphene-based composite materials. eng. *Nature* **442**, 282–286 (2006).

39. Novoselov, K. S. *et al.* Electric field effect in atomically thin carbon films. eng. *Science (New York, N.Y.)* **306**, 666–669 (2004).
40. Nair, R. R. *et al.* Fine structure constant defines visual transparency of graphene. eng. *Science (New York, N.Y.)* **320**, 1308 (2008).
41. Jo, G. *et al.* The application of graphene as electrodes in electrical and optical devices. eng. *Nanotechnology* **23**, 112001 (2012).
42. Bonaccorso, F. *et al.* Production and processing of graphene and 2d crystals. *Materials Today* **15**, 564–589 (2012).
43. Hernandez, Y. *et al.* High-yield production of graphene by liquid-phase exfoliation of graphite. eng. *Nature nanotechnology* **3**, 563–568 (2008).
44. Abdelkader, A. M., Cooper, A. J., Dryfe, R. A. W. & Kinloch, I. A. How to get between the sheets: a review of recent works on the electrochemical exfoliation of graphene materials from bulk graphite. eng. *Nanoscale* **7**, 6944–6956 (2015).
45. Chen, J., Duan, M. & Chen, G. Continuous mechanical exfoliation of graphene sheets via three-roll mill. *Journal of Materials Chemistry* **22**, 19625 (2012).
46. Paton, K. R. *et al.* Scalable production of large quantities of defect-free few-layer graphene by shear exfoliation in liquids. eng. *Nature materials* **13**, 624–630 (2014).
47. Li, X. *et al.* Highly conducting graphene sheets and Langmuir-Blodgett films. eng. *Nature nanotechnology* **3**, 538–542 (2008).
48. Li, X. *et al.* Large-area graphene single crystals grown by low-pressure chemical vapor deposition of methane on copper. eng. *Journal of the American Chemical Society* **133**, 2816–2819 (2011).
49. Xuesong Li *et al.* Large-Area Synthesis of High-Quality and Uniform Graphene Films on Copper Foils. eng. *Science (New York, N.Y.)* **324**, 1312–1314 (2009).
50. Kang, J., Shin, D., Bae, S. & Hong, B. H. Graphene transfer: key for applications. eng. *Nanoscale* **4**, 5527–5537 (2012).
51. Suk, J. W. *et al.* Transfer of CVD-grown monolayer graphene onto arbitrary substrates. eng. *ACS nano* **5**, 6916–6924 (2011).
52. Castro Neto, A. H., Guinea, F., Peres, N. M. R., Novoselov, K. S. & Geim, A. K. The electronic properties of graphene. *Reviews of Modern Physics* **81**, 109–162 (2009).
53. Novoselov, K. S. *et al.* Room-temperature quantum Hall effect in graphene. eng. *Science (New York, N.Y.)* **315**, 1379 (2007).
54. Novoselov, K. S. *et al.* Electronic properties of graphene. *physica status solidi (b)* **244**, 4106–4111 (2007).

55. Novoselov, K. S. *et al.* Two-dimensional gas of massless Dirac fermions in graphene. eng. *Nature* **438**, 197–200 (2005).
56. Yu, Y.-J. *et al.* Tuning the graphene work function by electric field effect. eng. *Nano letters* **9**, 3430–3434 (2009).
57. Ferrari, A. C. & Basko, D. M. Raman spectroscopy as a versatile tool for studying the properties of graphene. eng. *Nature nanotechnology* **8**, 235–246 (2013).
58. Ferrari, A. C. Raman spectroscopy of graphene and graphite: Disorder, electron–phonon coupling, doping and nonadiabatic effects. *Solid State Communications* **143**, 47–57 (2007).
59. Cançado, L. G. *et al.* Quantifying defects in graphene via Raman spectroscopy at different excitation energies. eng. *Nano letters* **11**, 3190–3196 (2011).
60. Zabel, J. *et al.* Raman spectroscopy of graphene and bilayer under biaxial strain: bubbles and balloons. eng. *Nano letters* **12**, 617–621 (2012).
61. Malard, L. M., Pimenta, M. A., Dresselhaus, G. & Dresselhaus, M. S. Raman spectroscopy in graphene. *Physics Reports* **473**, 51–87 (2009).
62. Ferrari, A. C. *et al.* Raman spectrum of graphene and graphene layers. eng. *Physical review letters* **97**, 187401 (2006).
63. Lazzeri, M., Attaccalite, C., Wirtz, L. & Mauri, F. Impact of the electron–electron correlation on phonon dispersion: Failure of LDA and GGA DFT functionals in graphene and graphite. *Physical Review B* **78** (2008).
64. Sudipta Dutta, S. K. P. Novel properties of graphene nanoribbons: a review. *J. Mater. Chem.* **20**, 8207–8223 (2010).
65. Liu, H., Liu, Y. & Zhu, D. Chemical doping of graphene. *J. Mater. Chem.* **21**, 3335–3345 (2011).
66. Shi, Y., Dong, X., Chen, P., Wang, J. & Li, L.-J. Effective doping of single-layer graphene from underlying SiO<sub>2</sub> substrates. *Physical Review B* **79** (2009).
67. Schedin, F. *et al.* Detection of individual gas molecules adsorbed on graphene. eng. *Nature materials* **6**, 652–655 (2007).
68. Swathi, R. S. & Sebastian, K. L. Resonance energy transfer from a dye molecule to graphene. eng. *The Journal of chemical physics* **129**, 054703 (2008).
69. Swathi, R. S. & Sebastian, K. L. Long range resonance energy transfer from a dye molecule to graphene has (distance)<sup>(-4)</sup> dependence. eng. *The Journal of chemical physics* **130**, 086101 (2009).
70. Chang, C.-H., Fan, X., Li, L.-J. & Kuo, J.-L. Band Gap Tuning of Graphene by Adsorption of Aromatic Molecules. *The Journal of Physical Chemistry C* **116**, 13788–13794 (2012).

71. Dong, X. *et al.* Doping single-layer graphene with aromatic molecules. eng. *Small (Weinheim an der Bergstrasse, Germany)* **5**, 1422–1426 (2009).
72. Emery, J. D. *et al.* Structural analysis of PTCDA monolayers on epitaxial graphene with ultra-high vacuum scanning tunneling microscopy and high-resolution X-ray reflectivity. *Surface Science* **605**, 1685–1693 (2011).
73. Berner, N. C. *et al.* Understanding and optimising the packing density of perylene bisimide layers on CVD-grown graphene. eng. *Nanoscale* **7**, 16337–16342 (2015).
74. Das, A. *et al.* Monitoring dopants by Raman scattering in an electrochemically top-gated graphene transistor. eng. *Nature nanotechnology* **3**, 210–215 (2008).
75. Sadewasser, S. & Glatzel, T. *Kelvin Probe Force Microscopy* 530 pp. (Springer International Publishing, Cham, 2018).
76. Voigtländer, B. *Scanning Probe Microscopy* 375 pp. (Springer Berlin Heidelberg, Berlin, Heidelberg, 2015).
77. Melitz, W., Shen, J., Kummel, A. C. & Lee, S. Kelvin probe force microscopy and its application. *Surface Science Reports* **66**, 1–27 (2011).
78. Christodoulou, C. *et al.* Tuning the Work Function of Graphene-on-Quartz with a High Weight Molecular Acceptor. *The Journal of Physical Chemistry C* **118**, 4784–4790 (2014).
79. Packham, D. Surface energy, surface topography and adhesion. *International Journal of Adhesion and Adhesives* **23**, 437–448 (2003).
80. Wang, S., Zhang, Y., Abidi, N. & Cabrales, L. Wettability and surface free energy of graphene films. eng. *Langmuir : the ACS journal of surfaces and colloids* **25**, 11078–11081 (2009).
81. Kozbial, A. *et al.* Study on the surface energy of graphene by contact angle measurements. eng. *Langmuir : the ACS journal of surfaces and colloids* **30**, 8598–8606 (2014).
82. Beams, R., Gustavo Cançado, L. & Novotny, L. Raman characterization of defects and dopants in graphene. eng. *Journal of physics. Condensed matter : an Institute of Physics journal* **27**, 083002 (2015).
83. Avouris, P. & Dimitrakopoulos, C. Graphene: synthesis and applications. *Materials Today* **15**, 86–97 (2012).
84. Meric, I. *et al.* Current saturation in zero-bandgap, top-gated graphene field-effect transistors. eng. *Nature nanotechnology* **3**, 654–659 (2008).
85. Melios, C., Giusca, C. E., Panchal, V. & Kazakova, O. Water on graphene: review of recent progress. *2D Materials* **5**, 022001 (2018).

86. Melios, C. *et al.* Effects of humidity on the electronic properties of graphene prepared by chemical vapour deposition. *Carbon* **103**, 273–280 (2016).
87. Mitoma, N., Nouchi, R. & Tanigaki, K. Photo-oxidation of Graphene in the Presence of Water. *The Journal of Physical Chemistry C* **117**, 1453–1456 (2013).
88. Coletti, C. *et al.* Charge neutrality and band-gap tuning of epitaxial graphene on SiC by molecular doping. *Physical Review B* **81** (2010).
89. Thodkar, K. *et al.* Restoring the Electrical Properties of CVD Graphene via Physisorption of Molecular Adsorbates. eng. *ACS applied materials & interfaces* **9**, 25014–25022 (2017).
90. Bunz, U. H. F. N-heteroacenes. eng. *Chemistry (Weinheim an der Bergstrasse, Germany)* **15**, 6780–6789 (2009).
91. Geyer, F. L., Brosius, V. & Bunz, U. H. F. 2-Bromotetraazapentacene and Its Functionalization by Pd(0)-Chemistry. eng. *The Journal of organic chemistry* **80**, 12166–12176 (2015).
92. Anthony, J. E., Facchetti, A., Heeney, M., Marder, S. R. & Zhan, X. n-Type organic semiconductors in organic electronics. eng. *Advanced materials (Deerfield Beach, Fla.)* **22**, 3876–3892 (2010).
93. Filleter, T., Emtsev, K. V., Seyller, T. & Bennewitz, R. Local work function measurements of epitaxial graphene. *Applied Physics Letters* **93**, 133117 (2008).
94. Panchal, V., Pearce, R., Yakimova, R., Tzalenchuk, A. & Kazakova, O. Standardization of surface potential measurements of graphene domains. eng. *Scientific reports* **3**, 2597 (2013).
95. Würthner, F. Perylene bisimide dyes as versatile building blocks for functional supramolecular architectures. eng. *Chemical communications (Cambridge, England)*, 1564–1579 (2004).
96. Höfener, S., Günther, B. A. R., Harding, M. E. & Gade, L. H. Understanding UV-Vis Spectra of Halogenated Tetraazaperopyrenes (TAPPs): A Computational Study. eng. *The journal of physical chemistry. A* **123**, 3160–3169 (2019).
97. Dongqing Li/A. W. Neumann. Equilibrium of capillary systems with an elastic liquid-vapor interface.
98. Li, D. & Neumann, A. W. Contact Angles on Hydrophobic Solid Surfaces and Their Interpretation. *Journal of Colloid and Interface Science* **148**, 190–200 (1992).
99. Neumann, A. W., Good, R. J., Hope, C. J. & Sejpal, M. An Equation-of-State Approach to Determine Surface Tensions of Low-Energy Solids from Contact Angles. *Journal of Colloid and Interface Science* **49**, 291–304 (1974).

100. Gao, A. *et al.* Extreme ultraviolet induced defects on few-layer graphene. *Journal of Applied Physics* **114**, 044313 (2013).
101. Imamura, G. & Saiki, K. UV-irradiation induced defect formation on graphene on metals. *Chemical Physics Letters* **587**, 56–60 (2013).
102. Imamura, G. & Saiki, K. Modification of graphene/SiO<sub>2</sub> interface by UV-irradiation: effect on electrical characteristics. eng. *ACS applied materials & interfaces* **7**, 2439–2443 (2015).
103. Varrla, E. *et al.* Large-Scale Production of Size-Controlled MoS<sub>2</sub> Nanosheets by Shear Exfoliation. *Chemistry of Materials* **27**, 1129–1139 (2015).
104. Lee, Y.-H. *et al.* Synthesis of large-area MoS<sub>2</sub> atomic layers with chemical vapor deposition. eng. *Advanced materials (Deerfield Beach, Fla.)* **24**, 2320–2325 (2012).
105. Yang, S. Y., Shim, G. W., Seo, S.-B. & Choi, S.-Y. Effective shape-controlled growth of monolayer MoS<sub>2</sub> flakes by powder-based chemical vapor deposition. *Nano Research* **10**, 255–262 (2017).
106. Chen, F. *et al.* Morphological evolution of atomically thin MoS<sub>2</sub> flakes synthesized by a chemical vapor deposition strategy. *CrystEngComm* **22**, 4174–4179 (2020).
107. Splendiani, A. *et al.* Emerging photoluminescence in monolayer MoS<sub>2</sub>. eng. *Nano letters* **10**, 1271–1275 (2010).
108. Cho, K., Pak, J., Chung, S. & Lee, T. Recent Advances in Interface Engineering of Transition-Metal Dichalcogenides with Organic Molecules and Polymers. eng. *ACS nano* **13**, 9713–9734 (2019).
109. R. Coehoorn, C. Haas & and R. A. de Groot. Electronic structure of MoSe<sub>2</sub>, MoS<sub>2</sub>, and WSe<sub>2</sub>. II. The nature of the optical band gaps.
110. Knirsch, K. C. *et al.* Basal-Plane Functionalization of Chemically Exfoliated Molybdenum Disulfide by Diazonium Salts. eng. *ACS nano* **9**, 6018–6030 (2015).
111. Bertrand, P. A. Surface-phonon dispersion of MoS<sub>2</sub>.
112. Li, H. *et al.* From Bulk to Monolayer MoS<sub>2</sub>: Evolution of Raman Scattering. *Advanced Functional Materials* **22**, 1385–1390 (2012).
113. Michail, A., Delikoukos, N., Parthenios, J., Galiotis, C. & Papagelis, K. Optical detection of strain and doping inhomogeneities in single layer MoS<sub>2</sub>. *Applied Physics Letters* **108**, 173102 (2016).
114. Chae, W. H., Cain, J. D., Hanson, E. D., Murthy, A. A. & Dravid, V. P. Substrate-induced strain and charge doping in CVD-grown monolayer MoS<sub>2</sub>. *Applied Physics Letters* **111**, 143106 (2017).

115. Mouri, S., Miyauchi, Y. & Matsuda, K. Tunable photoluminescence of monolayer MoS<sub>2</sub> via chemical doping. *eng. Nano letters* **13**, 5944–5948 (2013).
116. Arramel *et al.* Molecular Alignment and Electronic Structure of N,Nâ<sup>2</sup> – Dibutyl – 3,4,9,10 – perylene – tetracarboxylic – diimide Molecules on MoS<sub>2</sub> Surfaces. *ACS Applied Materials & Interfaces* **9**, 5566–5573 (2017).
117. Obaidulla, S. M. *et al.* MoS<sub>2</sub> and Perylene Derivative Based Type-II Heterostructure: Bandgap Engineering and Giant Photoluminescence Enhancement. *Advanced Materials Interfaces* **7**, 1901197 (2020).
118. Tilmann, R. *et al.* Highly Selective Non-Covalent On-Chip Functionalization of Layered Materials. *Advanced Electronic Materials* **7**, 2000564 (2021).
119. Ramakrishna Matte, H., Subrahmanyam, K. S., Venkata Rao, K., George, S. J. & Rao, C. Quenching of fluorescence of aromatic molecules by graphene due to electron transfer. *Chemical Physics Letters* **506**, 260–264 (2011).
120. Kukucska, G. & Koltai, J. Theoretical Investigation of Strain and Doping on the Raman Spectra of Monolayer MoS<sub>2</sub>. *physica status solidi (b)* **254**, 1700184 (2017).
121. Keyshar, K. *et al.* Experimental Determination of the Ionization Energies of MoSe<sub>2</sub>, WS<sub>2</sub>, and MoS<sub>2</sub> on SiO<sub>2</sub> Using Photoemission Electron Microscopy. *eng. ACS nano* **11**, 8223–8230 (2017).
122. Konečný, M. *et al.* Kelvin Probe Force Microscopy and Calculation of Charge Transport in a Graphene/Silicon Dioxide System at Different Relative Humidity. *eng. ACS applied materials & interfaces* **10**, 11987–11994 (2018).

## 8 Experimental Parameters

### 8.1 UV-Vis/Absorbance Spectroscopy

Absorbance measurements were all done on either a Agilent Cary 60 or 6000i with a slit band width of 1.5 nm, 0.5 s acquisition time for each 0.5 nm data point. All sample solutions were measured in a 10x10 mm quartz cuvette.

### 8.2 Raman Spectroscopy

Raman spectroscopic measurements were done using a Renishaw inVia confocal Raman microscope with an excitation wavelength of 532 nm.

#### 8.2.1 Measurements on Graphene

All measurements were done by recording two-dimensional maps on the sample consisting of  $\sim 170$  spectra over an area of  $\sim 60 \times 60 \mu\text{m}^2$ . The laser power was adjusted to 10 % of the maximum power, which corresponds to  $\sim 5 \mu\text{W}$ . Each single spectrum was recorded with 2 seconds integration time and 2 accumulations to balance out the achieved spectral quality and the overall measurement duration. Analyzation of the Raman scattered light was conducted through a grating with  $2400 \text{ l/mm}$ .

Due to the influence of defects and multilayers on the graphene intensity ratio, every measurement spot had to be chosen carefully to minimize defects and multilayer content. Still every map measurement had to be carefully evaluated before extracting the desired intensities. As a first step all spectra showing signs of a high defect content were excluded. Those spectra can be identified by a high D- and D'-band intensity. To further exclude spectra showing bi- and multilayers the mean intensity of the G- and 2D-band were calculated to identify statistical outliers in those intensities that belong to spectra with non-monolayer content. This method is viable due to the graphene samples being mostly monolayers and the effect of molecular doping will be exerted homogeneously over the sample due to the method of coating.

To finally calculate the 2D- and G-band intensity ratio of each measurement, the intensities were extracted out of every baseline corrected spectrum of a map and the mean value was calculated.

To further increase statistical robustness of the calculated intensity ratio, each sample was usually measured in two different spots to increase the number of spectra used for calculation to about 300 to 320.

## 8.2.2 Measurements on MoS<sub>2</sub>

To measure the individual MoS<sub>2</sub> flakes circular maps with a slightly larger radius than the inner circle of the triangular flake were recorded to include parts of the Si/SiO<sub>2</sub> substrate as a reference. The step size of the map grid varied between 0.5 and 1.5 steps/mm depending on the actual size of the flake. This corresponds roughly to a total number of spectra between 95 to 150. All spectra were integrated for 1 second with 1 accumulation due to the broad spectral range.

The extraction of peak positions for the  $\epsilon$ -n plot were done by fitting a single Lorentzian to the mean signals over all points of the Raman maps, excluding spectra with no MoS<sub>2</sub> signals on the edges of the maps.

Visualizing the spacial distribution of intensities was done by fitting each single spectrum on every gridpoint again with a Lorentzian for each MoS<sub>2</sub> signal and molecule signal. The photoluminescence was fitted with a Gaussian function.

## 8.3 FM-KPFM

All AFM and FM-KPFM measurements were done under ambient conditions. Humidity and temperature were monitored during the measurements to ensure all measurements were carried out at  $30 \pm 5\%$  rH. As measurement Instrument a Bruker Dimension Icon was used. Standard topography characterization was done with Brukers ScanAsyst mode utilizing tips with the same name. For all FM-KPFM measurements SCM-PIT-V2 tips, also supplied from Bruker were used. To ensure conductivity these tips are coated with an platinum-iridium alloy and have a nominal tip radius of 25 nm for precise imaging of all possible graphene features.

As stated in section 3.3.2 the sample has to be connected to the electrical circuit of the measurement setup and be grounded. Due to the samples having an insulating layer of SiO<sub>2</sub> a conductive connection was achieved by using conductive copper tape to bridge the graphene surface to the AFM stage, which is itself part of the electrical circuit of the instrument.

To calculate the sample work function, the work function of the tip has to be known. To get access to this tip work function a standard measurement was carried out with every new tip and before each measurement series (e.g. five samples in one measurement run). As standard sample a gold surface with the known work function of 5.29 eV was used. For each calculated value three measurements per sample were taken and the mean  $V_{CPD}$  was used for the calculation.

Figure 8.1 show exemplary images taken on as received graphene, after NMP treatment and molecule deposition underlining again the need for annealing as the intercalated water leads to a decrease in precision of the surface potential measurement. After annealing however the surface potential measures perfectly the topography due to different potentials

for mono and bilayer (and wrinkles) graphene.

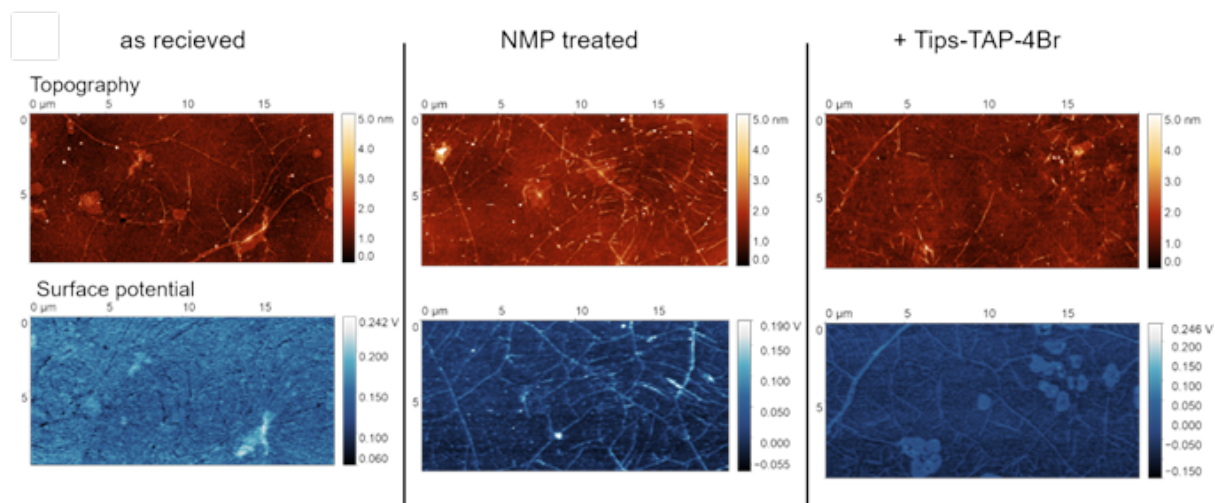


Figure 8.1: Raw KPFM images (out-of-box, annealed, NMP, Molecules)

## 9 List of Frequently Used Abbreviations

AFM	Atomic Force Microscopy
BN	Benzenophthiridine
CHCl <sub>3</sub>	Chloroform
CPD	Contact Potential Difference
CVD	Chemical Vapor Deposition
DCM	Dichloromethane
DMSO	Dimethylsulfoxide
DOS	Density of States
EA	Ethyl Acetate
eV	Electronvolt
FMO	Frontier Molecular Orbital
HCl	Hydrochloric Acid
HOMO	Highest Occupied Molecular Orbital
(S)KPFM	(Scanning) Kelvin-Probe-Force-Microscopy
LUMO	Lowest Unoccupied Molecular Orbital
MeCN	Acetonitrile
MoS <sub>2</sub>	Molybdenumdisulfide
HTA	Heterotriangulene
NMP	<i>N</i> -Methyl-Pyrrolidone
(TIPS)-TAP	(Triisopropylsilyl)-Tetraazapentacene
TAPP	Tetraazaperopyrene
THF	Tetrahydrofuran
TMD	Transitionmetal-dichalcogenide
UV	Ultraviolet
vis	visible

# 10 List of Figures

## List of Figures

2.1	Logical evolution of the tetraazapentacene structure and its HOMO/LUMO energy, starting with pentacene (a). To avoid oxidation of the acene structure (b), tri-isopropyl-silyl groups are added to the center ring (c). Introducing nitrogen into the backbone decreases HOMO and LUMO energy <sup>15</sup> compared to TIPS-pentacene <sup>16</sup> (d). Additional decrease of HOMO/LUMO energy is achieved by additional substitution with halogen atoms <sup>14,15</sup> (e). Energies for the halogen substituted molecules, differ only slightly from one another and thus are summarized here in two values for demonstrative purpose. . . . .	4
2.2	Overview of the pyrene molecule family and the changes in HOMO/LUMO energies from peropyrene <sup>21</sup> (a) to tetraazaperopyrene <sup>18</sup> (b) to tetra halogenated tetraazapentacene <sup>18</sup> (c). Peropyrene can be seen as a formal extension of the pyrene structure by adding an additional pyrene unit. Adding another pyrene unit will result in teropyrene and so on. The halogenated HOMO/LUMO energies are color coded to their respective halogens. . . .	5
2.3	General conceptual overview of heterotriangulenes. Bridging of a triphenylamin leads to a planarization of the molecular structure (a). The bridging can be done with several different structures, from heteroatoms like oxygen or sulfur to carbonyl or -CR <sub>2</sub> functionalities. <sup>24</sup> . Changing the center atom from N to P will lead to a non planar structure due to the initial structural constraint of the larger phosphorus (b). For comparison of the HOMO/LUMO <sup>25</sup> energies (bottom) only one relevant example for each heterotriangulene is displayed for simplicity. . . . .	6
2.4	Structural composition of benzonaphthyridine to derive the principle of its molecule structure that combines several well known building blocks for organic electronics. It can be seen as two acene units containing a 1,8-Naphthyridine unit (blue) that are fused via a pyrene core (red). To increase solubility tert-butyl groups are added to the pyrene unit (green). . .	7
2.5	Graphene unit cell with lattice vectors $a_1$ and $a_2$ (left) and corresponding Brillouin zone (right). Reciprocal lattice vectors are denoted as $b_1$ and $b_2$ and important lattice points are marked as explained in the text above. . .	10
2.6	Energy dispersion for the graphene unit cell with a zoom in on the Dirac point. Adapted from Neto <i>et al.</i> <sup>52</sup> . . . . .	11

2.7	Schematic representation of the Dirac cone at the K point of the graphene unit cell and the relation of the Fermi energy $E_F$ to the sample work function $W$ . The vacuum energy is denoted as $E_V$ and $W_0$ represents the work function of neutral graphene. <sup>56</sup> . . . . .	12
2.8	Comparison of Raman spectra for graphite (top) and graphene (bottom) at an excitation wavelength of 514 nm. Both spectra show the typical Raman signals with a G-band around $1585\text{ cm}^{-1}$ and a 2D-band around $2680\text{ cm}^{-1}$ . The main difference between graphite and graphene lies in the intensity ratio of both signals and the 2D-band being a single symmetrical Lorentzian for graphene. <sup>62</sup> . . . . .	13
2.9	Calculated phonon dispersion for graphene along the $\Gamma$ -K-M- $\Gamma$ direction. In total, six phonon branches can be observed of which the iLO and iTO phonons are relevant for Raman spectroscopy of graphene. Plot adapted from Ref <sup>61,63</sup> . . . . .	14
2.10	Phonon scattering processes leading to the main observable Raman modes of graphene. a) single resonance process at the $\Gamma$ point leading to the G-band. b) defect mediated double resonance at the K (and K') point leading to the D-band. c) and d) double and triple resonance respectively at the K (and K') point resulting in the 2D-band. . . . .	15
2.11	Schematic illustration of the phonon vibrations for the two main Raman signals of graphene. Left: the doubly degenerate iTO and iLO phonons at the $\Gamma$ -point responsible for the G-band. Right: Radial breathing mode of the iTO phonon at the K-point resulting in the 2D-band (and D-band with defects present). . . . .	16
2.12	Schematic representation of the Fermi energy $E_F$ at the Dirac points for from left to right, p-doped (electron poor), neutral and n-doped (electron rich) graphene. . . . .	17
2.13	Shift of graphene Raman signals in dependence of electron concentration. Asymmetric shift of G-band position to higher wavenumbers by both increase and decrease of electron concentration (top left). Downward shift of D-band position from low to high electron concentrations. (top right). Symmetric decrease of full width at half maximum (FWHM) of G-band (bottom left) and similar shift for the intensity ratio between 2D- and G-band (bottom right). Adapted from Das <i>et. al.</i> <sup>74</sup> . . . . .	19

2.14	Schematic of a confocal Raman microscope setup that was employed in this work. The 532 nm laser is coupled into a microscope objective to be focused on the sample surface. The scattered light then travels through a holographic notch filter (i.e. Rayleigh filter) to drastically reduce the elastic scattered light at 532 nm. The filtered light is then coupled into a spectrometer onto a CCD detector. . . . .	20
2.15	Schematic illustration of the general working principle of an AFM measurement. An oscillating cantilever with a sharp tip is moving either with direct contact or indirect contact (through interactions like van-der-Waals or electric/electrostatic forces) over the sample surface to track the profile via changes in oscillation that are observed with a laser that is reflected on the back of the cantilever onto a four quadrant detector. . . . .	21
2.16	Representation of Fermi energies of Tip and Sample ( $E_F$ (T) and $E_F$ (S)) relative to the Vacuum energy ( $E_V$ ) and the corresponding work functions ( $\Phi_T$ and $\Phi_S$ ). First sample and tip are separated by a distance $d$ and have no electrical interaction (a). After bringing both into contact (b) both Fermi levels will align and equilibrate through a flow of current with a contact potential difference ( $V_{CPD}$ ) forming. c) applying a DC voltage to counter the CPD. . . . .	23
2.17	Overview over a standard KPFM setup. The normal AFM setup to measure topography is extended with a KPFM controller and Lock-in Amplifier to control the voltage applied to the tip to measure the CPD in either a frequency or amplitude modulated fashion (FM- and AM-modes). Adapted from Melitz <i>et al.</i> <sup>77</sup> . . . . .	24
2.18	Relationship of tip work function ( $W_{Tip}$ ) and graphene work function ( $W_{Sample}$ ) relative to the Vacuum energy $E_V$ . $W_0$ describes the work function of completely neutral graphene but exposition of graphene to e.g. a substrate will change its Fermi energy $E_F$ . The sample and tip work function are directly related over the measurable surface potential difference $V_{CPD}$ and elemental charge $e$ as shown in equation 2.7. $W_{o/m}$ describes a possible offset of the work function with the presence of surface dipoles induced by adsorbates. . . . .	26

3.1	Summary of all <i>N</i> -Heteropolycycles used in this project: a) TIPS-Tetraazapentacenes with different substitutional patterns of bromine and iodine. TIPS-TAP-4H denotes only hydrogen substituents followed by one (TIPS-TAP-Br), two (TIPS-TAP-2Br) and four (TIPS-TAP-4Br) bromine substituents as well as four iodine substituents (TIPS-TAP-4I). b) Four different variations of <i>N</i> -Heterotriangulenes with either hydrogen (NHTA), methyl-groups (Me-NHTA), amino-groups (NH <sub>2</sub> -NHTA) or methoxy-groups (MeO-NHTA) as substituents. The fifth Heterotriangulene has hydrogen substituents and the center nitrogen atom is exchanged for a phosphorus atom (PHTA). c) Five different Tetraazaperopyrenes (TAPPs) with either four hydrogen (TAPP-H), bromine (TAPP-Br), or methylthiophen (TAPP-T1/T2) substituents. The fifth TAPP is called TAPP-n and is similar to TAPP-H but missing the perfluor sidechains. d) Benzonaphthyridines (BNs) with either pentyl- (5BN) or octyl-sidechains (8BN) or no alkyl-sidechains (0BN). . . . .	30
3.2	Histogram of mean 2D to G intensity ratio of N=79 samples with a mean value of 1.99 and a standard deviation of 0.15, showing the NMP treatment ensures a reproducible and reliable starting point for all Raman measurements. . . . .	31
3.3	Mean Raman spectrum (excitation wavelength 532 nm) of $\approx 300$ spectra taken over an area of two times $65 \times 65 \mu\text{m}^2$ of a NMP-cleaned graphene sample, showing the typical graphene Raman bands around $1585 \text{ cm}^{-1}$ (G-Band) and $2680 \text{ cm}^{-1}$ (2D-Band). Only minor defects are visible with a very low intensity of both D- and D'-Band at $1350 \text{ cm}^{-1}$ and $1610 \text{ cm}^{-1}$ respectively, that should not interfere with following measurements. . . . .	32
3.4	Sample preparation scheme; after initial annealing to remove intercalated water and residues the samples are treated with NMP for further cleaning and to achieve a homogeneous starting point to deposit the molecules onto graphene. Bottom row shows contact angle images with water demonstrating the increasing hydrophobicity after removing water and the changes of the surface due to different coatings. . . . .	33

3.5	a)-b) average Raman spectra of TIPS-TAP-2Br deposited onto graphene (532 nm excitation) normalized to the G-Band compared to the same graphene sample area prior to deposition. The mean of 170 spectra over a $65 \times 65 \mu\text{m}^2$ sample area is shown. Deposition by a) dip coating and b) drop casting. The inset in b) shows the Raman signature of the molecule. c)-e) Histograms of the intensity ratio of the graphene 2D and G band $I_{2D}/I_G$ after deposition of the molecule by dip coating (black) and drop casting (blue) from different solvents. c) Dichloromethane, DCM, d) Ethylacetate, EA, e) Toluene. f)-g) Histograms of the intensity ratio of the highest molecule peak ( $\text{@}1390 \text{ cm}^{-1}$ ) normalized to the graphene G-band. f) Dichloromethane, DCM, g) Ethylacetate, EA, h) Toluene. . . . .	34
3.6	Normalized absorbance spectra of all TIPS-TAPs in toluene displaying the subsequent shift in absorbance by increasing number and mass of halogen substituents. All TIPS-TAPs show the typical acene absorption feature between 500 nm and 700 nm. The dashed line indicates the excitation wavelength of 532 nm used for Raman measurements. . . . .	36
3.7	Absorbance spectra of TIPS-TAP-2Br freshly prepared in NMP (black) and after 7 days (yellow) demonstrating loss of most absorbance features attributed to decomposition. . . . .	37
3.8	Mean and corrected Raman spectra for all TIPS-TAPs on graphene showing both graphene (G-band at $1590 \text{ cm}^{-1}$ , 2D-band at $2690 \text{ cm}^{-1}$ ) and molecule ( $1200 \text{ cm}^{-1}$ to $1600 \text{ cm}^{-1}$ ) signals. No significant increase in defect density through processing can be observed due to low D'-band ( $1610 \text{ cm}^{-1}$ ) intensity. . . . .	38
3.9	a) to e) Comparison of the molecule Raman bands on graphene as deposited (black), after washing (yellow) and without graphene (blue). The bare molecule spectra are baseline corrected to account for the large, unquenched fluorescence background. f) DFT calculated Raman spectrum of TIPS-TAP-4H. . . . .	39
3.10	Raman intensity ratio in correlation with LUMO energies of the TIPS-TAP molecules showing an almost linear dependency between induced charge transfer and acceptor strength, that is in accordance to theory. . . . .	41
3.11	Top row: Examples of topography (orange) and contact potential difference (blue) scans. Bottom row: correlation of measured work function to LUMO energy (a) and Raman intensity ratio (b) of washed TIPS-TAP samples, showing the expected trends of a increasing work function with stronger acceptor interactions represented by LUMO energy and Raman 2D/G intensities. . . . .	42

3.12	Normalized absorbance spectra of all TAPP molecules with the Raman excitation at 532 nm indicated with a dashed line. All spectra show a similar structure with typical peropyrene-core bands from 400 nm to 550 nm although for thiophene substituted molecules these bands are rather broad in comparison. . . . .	44
3.13	Normalized absorbance spectra of a) TAPP-H, b) TAPP-Br and c) TAPP-T1 in NMP both freshly prepared (black) as well as after 6 days (yellow). All spectra show changes occurring after 6 days. These are only minor for TAPP-H, but significant for TAPP-T1 which seems to undergo some kind of degradation. . . . .	45
3.14	Mean and corrected Raman spectra for all TAPPs (532 nm excitation; dipcoated from toluene) on graphene showing both graphene (G-band at $1590\text{ cm}^{-1}$ , 2D-band at $2690\text{ cm}^{-1}$ ) and molecule ( $1200\text{ }^{-1}$ to $1600\text{ }^{-1}$ ) signals. . . . .	46
3.15	Comparison of the molecule Raman bands on graphene (black) and without graphene (yellow). The bare molecule spectra (532 nm excitation, dropcasted from toluene) are baseline corrected to account for the large, unquenched fluorescence background. . . . .	47
3.16	Summary of Raman spectroscopic results for all TAPPs. The top row shows examples how the different spectra were fitted to separate the molecule signal from the graphene G-Band. The bottom row shows from left to right the correlation of Raman intensity to the position of the G-band, the molecule Raman intensity for both NMP and toluene before and after washing as well as a plot of the relative intensity of the molecule vibration to the graphene Raman 2D/G ratio. . . . .	48
3.17	Correlation of the graphene Raman 2D/G intensity ratio as function of LUMO energy of the acceptor molecules. The scaling with the TAPP molecules is independent on whether acceptor molecule was removed by washing (a). In addition, panel (b) shows that data from TIPS-TAPs (green) and TAPPs (black) fall on the same curve which is in fact not linear, but shows a sharp decrease in graphene 2D/G ratio for lower LUMO energies. . . . .	49
3.18	Correlation of work function to both LUMO energy of the molecules (a) and Raman intensity ratio (b) showing previous trends demonstrated with TIPS-TAPs continue with TAPPs as a different acceptor molecule family. . . . .	50
3.19	Examples for optical images after deposition of five different solvents( water, glycerin, dimethylsulfoxide (DMSO), acetonitrile (MeCN) and isopropanol) on the TAPP-Br-graphene substrate. . . . .	51
3.20	Polynomial fitting of calculated Neumann parameters $\ln(0.5 + 0.5\cos(\theta))^2$ against the surface tension of the solvents used. From these plots and fits, the surface energy of the graphene-TAPP substrate can be calculated. . . . .	52

3.21	Surface energies for all TAPP molecules calculated with the Neumann model. Error values range between 0.01 and 0.025 and are thus not displayed.	53
4.1	Possible modifications that can be achieved after deposition of molecules: a) oxidation of triangulenes to a radical cation with UV light or chemically with a borane <sup>23</sup> ; b) protonation of the pyridinic nitrogen of benzonaphthyridines with mineral acids such as HCl.	54
4.2	Normalized absorbance spectra of all HTAs in toluene and Raman excitation of 532 nm indicated as dashed line. All molecules show a single absorption band below 400 nm without pronounced vibronic fine-structure. For PHTA this absorption is blue-shifted to the solvent absorption region below 300 nm. Only for NH <sub>2</sub> - and MeO-NHTA a small additional absorption red-shifted to the main absorption can be observed.	55
4.3	Comparison of NHTA treated with UV-light for 2h in chloroform solution (a) and chemically oxidized NHTA with two different weakly-interacting counterions (b). After UV treatment, NHTA shows a reduced intensity of the main spectral feature with an additional absorption at around 400 nm. Similar to that the chemical-oxidized species show the same pattern, however slightly shifted due to a different chemical environment.	56
4.4	Comparison of drop-casted NHTA on quartz before (black) and after (yellow) 2h of UV irradiation (253 nm).	57
4.5	Normalized Raman spectra of all HTAs and an annealed reference showing G- and D-band region both before and after UV-treatment. Right: bar chart showing the change in D-band intensity after irradiation with no significant increase for coated samples, but for the plain graphene reference.	59
4.6	Overlay of molecular Raman vibrations for NH <sub>2</sub> -NHTA (a) with (black) and without graphene (yellow) and zoom in on the absorbance spectra (b).	60
4.7	Summary of changes in Raman intensity ratio (a) and work function (b) before and after UV-treatment for all HTAs showing a corresponding trend of an increasing Raman intensity ratio with a decrease of the work function.	61
4.8	Comparison of pristine absorbance spectra (black) to spectra after protonation (yellow) for 0BN (a) 5BN (b) and 8BN (c) in toluene. Protonation was achieved by the addition of HCL. The characteristic electronic transitions of aromatic molecules are observed with vibronic fine structure. After protonation the transitions are red-shifted and the lowest energy transition is significantly broadened with no vibronic fine structure being observable any more.	62

4.9	Comparison of Raman spectra around the molecular vibrations and the graphene G-band for 0BN (a), 5BN (b) and 8BN (c) as-deposited on graphene (black), protonated on graphene (yellow) and protonated in solution prior to deposition (blue). In the case of 8BN, it was possible to record a Raman spectrum on aluminum (gray). . . . .	63
4.10	Summary of Raman (a) and work function measurements (b) for as-deposited BNs on graphene (black), protonated on graphene (yellow) and protonated in solution (blue). . . . .	64
5.1	Evolution of the electronic band structure of MoS <sub>2</sub> from a indirect (a) to a direct band-gap semiconductor (d), by layer reduction. Adapted from Splendiani <i>et. al.</i> <sup>107</sup> . . . . .	66
5.2	Structure of a MoS <sub>2</sub> monolayer from the side and top with corresponding in- and out-of-plane Raman modes. . . . .	69
5.3	Raman spectrum of a as-grown MoS <sub>2</sub> flake showing the Raman signals of the underlying Si/SiO <sub>2</sub> substrate (520.6 cm <sup>-1</sup> , 980 cm <sup>-1</sup> ) the E <sub>2g</sub> and A <sub>1g</sub> modes of MoS <sub>2</sub> at 384 cm <sup>-1</sup> and 405 cm <sup>-1</sup> respectively (insert) as well as a broad signal at 4000 cm <sup>-1</sup> related to the photoluminescence. . . . .	70
5.4	Overview of molecules deposited on MoS <sub>2</sub> . a) tetraazaperopyrenes (TAPP-H, -Br, -I), b) swallow-tail perylenebisimide (st-PBI) and c) benzonaphthyridine (0BN). . . . .	71
5.5	Absorption spectrum of st-PBI in toluene with a concentration of 10 <sup>-4</sup> mol/l as it was used for deposition. Dashed line indicates the Raman excitation. . . . .	72
5.6	Raman spectrum of st-PBI on graphene showing a similar vibrational structure to the other perylenes with a vibration close to the graphene G-band at 1590 cm <sup>-1</sup> and a I <sub>2D</sub> /I <sub>G</sub> ratio of 0.75. Signals around the 2D-band at 2690 cm <sup>-1</sup> are related to vibrations of the alkyl-substituents. . . . .	73
5.7	Raw (with only a constant baseline subtracted) Raman/photoluminescence spectra of pristine (black) and molecule-treated (yellow) MoS <sub>2</sub> for 0BN (a), TAPP-H (b), st-PBI (c), TAPP-Br (d) and TAPP-I (e). Inserts show magnifications of the MoS <sub>2</sub> and molecule vibrations. . . . .	74
5.8	Plot of MoS <sub>2</sub> A <sub>1g</sub> versus E <sub>2g</sub> position representative of the carrier to strain ratio for MoS <sub>2</sub> flakes before (black) and after (yellow) molecule deposition. Blue data points show average over all measurements before and after treatment. Gray dashed lines indicate changes in strain (±0.05%) and carrier density (±0.05 · 10 <sup>13</sup> cm <sup>-2</sup> ) based on exfoliated MoS <sub>2</sub> <sup>113</sup> . . . . .	76
5.9	Graphical illustration of HOMO/LUMO level alignment and possible charge transfer processes in MoS <sub>2</sub> when in contact with organic molecules. a) resonant process with st-PBI resulting in n-doping. b) non-resonant process with TAPPs resulting in photo-induced p-doping. . . . .	77

5.10	Integrated photoluminescence in comparison to both $A_{1g}$ (a) and $E_{2G}$ (b) Raman shifts as well as a correlation of photoluminescence before and after molecule deposition (c). The diagonal dashed lines in c) indicates the area of no change in PL after deposition, horizontal and vertical dotted lines indicate constant PL. . . . .	79
5.11	Examples of spacial distribution of Raman intensities for $MoS_2$ ( $A_{1g}$ mode) and TAPP-H @ $1610\text{ cm}^{-1}$ for two different flakes. Color scale ranges from blue for no to low intensity to red for high intensity. . . . .	80
5.12	Examples of spacial distribution of Raman intensities for $MoS_2$ ( $A_{1g}$ mode) and TAPP-Br @ $1598\text{ cm}^{-1}$ for two different flakes. Color scale ranges from blue for no to low intensity to red for high intensity. . . . .	81
5.13	Examples of spacial distribution of Raman intensities for $MoS_2$ ( $A_{1g}$ mode) and TAPP-I @ $1594\text{ cm}^{-1}$ for two different flakes. Color scale ranges from blue for no to low intensity to red for high intensity. . . . .	82
6.1	Summary recap of molecule families under investigation throughout this work. a) Tetraazapentacenes with different halogenation patterns. b) Triangulenes with different para-substituents. c) Tetraazaperopyrenes with different, more and less steric fourfold substituents. d) Benzonaphthyridines with different lengths of alkyl-sidechains. Blue marked molecules were the ones tested on $MoS_2$ . . . . .	85
6.2	Summary of all UV-vis spectra for all molecule solutions for a) Tetraazaperopyrenes, b) Triangulenes, c) Tetraazapentacenes and d) Benzonaphthyridines. Note that all spectra are in Toluene except TAPP-n (NMP) and all BNs (Chloroform). . . . .	86
6.3	Overview over the range of different HOMO (black) and LUMO (yellow) energies of all investigated molecules. . . . .	87
6.4	Summary of measured Raman intensity ratios in relation to the Frontier Molecular Orbital (FMO) energies for both acceptors (LUMO, black) and donors (HOMO, yellow). . . . .	88
6.5	Left: summary of measured work functions in correlation to either HOMO energies (yellow) for donors and LUMO energies (black) for acceptors. Right: summary of work function correlated to the measured Raman intensity ratios. . . . .	89
8.1	Raw KPFM images (out-of-box, annealed, NMP, Molecules) . . . . .	95



**Eidesstattliche Versicherung gemäß § 8 der Promotionsordnung für die Gesamtfakultät für Mathematik, Ingenieur- und Naturwissenschaften der Universität Heidelberg / Sworn Affidavit according to § 8 of the doctoral degree regulations of the Combined Faculty of Mathematics, Engineering and Natural Sciences at Heidelberg University**

1. Bei der eingereichten Dissertation zu dem Thema / **The thesis I have submitted entitled**

.....  
.....

handelt es sich um meine eigenständig erbrachte Leistung / **is my own work.**

2. Ich habe nur die angegebenen Quellen und Hilfsmittel benutzt und mich keiner unzulässigen Hilfe Dritter bedient. Insbesondere habe ich wörtlich oder sinngemäß aus anderen Werken übernommene Inhalte als solche kenntlich gemacht. / **I have only used the sources indicated and have not made unauthorised use of services of a third party. Where the work of others has been quoted or reproduced, the source is always given.**

3. Die Arbeit oder Teile davon habe ich wie folgt/bislang nicht<sup>1)</sup> an einer Hochschule des In- oder Auslands als Bestandteil einer Prüfungs- oder Qualifikationsleistung vorgelegt. / **I have not yet/have already<sup>1)</sup> presented this thesis or parts thereof to a university as part of an examination or degree.**

Titel der Arbeit / **Title of the thesis:** .....

Hochschule und Jahr / **University and year:** .....

Art der Prüfungs- oder Qualifikationsleistung / **Type of examination or degree:** .....

4. Die Richtigkeit der vorstehenden Erklärungen bestätige ich. / **I confirm that the declarations made above are correct.**

5. Die Bedeutung der eidesstattlichen Versicherung und die strafrechtlichen Folgen einer unrichtigen oder unvollständigen eidesstattlichen Versicherung sind mir bekannt. / **I am aware of the importance of a sworn affidavit and the criminal prosecution in case of a false or incomplete affidavit.**

Ich versichere an Eides statt, dass ich nach bestem Wissen die reine Wahrheit erklärt und nichts verschwiegen habe. / **I affirm that the above is the absolute truth to the best of my knowledge and that I have not concealed anything.**

.....  
Ort und Datum / **Place and date**

.....  
Unterschrift / **Signature**

<sup>1)</sup> Nicht Zutreffendes streichen. Bei Bejahung sind anzugeben: der Titel der andernorts vorgelegten Arbeit, die Hochschule, das Jahr der Vorlage und die Art der Prüfungs- oder Qualifikationsleistung. / **Please cross out what is not applicable. If applicable, please provide: the title of the thesis that was presented elsewhere, the name of the university, the year of presentation and the type of examination or degree.**